UNIVERSITY OF OKLAHOMA

GRADUATE COLLEGE

# HIGH-RESOLUTION TRANSMISSION ELECTRON MICROSCOPY ANALYSIS OF NANOSTRUCTURES

A DISSERTATION

SUBMITTED TO THE GRADUATE FACULTY

in partial fulfillment of the requirements for the

Degree of

DOCTOR OF PHILOSOPHY

By

MARK ERMAN CURTIS
Norman, Oklahoma
2009

HIGH-RESOLUTION TRANSMISSION ELECTRON MICROSCOPY ANALYSIS OF NANOSTRUCTURES

A DISSERTATION APPROVED FOR THE
HOMER L. DODGE DEPARTMENT OF PHYSICS AND ASTRONOMY

BY

______________________________
Dr. Matthew Johnson, Chair

______________________________
Dr. Sheena Murphy

______________________________
Dr. Lloyd Bumm

______________________________
Dr. Gregory Parker

______________________________
Dr. David Schmidtke

© Copyright by MARK ERMAN CURTIS 2009
All Rights Reserved.

*To my wife Tina, my son Harper,*
*my parents Gregory and Reita,*
*and my grandmother Eva Ruth*

# Acknowledgments

I would like express my deep appreciation to my thesis advisor Dr. Matthew Johnson for all of his guidance throughout my graduate studies. His mentoring has pushed me to develop a level of scientific discipline that will serve me well in my career.

In addition I would like to thank my doctoral committee members, Dr. Sheena Murphy, Dr. Lloyd Bumm, Dr. Gregory Parker, and Dr. David Schmidtke. Their advice and guidance has been tremendously helpful during my doctoral work.

I would like to express my gratitude to Dr. Joel Keay. His help throughout my graduate studies has been invaluable, and the knowledge he has imparted to me will assist me well into the future.

I would like thank Dr. Guoda Lian, Dr. Tetsuya Mishima, Dr. Ruwan Dedigama, Jeremy Jernigen, Roshan Bokalawela, Dan Brunski, Ernie Sanchez, and Kevin Hobbs for all their assistance with various projects. The help I have received and knowledge I have gained from them has assisted me in many ways, and I am deeply indebted to them.

I would like to especially thank Dr. Preston Larson and Mr. Greg Strout at the Samuel Roberts Noble Electron Microscopy Laboratory. Their knowledge and assistance has invaluable to my work.

Finally I would like to thank my wife, son, and family for all of their support during this process. It could not have happened without them.

# Table of Contents

Acknowledgments ........ iv

Table of Contents ........ v

List of Tables ........ viii

List of Figures ........ ix

Abstract ........ xix

Chapter 1: Introduction to Transmission Electron Microscopy of Nanostructures ........ 1

1.1 Introduction to Nanostructures ........ 1

1.2 Introduction to Transmission Electron Microscopy ........ 4

1.3 Dissertation Overview ........ 8

Chapter 2: Fabrication and Characterization of Free-Standing Silicon Nanomeshes ........ 12

2.1 Abstract ........ 12

2.2 Introduction ........ 13

2.3 Fabrication Details ........ 14

2.4 Electron Microscopy Results and Discussion ........ 21

2.5 Conclusions ........ 25

2.6 Acknowledgements ........ 26

Chapter 3: Characterization of $Mn^{2+}$ Doped ZnSe Branched Quantum Dots ........ 27

3.1 Abstract ........ 27

3.2 Introduction ........ 27

3.3 TEM Analysis ....28

3.4 Energy Dispersive Spectroscopy Analysis ....32

3.5 Conclusions ....34

3.6 Acknowledgments ....34

Chapter 4: Characterization of Cuboid-Shaped Microcrystals in PbSe Epitaxial Films ....35

4.1 Abstract ....35

4.2 Introduction ....35

4.3 Growth Details ....36

4.4 Optical and SEM Results ....36

4.5 Electron Backscatter Diffraction Results ....38

4.6 TEM Results ....44

4.7 Conclusions ....47

4.8 Acknowledgments ....48

Chapter 5: TEM and NBD Characterization of Ferroelectric Random Access Memory Device Capacitors ....49

5.1 Abstract ....49

5.2 Introduction ....50

5.3 Ferroelectric Random Access Memory ....52

5.4 Fabrication of FRAM Devices ....55

5.5 Focused Ion Beam Preparation of TEM Samples ....55

5.6 TEM/STEM Results ....59

5.7 Nanobeam Diffraction Results ....61

5.8 HRTEM Results ....65

5.9 Conclusions ....................................................................................................67

5.10 Acknowledgments...............................................................................................68

Chapter 6: Dual-Biprism Electron Holography of Ferroelectric Random Access Memory Device Capacitors..........................................................................................69

6.1 Abstract ...............................................................................................................69

6.2 Introduction.........................................................................................................70

6.3 Single-Biprism Electron Holography ..................................................................71

6.4 Dual-Biprism Electron Holography.....................................................................75

6.5 Results and Discussion .......................................................................................77

6.6 Conclusions.........................................................................................................84

6.7 Acknowledgments...............................................................................................84

Chapter 7: Characterization of a Bare PZT Layer on an FRAM Capacitor Electrode ......85

7.1 Abstract ...............................................................................................................85

7.2 Introduction.........................................................................................................85

7.3 SEM and AFM Results .......................................................................................86

7.4 XRD Results .......................................................................................................88

7.5 Preliminary PFM and BEPS Results...................................................................92

7.6 Conclusions.........................................................................................................96

7.8 Acknowledgements .............................................................................................97

Bibliography .........................................................................................................98

# List of Tables

Table 1.1 Comparison of TEM operational modes....................................................6

Table 3.1 Summary of the background corrected $K_\alpha$ x-ray counts from the x-ray spectra shown in figure 3.4b.......................................................................33

Table 5.1 A comparison of different types of memories ..........................................54

Table 5.2 Comparison of grain sizes from different FRAM capacitors.....................60

Table 6.1 Optimal lens current settings for dual-biprism electron holography on the Hitachi HF-3300 ..........................................................................................81

# List of Figures

Figure 1.1 Illustration of the size of objects, both naturally occurring and man-made, from a few millimeters down to tenths of nanometers. Nanostructures occupy the size regime from 1-100 nm (shown on the middle scale) and include structures such as DNA (naturally occurring) and carbon nanotubes (man-made)....................2

Figure 1.2 Characterization of an ordered array of Ni nanodots on an Si surface using (a) AFM for topology, (b) SEM for surface structure, and (c) TEM for internal structure....................3

Figure 1.3 Schematic of TEM....................5

Figure 1.4 Schematic of diffraction pattern formation....................8

Figure 2.1 Schematic of a free-standing Si nanomesh. The array of nanopores in the Si membrane can be seen from the top down view. From the cross-sectional view, the etched opening that the nanoporous membrane spans can be seen....................14

Figure 2.2 Cross-sectional schematic of fabrication procedure: : (a) Initial silicon-on-insulator sample pattern by oxide mask; (b) after anisotropic wet etch to open windows through handle layer; (c) lift-off of AAO template onto device layer; (d) pattern transfer through AAO template; (e) removal of

AAO and BOX layer; (f) self-limiting oxidation of structure resulting in encapsulated Si nanomesh ....................................................................15

Figure 2.3 Cross-sectional profile for anisotropic (top) and isotropic (bottom) etching of Si ..........................................................................................................16

Figure 2.4 (a) SEM image of an array of pyramidal pits etched into a Si (100) substrate with the TMAH. (b) Cross-sectional SEM image of one of the pits.........................................................................................................17

Figure 2.5 (a) Schematic of ordered anodic aluminum oxide (AAO). (b) An AAO film that has gone though the lift-off process onto a GaAs substrate. The GaAs has been etched through the AAO ..................................................18

Figure 2.6 Electron microscope images of free-standing silicon nanomeshes. (a) SEM image of openings wet-etched into the handle layer (from back side). (b) Bright-field TEM mage of unoxidized nanomesh (top side) spanning an opening in the substrate.........................................................................20

Figure 2.7 (a) SEI image of unoxidized Si nanomesh. (b) TEI image of unoxidized nanomesh with schematic of nanopore taper inset. (c) SEI image of oxidized nanomesh. (d) TEI image of oxidized nanomesh showing rings of oxide around the nanopores.................................................................22

Figure 2.8 TEM images of free-standing silicon nanomesh.(a) Bright-field image of oxidized mesh delineating crystalline SI and silicon oxide regions. Inset is a dark-field image showing the hole (black), the amorphous nature of the oxide (gray) and the crystalline silicon (white). (b) High-resolution TEM image of an oxidized nanomesh showing crystalline Si encapsulated by

high-quality oxide. Inset is a magnified view of lattice fringes in the remaining Si ........................................................................................23

Figure 2.9 (a) TEM image of encapsulated Si nanomesh after oxidation. b) Convergent beam diffraction (CBD) pattern used to determine the thickness of the Si. The Si thickness at position A, B, C, and D is 12.1, 14.0, 13.7, and 15.3 nm, respectively ......................................................24

Figure 3.1 A schematic of the branched d-dot structure showing four pods attached to a central core ........................................................................................29

Figure 3.2 Bright-field TEM image of $Mn^{2+}$ doped ZnSe branched d-dots. Some of the d-dots are missing pods......................................................................29

Figure 3.3 (a) High-resolution TEM image of a representative branched d-dot with four branches in crystallographic registry with the core. The branches are labeled 1 through 4. The crystal planes at the connections between the core and branches are superimposed on the image and thicker lined versions of these planes are labeled and positioned on adjacent areas off the quantum dot. (b), (c), (d), and (e) Indexed FFTs of the core, branch 1, 4 and 3, respectively .......................................................................30

Figure 3.4 (a) High angle annular dark field (HAADF) scanning TEM (STEM) image of a branched d-dot. The two boxes represent the areas from which the beam was rastered to acquire x-ray spectra. (b) X-ray spectra from area 1 (core) and area 2 (branch)......................................................................... 32

Figure 4.1 (a) Optical microscope image of cuboids in a PbSe (111) epilayer. (b) A higher magnification image of a group of cuboids ...................................37

Figure 4.2 Plan-view SEM images of (a) an individual cuboid and (b) a cluster of cuboids ....................................................................................37

Figure 4.3 A cross-sectional SEM image of a cluster of PbSe cuboids showing the root structure of a cluster in the PbSe (111) epilayer................................38

Figure 4.4 (a) Schematic of the concept of EBSD. (b) Optical image of the inside of an SEM chamber equipped for EBSD .....................................................39

Figure 4.5 (a) Top down SEM image of PbSe cuboid. (b) SEM image of same cuboid at 70° tilt to the electron beam for EBSD. (c) Raw EBSD pattern from the cuboid shows a raw EBSD pattern taken from the cuboid. (d) Same EBSD pattern indexed by the OIM software ..................................41

Figure 4.6 (a) SEM image of PbSe cuboid at with the sample surface tilted 70° to the electron beam. (b) EBSD orientation map of the image in (a) with an inverse pole figure inset used to determine orientation on the map. The EBSD map has been compressed vertically to match the SEM image of the cuboid due to the 70° tilt of the sample. (c) EBSD map of cuboid showing deviation of cuboid from perfect <100> orientation as a result of the cuboid face not being perfectly parallel to epilayer surface ......................42

Figure 4.7 (a) Top down SEM image of a PbSe cuboid with the orientation of both the cuboid and epilayer labeled. (b) and (c) Software rendering s of orientation of unit cell f or epilayer and cuboid, respectively. (d) and (e) Indexed EBSD patterns to determine unit cell in (b) and (c) , respectively .. ..........................................................................................................43

Figure 4.8 (a) Stitched bright-field TEM image of PbSe cuboid with the angles of the cuboid labeled. (b) Tilted bright-field TEM image of the PbSe cuboid. (b) Tilted dark-field TEM image of the PbSe cuboid ................................44

Figure 4.9 (a) Bright-field TEM image of the top of the PbSe cuboid. (b) and (c) PbSe epilayer SAD pattern and HRTEM image, respectively. (d) and (e) PbSe cuboid SAD pattern and HRTEM image, respectively ....................46

Figure 4.10 TEM image of the root at the bottom of the cuboid .................................47

Figure 5.1 A Venn diagram showing the relationship between ferroelectrics, pyroelectrics, and piezoelectrics ..............................................................52

Figure 5.2 (a) Schematic of PZT unit cell. The central ion can move along the c-axis giving rise to a spontaneous polarization. (b) Plot of polarization vs. electric field for a ferroelectric showing hysteresis. A bit (1 or 0) is stored as the remnant polarization of the material once the electric field has been removed..........................................................................................53

Figure 5.3 (a) A schematic of an FRAM capacitor. (b) SEM image of the capacitor without the W contacts.....................................................................55

Figure 5.4 (a) Part of an 8” wafer onto which the FRAM modules have been fabricated. (b) A cross-sectional, two-tiered chip that has been cut from the wafer using a dicing saw. The red square indicates the area that will be further thinned by FIB...........................................................56

Figure 5.5 A schematic of a dual-beam FIB/SEM system.........................................56

Figure 5.6 SEM image of a protective platinum strap deposited over the top to the FRAM capacitors. The dot structures on the surface are the top tungsten contacts of the buried capacitors ........................................................ 57

Figure 5.7 (a) Top down SEM image of the FIB milled window. The step pattern leading to the window in the center can be seen. (b) A cross-sectional SEM image of the final electron transparent window showing a row of FRAM capacitors ........................................................ 57

Figure 5.8 (a) An FRAM capacitor with an amorphous PZT layer due to FIB damage. (b) An FRAM capacitor from the same sample with crystalline PZT after careful FIB milling ........................................................ 58

Figure 5.9 (a) High-angle annular dark-field (HAADF) scanning transmission electron microscopy (STEM) image of a complete FRAM capacitor. (b) Stitched bright-field TEM image of an FRAM capacitor. Individual grains of PZT can be seen in both images ........................................................ 59

Figure 5.10 (a) TEM image of part of an FRAM capacitor with the smallest SAD aperture on the TEM inserted. (b) The SAD pattern taken from that area showing multiple crystallites. (c) NBD pattern taken from an individual grain in the capacitor showing a single crystal diffraction pattern. The diameter of the NBD beam used is indicated by the dashed red circle in (a) ........................................................ 61

Figure 5.11 Bright-field TEM image of an FRAM capacitor. Inset (lower left) shows a NBD pattern from the Si substrate below the capacitor, used as an in situ calibration. Inset (upper left) shows the NBD pattern for the PZT grain

indicated by the outlined box. Inset (upper right) is a higher mag. image of the outlined PZT grain (labeled grain 3), including an arrow indicating the c-axis. The dashed circle indicates the approx. diameter of the beam for the NBD pattern ........................................................................62

Figure 5.12 Four indexed NBD patterns taken from PZT grains in the FRAM capacitor, shown directly below. The capacitor is the same as the one shown in figure 5.11. The orientation for each grain was determined by indexing the NBD patterns. The sample tilts used to obtain the patterns and the measured c/a ratios are also shown ..............................................64

Figure 5.13 (a) High-resolution TEM image of PZT grain 3 from the same capacitor exhibiting 2-directional lattice. The c-axis is 3° off of a line normal to the capacitor electrodes. (b) A fast Fourier transform (FFT) of the HRTEM image, showing the c-axis. (c) A lower mag. TEM image showing the location of PZT grain 3 in (a) .................................................................. 66

Figure 5.14 Four indexed fast Fourier transforms (FFTs) taken from PZT grains in the same FRAM capacitor as before, shown directly below. The orientation of each grain was determined by indexing the FFT. The sample tilts used to obtain the HRTEM images for the FFTs and the measured c/a ratios are also shown.........................................................................................67

Figure 6.1 Microscope arrangement for single biprism electron holography .............71

Figure 6.2 <310> oriented etched tungsten tip used for a field-emission TEM which is key to electron holography....................................................................72

Figure 6.3 Reconstruction process for electron holography. The holograph is Fourier transformed producing side bands that represent the Fourier transform of the object wave and its conjugate. One of the sidebands is selected and an inverse Fourier transform is performed. The amplitude and phase can then be extracted from the reconstructed object wave......................................74

Figure 6.4 Detailed microscope arrangement for dual-biprism electron holography .75

Figure 6.5 Plot of electron hologram fringe spacing vs. applied voltage to the upper biprism (BP1). The fringe spacing is proportional to 1/V where V is the voltage on the biprism.....................................................................77

Figure 6.6 Bright-field TEM image of a bank of FRAM capacitors. The shadow of one of the electron biprisms can be seen going diagonally across the image during alignment of the biprisms. Ideally the biprism needs to be in a position such that it is aligned parallel to the sample/vacuum interface as indicated by the red line ..................................................................78

Figure 6.7 (a) Bright-field TEM image of both biprisms aligned for electron holography. Contamination on both biprisms can be seen. (b) Bright-field TEM image of the interference region (bright area) produced with both biprisms properly biased. Note the distortions in the interference region due to charging of the contamination particles..............................79

Figures 6.8 (a) Electron interference pattern using a single biprism. The finer fringes are the interference fringes and the coarser fringes near the edges of the interference region are Fresnel fringes. (b) Electron interference pattern

using two biprisms with interference fringes. The Fresnel fringes are not completely absent but are dramatically reduced ........................................80

Figure 6.9 Dual-biprism electron holograph of an Au particle imbedded in $Fe_2O_3$. Inset is an enlarged image of the Au particle showing subtle shifts in the interference fringes as they cross the particle. The horizontal fringes seen in the particle are Au lattice fringes ........................................................81

Figure 6.10 (a) SEM image of a row of FRAM capacitors prepared in cross section by FIB. Some of the capacitors have had their top layers removed by the FIB. (b) Dual-biprism electron holograph of PZT from one of the FRAM capacitor with higher magnification image of the interference fringes inset. Part of the capacitor was removed by the FIB producing a PZT /vacuum interface.........................................................................................82

Figure 7.1 (a) Plan view SEM image of the blanket PZT layer. (b) Cross-sectional SEM image of the blanket PZT layer with layers labeled. The sample is at a 70° tilt to the electron beam. Inset is a lower magnification x-sectional image showing depressions in the PZT due to the W contacts..................87

Figure 7.2 2 µm x 2 µm AFM image of the blanket PZT layer with 5 µm x 5 µm scan inset ..........................................................................................................88

Figure 7.3 Bragg-Brentano XRD powder arrangement ..............................................89

Figure 7.4 XRD plot of blanket PZT pattern with offset calculated powder XRD positions and intensities ...................................................................90

Figure 7.5 Four-circle diffractometer arrangement......................................................91

Figure 7.6 XRD texture pole figures for (a) 001, (b) 110, (c) 210 planes of the blanket PZT layer ....................92

Figure 7.7 (a) Schematic of the principle of PFM. (b) Relationship between the applied AC voltage signal to the tip and the deflection of the tip (piezo-response) .................... 93

Figure 7.8 (a) AFM image of an area of the blanket PZT. (b) PFM amplitude image showing piezoresponse. (c) PFM phase image showing domains ............94

Figure 7.9 Schematic of the principle behind BEPS ....................95

Figure 7.10 BEPS Spectrograms (frequency vs. voltage step) during polarization switching that show the (a) amplitude and (b) phase....................96

# Abstract

Nanostructures are of great interest because of the unique size range they occupy between the bulk and the quantum regimes. Characterizing nanostructures requires tools that can access this size regime. Transmission electron microscopy (TEM) is one of the most important tools used to study materials and structures on the nanoscale because of its high-resolution imaging capabilities and the number of different characterization techniques that one single instrument can perform. In this dissertation, the characterization of several types of nanostructures using TEM and TEM-based techniques is described in detail. These techniques are used in conjunction with other nanoscale characterization methods such as AFM, XRD, and SEM to obtain a more complete understanding of the structures being studied.

# CHAPTER 1:

# INTRODUCTION TO TRANSMISSION ELECTRON MICROSCOPY OF NANOSTRUCTURES

## 1.1. INTRODUCTION TO NANOSTRUCTURES

Nanostructures are objects possessing at least one dimension between 1-100 nm. Nanostructures are of great interest, not only because of their size but also the effect that their size has on their fundamental properties. The nanoscale size regime lies in between the bulk and the atomic regimes, giving nanostructures traits that are different from both. Because of their unique attributes, nanostructures have a variety of applications in biomedical, electronic, mechanical, and optical fields.

Nanostructures can be grouped into two categories: those occurring naturally and those that are man-made. This is illustrated in figure 1.1 [1] which shows the size scale of many naturally occurring and man-made structures from a few millimeters in size down to a few tenths of nanometers in size. Naturally occurring nanostructures consist of things such as viruses, proteins, and DNA. Man-made nanostructures include quantum dots, carbon nanotubes, and aerogels and even transistors in today's integrated circuits.

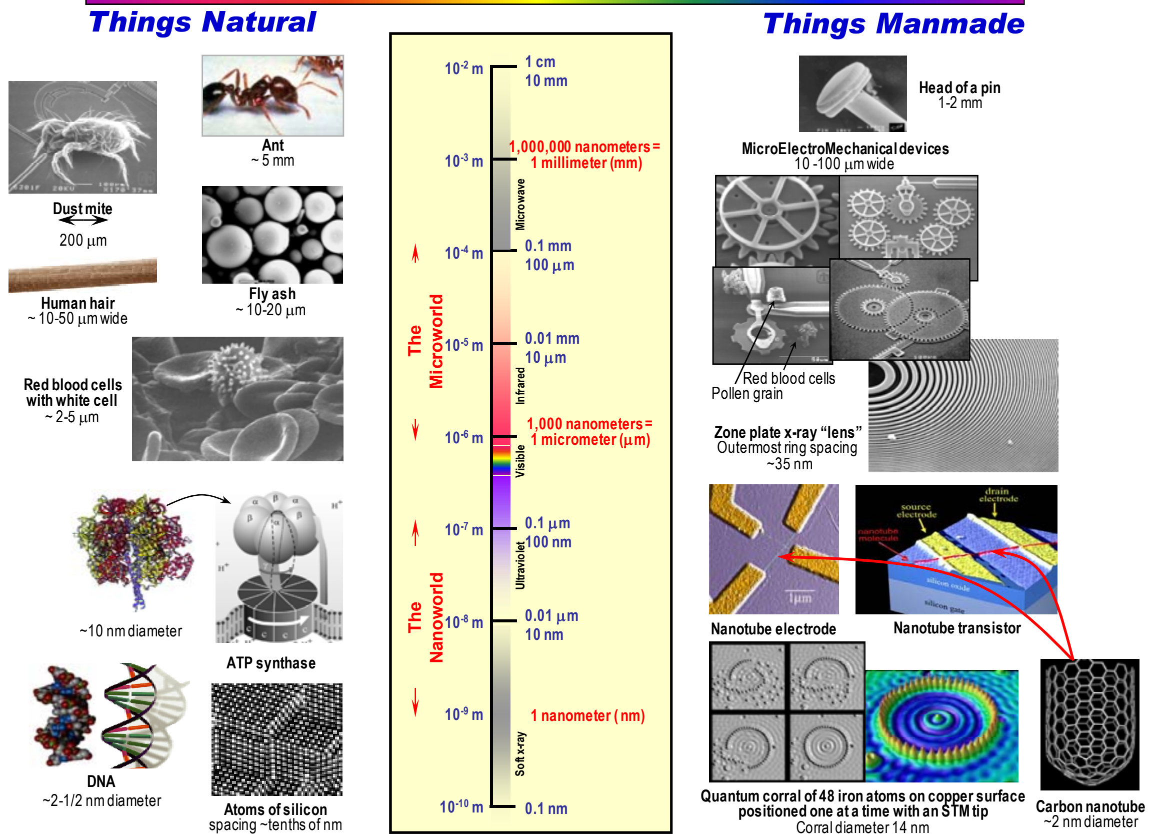


**Figure 1.1.** Illustration of the size of objects, both naturally occurring and man-made, from a few millimeters down to tenths of nanometers. Nanostructures occupy the size regime from 1-100 nm (shown on the middle scale) and include structures such as DNA (naturally occurring) and carbon nanotubes (man-made).

Over the last couple of decades there has been an intense amount of interest in the fabrication of nanostructures for various applications. There are two types of fabrication procedures, top-down and bottom-up. In bottom-up approaches, nanostructures are fabricated atom by atom until the desired structures are achieved. Examples of this include table-top chemical synthesis of colloidal quantum dots and nanoparticles, molecular beam epitaxy (MBE) of quantum wells and quantum dots, and self-assembled monolayers (SAMs). This is opposed to top-down approaches to nanofabrication which involve removal of bulk material to create nanostructures. Examples of top-down approaches include electron beam lithography, scanning probe lithography, laser ablation, chemical wet-etching, reactive ion etching (RIE), and focused ion beam (FIB) milling.

Since the interesting properties of nanostructures arise from their small size, there is a need to develop and extend characterization techniques to access the nanoscale. Techniques such as scanning probe microscopy (SPM) which includes scanning tunneling microscopy (STM), atomic force microscopy (AFM), magnetic force microscopy (MFM), and piezoresponse force microscopy (PFM) have been developed to study materials on the nanoscale. Additional techniques such as photoluminescence spectroscopy, UV-Vis-NIR spectroscopy, scanning electron microscopy (SEM), and x-ray diffraction (XRD) are also used to probe nanostructures and their properties. One particularly indispensible tool for studying nanostructures is transmission electron microscopy (TEM). TEM is related to SEM; however, whereas SEM images the surfaces of nanostructures, TEM images their internal structure down to the atomic scale. TEM is often used to analyze defects in nanostructures as well as determine their

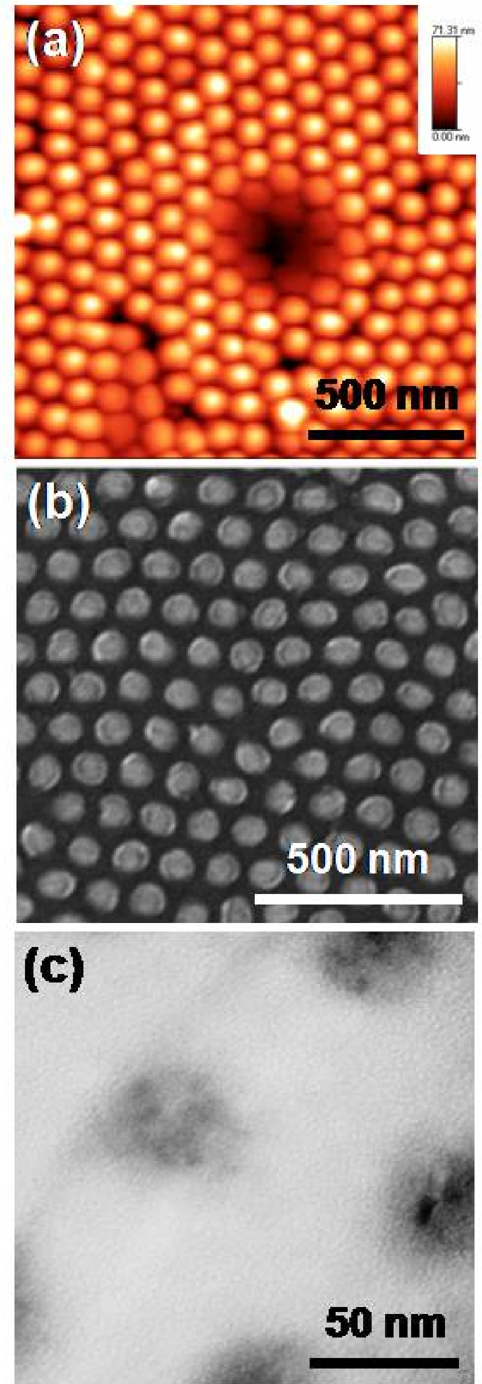


**Figure 1.2.** Characterization of an ordered array of Ni nanodots on an Si surface using (a) AFM for topology, (b) SEM for surface structure, and (c) TEM for internal structure.

.

crystallinity and composition.

Often many nanoscale characterization techniques are used together to provide information on different aspects of the same nanostructure. This is illustrated in figures 1.2. (a) – (c), which show an AFM, SEM, and TEM image of the same Ni nanodot patterned Si surface, respectively. The AFM image provides information on the topology of the nanostructured surface. The SEM image shows surface detail of the individual Ni nanodots. The TEM image provides information on the internal grain structure of the Ni nanodots which can be seen as areas of light and dark contrast within the dots.

## 1.2. INTRODUCTION TO TRANSMISSION ELECTRON MICROSCOPY

Transmission electron microscopy is a technique that relies on the use of electron waves (oscillating probability amplitude) instead of light waves (oscillating electric and magnetic fields). The wavelength of an electron is given by the de Broglie wavelength:

$$\lambda = \frac{h}{p} \tag{1.1}$$

where $h$ is Planck's constant and $p$ is the electron's momentum. In a TEM the electrons are emitted from either a thermionic or field emission source and are accelerated down the column of the TEM by a high voltage (typically 100-300 kV). A schematic of a TEM is shown in figure 1.3 [2]. The electrons are accelerated by the high voltage to a speed that is a significant portion of the speed of light (~ 0.7c for a 200 kV acceleration voltage) and therefore must be treated relativistically. The relativistic wavelength of the electron is given by:

$$\lambda = \frac{h}{\left[2m_0eV\left(1+\frac{eV}{2m_0c^2}\right)\right]^{\frac{1}{2}}} \tag{1.2}$$

where $m_0$ is the electron's rest mass, $e$ is the fundamental electric charge, $V$ is the accelerating voltage, and $c$ is the speed of light. Using a 200 kV accelerating voltage, which is typical for TEM, yields an electron wavelength of 0.025 Å.

In a TEM, the electrons are focused by a series of electromagnetic lenses. The first lenses that the electrons encounter in the TEM column are the condenser lenses which control the illumination of the sample. The sample must be thin enough (~ 100 nm thick or less) to be electron transparent. This is the major disadvantage of TEM and often necessitates tedious sample preparation to produce samples thin enough for characterization. The electrons either pass through the thinned sample unperturbed or scatter from the sample. The objective lens below the sample collects the electrons to form the first image of the sample. This image is then magnified by the rest of the imaging system and projected onto a phosphor screen or recording device.

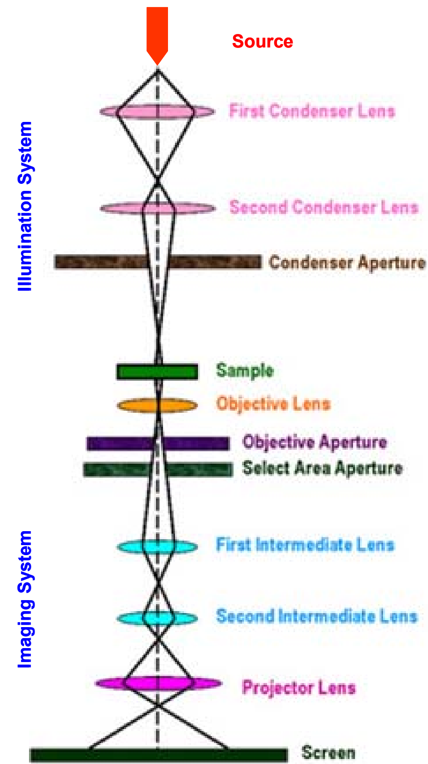


**Figure 1.3**. Schematic of TEM

The resolution that can be achieved by a TEM makes it one of the most important tools in studying nanostructures. It is important to note that the wavelength of the electron in the TEM is not the determining factor of the overall resolution of the microscope. The resolution of a TEM is ultimately limited by lens defects, the most prominent of which is the spherical aberration of the objective lens. However, recently,

| Mode | Principle of Operation | Information Gained |
|---|---|---|
| **Bright Field Imaging (BF)** | Uses electron beam transmitted directly through the sample for imaging | Contrast due to mass and thickness, some geometrical information; crystallographic information at high magnification |
| **Dark Field Imaging (DF)** | Uses electron beams diffracted by various crystalline planes | Crystallographic orientation; amorphous vs. crystalline areas; strain |
| **Scanning Transmission Electron Microscopy (STEM)** | Scans a converged electron beam across the sample. Uses a detector on the transmission side of sample to create image. Detectors to collect electrons scattered at high angles can be used | Atomic number contrast due to high angle scattering; Can be used in conjunction with other modes (*e.g.* EELS, EDS, etc.) |
| **Selective Area Diffraction (SAD)** | Uses aperture to select area on specimen and forms an electron diffraction pattern | Structure; spacing of atomic planes |
| **Convergent Beam Diffraction (CBD)** | Uses an small electron beam at a large convergence angle to form an diffraction pattern of a smaller area of the specimen than SAD | Crystallographic information from small areas; thickness of crystalline specimen; strain |
| **Nanobeam Diffraction (NBD)** | Uses small, parallel electron beam to form diffraction pattern of a smaller area of the specimen than SAD. Easier to interpret than CBD but not as versatile. | Crystallographic information from small areas |
| **Energy Dispersive Spectroscopy (EDS)** | Uses an electron probe to eject electrons from the electron shells of atoms. An electron from a higher shell emits a characteristic x-ray to fill the vacancy | Elemental composition |
| **Electron Energy Loss Spectroscopy (EELS)** | Uses a detector to measure the energy loss of electrons that have passed through a sample | Elemental composition; chemical bonding |
| **Electron Holography** | Splits incident electron wave into object wave (passes through sample) and reference wave (passes through vacuum). Recombines the two to produce electron interference pattern. Pattern contains amplitude and phase information of sample | Electric and magnetic fields in and around the sample |
| **Tomography** | Takes a series of images at different tilts and reconstructs a 3D image | 3D structural information |

**Table 1.1.** Comparison of TEM operational modes.

spherical aberration correctors have been realized to reduce the effect of spherical aberration [3]. Currently the best resolution that can be achieved in a TEM with the use of spherical aberration correctors is 0.5 Å [4].

While high-resolution TEM is extremely useful for imaging nanostructures, another advantage of TEM is the multitude of characterization techniques that can be performed at the same time in the same instrument. Several of the most common modes of TEM operation are given in table 1.1. All of these modes together enable the TEM to provide a wealth of information on the structural and compositional properties of nanostructures.

Bright-field imaging is the standard mode in which a TEM is typically used. Other than conventional bright-field imaging, diffraction mode is the next most utilized mode of a TEM and is also important in setting up the dark-field imaging mode. Diffraction mode utilizes Bragg diffraction from crystalline samples. The Bragg equation for diffraction is given by:

$$\lambda = 2d_{hkl} \sin\theta \qquad (1.3)$$

where $\lambda$ is the electron wavelength, $d_{hkl}$ is the distance between crystal planes (d-spacing), and $\theta$ is the angle between the incident beam and the diffracting crystal plane. Given that the electron wavelength in a 200 kV TEM in on the order of a few picometers and typical crystal d-spacings are on the order of a few of Ångstroms or less, the angle $\theta$ in the Bragg equation is quite small. The Bragg equation can therefore be reduced to:

$$\frac{\lambda}{d_{hkl}} = 2\sin\theta \approx 2\theta \qquad (1.4)$$

In a TEM, the diffracted beams that form the diffraction pattern are projected onto the viewing area as shown in figure 1.4. $R$ is the distance from the spot of the central

transmitted beam to the spot of the diffracted beam. $L$ which is shown as the distance from the sample to the viewing area is referred to as the camera length. Keeping in mind that $\theta$ is very small, the relationship between $R$ and $L$ can be written as:

$$\frac{R}{L} = \tan 2\theta \approx 2\theta \tag{1.5}$$

Equations (1.4) and (1.5) can then be combined to produce:

$$R = \frac{\lambda L}{d_{hkl}} \tag{1.6}$$

Equation 1.6 is one of the most important equations in TEM. It relates the distance between a recorded diffraction spot and the spot of the central transmitted beam to the distance between lattice planes for that particular diffraction spot. This can be used, in conjunction with the geometry of the diffraction pattern, to identify the crystal structure and determine d-spacings for crystal planes within the sample.

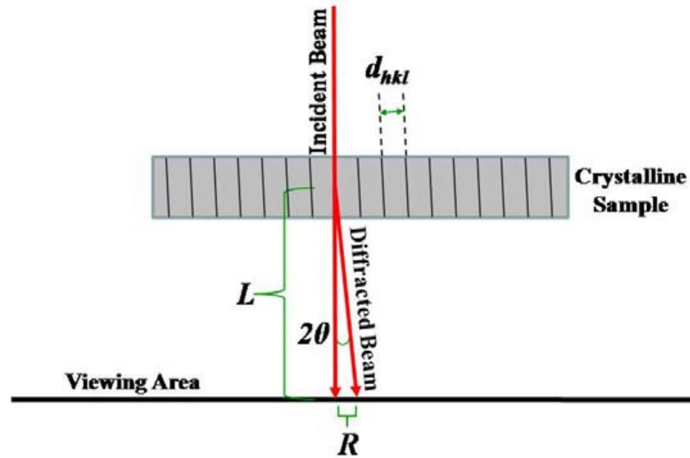


**Figure 1.4.** Schematic of diffraction pattern formation.

## 1.3. DISSERTATION OVERVIEW

This dissertation describes the TEM characterization of novel nanostructures. Details of the fabrication methods of the nanostructures and additional characterization techniques used to complement the TEM characterization are also provided, where appropriate. The chapters are, for the most part, presented in a historical manner in the

order the experiments were performed. The rest of the dissertation is organized as follows:

**Chapter 2: Fabrication and Characterization of Free-Standing Silicon Nano-meshes**

This chapter details the fabrication of novel free-standing nanometer-sized silicon meshes using a combination of photolithography, wet anisotropic etching, porous anodic aluminum oxide templates, and dry etching techniques. The results of SEM and TEM on the nanomeshes are given. Subsequent self-limiting thermal oxidation has reduced the cross-sectional dimensions of the remaining silicon to a size that is close to the quantum confinement size regime for silicon.

**Chapter 3: Characterization of $Mn^{2+}$ doped ZnSe Branched Quantum Dots**

In this chapter, the high-resolution TEM analysis of the crystallographic structure of colloidal $Mn^{2+}$ doped ZnSe branched quantum dots is discussed. In addition, the results of energy dispersive spectroscopy used to characterize the elemental composition of the dots are presented.

**Chapter 4: Characterization of Cuboid-Shaped Microcrystals in PbSe Epitaxial Films**

This chapter describes the characterization of cuboid-shaped PbSe microcrystals in PbSe (111) epilayers. SEM results are presented revealing that most of the cuboids posses flat, rectangular faces and extend a few microns into the epilayer. EBSD and SAD have determined that the exposed square face of the cuboids at the surface of the sample is a {100} plane. TEM results on a cuboid prepared in cross-section are also given.

**Chapter 5: TEM and NBD Characterization of Ferroelectric Random Access Memory Device Capacitors**

This chapter discusses the preparation of cross-sectional TEM samples of ferroelectric random access memory (FRAM) device capacitors by focused ion beam milling. The results of TEM characterization of individual grains of the ferroelectric lead zirconate titanate (PZT) layer from the capacitors are given. NBD patterns were taken from individual PZT grains and indexed thus allowing the crystallographic orientation of the grains to be determined. The presented results indicate a preferential orientation of the PZT grains with either the a- or c-axis of the grain generally normal to the FRAM capacitor electrodes. The results of fast Fourier transform (FFT) analysis of HRTEM images from individual PZT grains are also presented.

**Chapter 6: Dual-Biprism Electron Holography of Ferroelectric Random Access Memory Device Capacitors**

This chapter details experiments in performing dual-biprism electron holography on PZT layers within FRAM device capacitors. A brief background on electron holography is given followed by a discussion of the optimization of electron holography parameters on a Hitachi HF-3300 TEM. The electron holography results on PZT layers inside FRAM device capacitors are given. This chapter also discusses important practical considerations for dual-biprism electron holography of FRAM capacitors that were discovered during experimentation.

## Chapter 7: Characterization of a Bare PZT Film on a Ferroelectric Random Access Memory Device Capacitor Electrode

This chapter details characterization of the PZT layer of an FRAM device wafer that was removed from the fabrication line after deposition of the PZT. The bare PZT layer allowed for characterization methods not permitted using fully fabricated FRAM devices. SEM and AFM results are given describing the topology of the surface. X-ray diffraction results show that the grains in the PZT film are not randomly oriented but have a preference for having either their a- or c-axis perpendicular to the capacitor electrode. This chapter also discusses preliminary piezoresponse force microscopy (PFM) and band excitation piezoresponse spectroscopy (BEPS) results on the bare PZT film.

# CHAPTER 2:

# FABRICATION AND CHARACTERIZATION OF FREE-STANDING SILICON NANOMESHES

## 2.1. ABSTRACT

Novel free-standing nanometer-sized silicon meshes have been realized on silicon-on-insulator substrates using a combination of photolithography, wet anisotropic etching, porous anodic aluminum oxide templates, and dry etching techniques. Scanning electron microscopy (SEM) and transmission electron microscopy (TEM) results show ordered nanoporous silicon membranes spanning 45 μm x 45 μm openings in the substrate. The nanopores in the membrane are arranged in a 2D hexagonal close packed array with a nanopore diameter of approximately 50 nm and a center-to-center spacing of approximately 100 nm. Given this geometry, the Si in the nanomesh can also be thought of as intertwining wires of silicon nanowires. Subsequent self-limiting thermal oxidation has reduced the cross-sectional dimensions of these wires by approximately 60% as confirmed by TEM and convergent beam diffraction (CBD). This reduction in sizes moves the nanomeshes closer to the quantum confinement size regime for silicon.

## 2.2. INTRODUCTION

Silicon is the most widely used material in the semiconductor industry and is the key material in current microelectronic technologies. Currently, there is a push towards silicon optoelectronics in an attempt to overcome the limitations of traditional silicon microelectronics such as slower speeds [5]. Silicon, however, possesses an indirect band gap and radiative recombination of electrons in the conduction band with holes in the valence has a low probability of occurring since non-radiative processes dominate the recombination. This has limited silicon's usefulness in optoelectronics. One of the methods being explored to overcome this limitation is the use of nanostructured silicon. By reducing the dimensions of the silicon, there is hope to exploit quantum confinement when these dimensions approach the size of the exciton Bohr radius in silicon which is around 4.5 nm [6]. In addition, defects produced on the surface of the silicon during the nanostructuring process could also play a role in enhancing light emission. Improvements in radiative recombination, such as photoluminescence [7-9] as well as optical gain and stimulated emission [10], have been observed in nanostructured Si.

Nanoporous silicon is particularly interesting in applications beyond enhanced light emission. For instance, nanostructured silicon has shown utility as a sensor for detecting chemical vapors in the environment [11]. In addition, nanoporous materials are of interest for biological applications. Viruses, which are typically less than 100 nm in size, could easily be filtered by a synthetic nanoporous membrane, provided the pore diameters are smaller than the virus. In addition, solid-state nanoporous membranes have been fabricated and used to differentiate straight strands of DNA from folded strands of

DNA as the strands pass single file through a nanopore in the membrane [12]. This could give rise to a method of sequencing DNA in the future.

In this chapter, the fabrication of free-standing silicon nanomeshes using a combination of photolithography, wet anisotropic etching, porous alumina templates, and dry etching techniques is described in detail. These nanomeshes differ from other nanomeshes in that they are truly free-standing with no substrate directly underneath. Subsequent self-limiting oxidation of the nanomeshes reduced the dimensions of the silicon further. TEM, SEM, and CBD results will be discussed.

## 2.3. FABRICATION DETAILS

A schematic of a free-standing silicon nanomesh is shown in figure 2.1. The nanomesh consists of a 40-50 nm thick nanoporous silicon membrane that spans a 45 μm x 45 μm opening etched from the back side of the substrate. This frees-standing nature gives the nanomesh the ability to be characterized with TEM unlike nanomeshes that are not free-standing. The nanopores in the silicon membrane are ideally 50 nm in diameter and are arranged in an ordered 2D hexagonal close packed array with a 100 nm center-to-center spacing. In addition to the nanoporous membrane

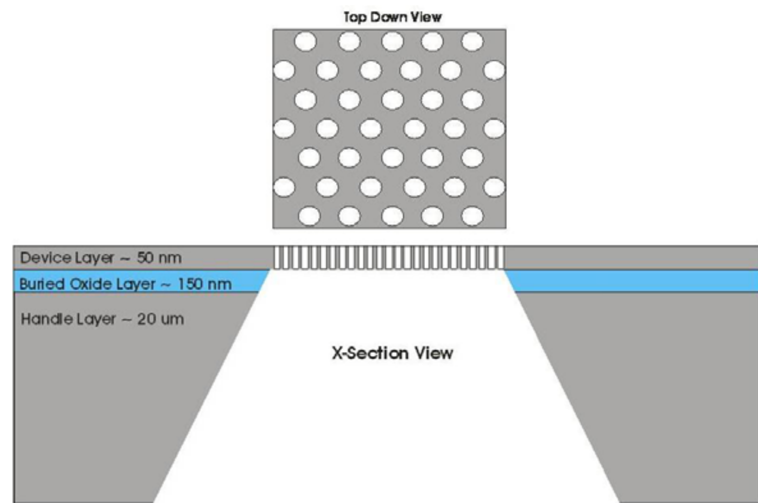


**Figure 2.1.** Schematic of a free-standing Si nanomesh. The array of nanopores in the Si membrane can be seen from the top down view. From the cross-sectional view, the etched opening that the nanoporous membrane spans can be seen.

description, the nanomesh can also be thought of as an array of intertwining Si wires with diameters of 40-50 nm.

Figure 2.2 shows a schematic of the procedure used to fabricate the free-standing silicon nanomeshes. The nanomeshes were fabricated from 5 mm by 5 mm cleaved pieces of n-type (As doped) silicon-on-insulator (SOI). The SOI consisted of a 53 nm thick Si (100) device layer on top of a 160 nm layer of $SiO_2$, referred to as the buried oxide (BOX) layer, on top of a 675 μm Si (100) handle layer. The handle layer was thinned to 20 μm by mechanical polishing using an Allied polisher. A series of diamond lapping films with progressively smaller particle sizes were used so that the final surface was free of any major scratches caused by the polishing process.

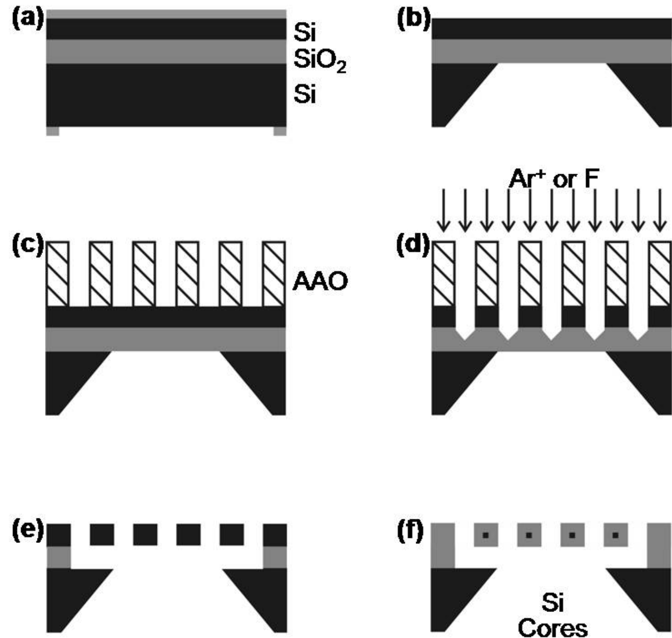


**Figure 2.2.** Cross-sectional schematic of fabrication procedure: (a) Initial silicon-on-insulator sample pattern by oxide mask; (b) after anisotropic wet etch to open windows through handle layer; (c) lift-off of AAO template onto device layer; (d) pattern transfer through AAO template; (e) removal of AAO and BOX layer; (f) self-limiting oxidation of structure resulting in encapsulated Si nanomesh.

The thinned SOI substrate was oxidized in a dry $O_2$ environment at 950 °C using a tube furnace. The SOI was oxidized for 30 min resulting in a $SiO_2$ layer approximately 10 nm thick encapsulating the SOI on all sides. This oxide layer was grown to serve as an etch barrier for the device layer and an etch mask for the handle layer. To define the oxide etch mask, photolithography was performed on the oxidized handle layer using a

copper TEM grid (60 μm x 60 μm openings, 80 μm center-to-center spacing) as a photolithography mask and Shipley S1818 photoresist. Alignment of the mask to the handle layer and UV exposure of the photoresist was done using a Karl Suss MJB-3 mask aligner. The mask was aligned in such a way that the edges of the square of openings on the TEM grid were parallel with the edges of the cleaved sample. After exposure to UV light, the sample was developed using Microposit MF-319 developer. An oxygen plasma descum was then performed in a March Plasmod plasma asher (50 W of power, 200 mTorr of $O_2$, 5 min descum time) to remove any photoresist residue on the exposed oxide in the openings.

The sample was then etched for 3 min in a 10:1 buffered oxide etch (BOE). This removed the thermal oxide and exposed the silicon underneath for etching as shown in figure 2.2a. The oxide etch barrier grown on the device layer was protected from the BOE by painting on a layer of S1818 photoresist prior to the BOE etch.

The sample was then etched using a mixture of 20 wt. % tetramethylammonium hydroxide (TMAH) using the thermally grown oxide as an etch mask as shown in figure 2.2b. TMAH is an anisotropic etchant of Si that etches the (100) planes of silicon faster than the (111) planes. A schematic of anisotropic etching is shown in figure 2.3. Figure 2.4 shows SEM results of this plane selectivity on a Si (100) substrate. Figure 2.4a shows an

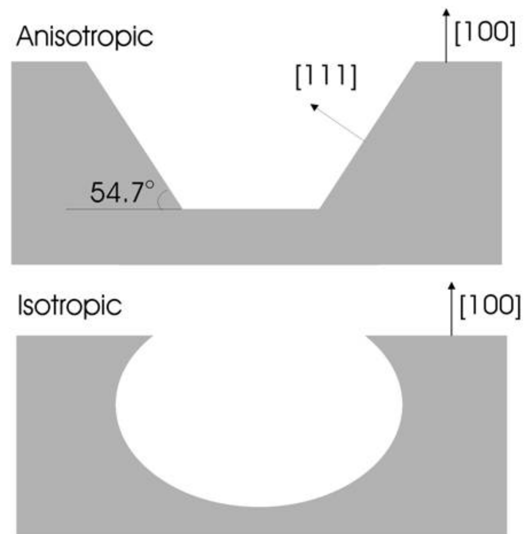


**Figure 2.3.** Cross-sectional profile for anisotropic (top) and isotropic (bottom) etching of Si (100).

array of pyramidal pits etched into the Si using the fabrication steps described above except for initial mechanical thinning of the substrate. Figure 2.4b shows a cross-sectional SEM image of one of the pits. The pyramid has a side angle of 52° with respect to the base which is close to the 54.7° angle between the (100) and (111) planes of Si. For the actual nanomesh, the thickness of the handle layer and the size of the openings in the etch mask, as defined by the TEM grid, were chosen such that the etch would terminate on the BOX layer before forming a complete pyramid. It should be mentioned here that for good etching results, the silicon surface to be etched must be free of major scratches and the etch mask must be aligned to the crystallographic axes of the substrate, otherwise misshapen etch pits will occur. In addition, for TMAH, it is crucial that n-doped Si is used as p-doped Si will not be etched and is often used as an etch stop. The initial fabrication procedure used a plastic beaker covered in paraffin film partially immersed in a heated water bath to hold the TMAH. Later TMAH etching was carried out in a reflux condenser to prevent water from leaving by evaporation thereby increasing the concentration of TMAH and lowering the etch rate. For the thinned SOI substrates, TMAH etching was carried out at 85° C for 90 min. This provided enough time for the etch to terminate at the BOX

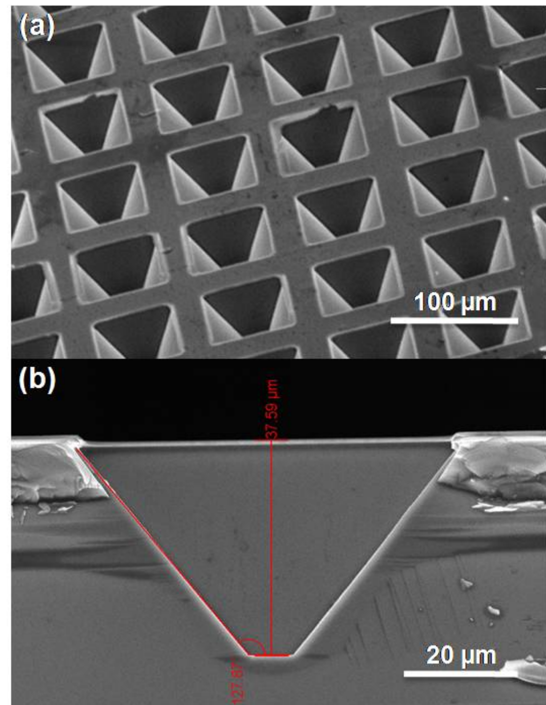


**Figure 2.4.** (a) SEM image of an array of pyramidal pits etched into a Si (100) substrate with the TMAH. (b) Cross-sectional SEM image of one of the pits.

layer of the SOI but not enough time for the TMAH to etch through the thermal oxide etch mask (TMAH does etch $SiO_2$ but much slower than Si). It should be noted that the TMAH quickly removed any photoresist on the sample upon coming into contact with the sample. After completion of the etch, the sample was removed to de-ionized (DI) water to stop the etch.

The nanopore array to be etched into the device layer was defined by an ordered anodic aluminum oxide (AAO) template. Figure 2.5a [13] shows a schematic of an ordered AAO film as it is grown on Al foil. AAO ordered over micron-sized domains is formed in a two-step anodization process as described by Masuda *et al* [13]. First a piece of Al foil is anodized in an electrolyte, either phosphoric, oxalic, or sulfuric acid depending on the pore diameter and center-to-center spacing desired. This first anodization step is performed for approximately 20 hrs, during which time the growing AAO pores become ordered at the Al/AAO interface by arranging themselves in a hexagonal close packed array to minimize the stress between neighboring pores. This AAO film is then etched away leaving ordered

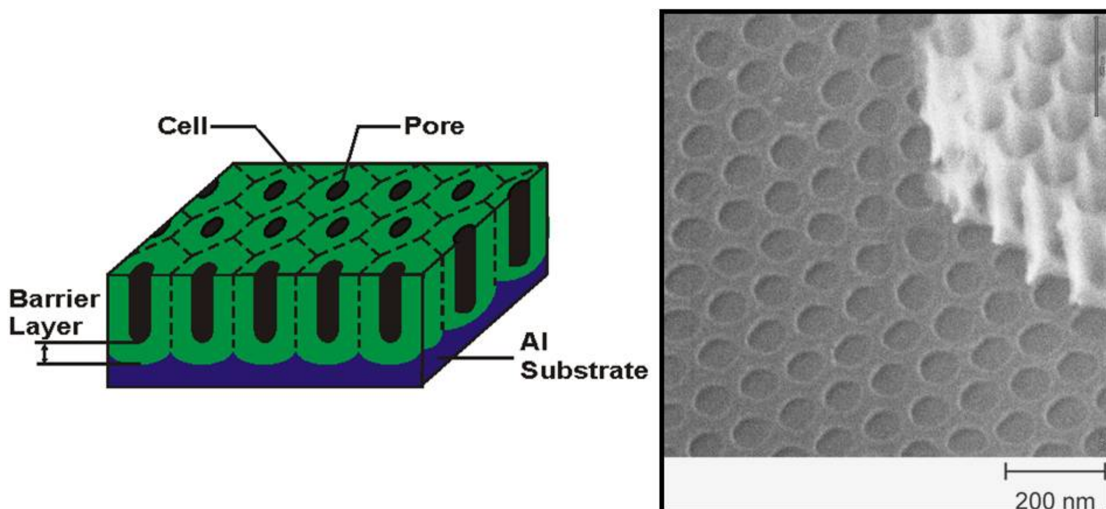


**Figure 2.5.** (a) Schematic of ordered anodic aluminum oxide (AAO). (b) An AAO film that has gone though the lift-off process onto a GaAs substrate. The GaAs has been etched through the AAO.

dimples in the Al foil where the pores once were. The Al foil is then anodized a second, shorter time, typically 3-5 minutes, depending on how thick of an AAO film is desired. For the silicon nanomeshes, the AAO was anodized in 0.3 M oxalic acid at 40 V at a temperature of 10 °C. The second anodization was done for 5 min, which yielded a 500 nm thick AAO film.

To be used as an etch template, the AAO must have the Al and barrier layer removed before being placed on the device layer for etching. This lift-off process is described by Masuda *et al.* [13]. Figure 2.5b shows an AAO film that has gone through the lift-off procedure and used to template a GaAs substrate. The substrate was subsequently etched through the AAO template transferring the AAO pore pattern into the GaAs.

For the lift-off process on the SOI device layer, the Al foil with the AAO on top was cut into 3 mm x 3 mm pieces and a polymer film of collodion in amyl acetate was spun on top of one of the pieces to provide support and protection for the AAO during the lift-off procedure. This piece was then floated, AAO side up, in a Petri dish containing a solution of $HgCl_2$ dissolved in water. The Hg from the $HgCl_2$ forms an amalgam with the Al foil, removing it from the AAO. After the Al had been removed, the floating AAO film was transferred to DI water. The barrier layer from the bottom of the AAO film was then etched away by floating the film in a constantly stirred bath of 5 wt. % solution of phosphoric acid at 30 °C for 35 min. The film was then transferred to DI water again. The SOI substrate was held by tweezers and used to lift the floating AAO film out of the DI water such that the AAO rested on top of the device layer. After allowing the film to dry on the SOI, the sample was immersed in acetone to remove the protective polymer

coating such that a through-hole AAO template rested on the SOI device layer as shown in figure 2.2c.

The device layer was etched through the AAO template with a 500 eV $Ar^+$ beam from a VG Microtech EX05 ion source as shown in 2.2d. The device layer was etched at normal incidence with a current density of 0.5 mA/cm$^2$ for 90 min. The sample was then immersed in the 10:1 BOE for 15 min to remove both the AAO template and BOX layer, resulting in a free-standing nanomesh as shown in figure 2.2e. The resulting nanomesh was then cleaved into two pieces.

As was previously mentioned, one way to look at the nanomesh is that of an array of intertwining silicon wires that are 40-50 nm in diameter. To further reduce the dimensions of these silicon wires into the regime where quantum confinement effects (Si exciton Bohr radius ~4.5 nm) would be seen, one of the nanomesh halves was oxidized, as shown in figure 2.2f, based on a process of self-limiting oxidation [14-18]. In self-limiting oxidation, non-planar silicon surfaces such as dots, wires, pillars, *etc.*, are thermally oxidized at a temperature below 950 °C. Stress occurring between the Si and $SiO_2$ in the direction perpendicular to the Si/$SiO_2$ interface and increasing as the size of the remaining Si decreases causes the growth of the $SiO_2$ to stop before consuming all of the Si. This process is dependent upon the starting size and geometry of the initial silicon structure [17, 18]. Assuming the nanomesh was composed of Si wires that were ~ 40-50 nm in diameter, the oxidation of the nanomesh was carried out in a dry $O_2$ environment at 875 °C for 2 hrs. This was expected to yield Si wires ~10-25 nm in diameter encased in a high quality oxide [16].

## 2.4. ELECTRON MICROSCOPY RESULTS AND DISCUSSION

Figure 2.6a shows an SEM image of the handle side of the device that has been through the entire fabrication process up to, but not including, the final self-limiting oxidation step. In the figure shown, openings can be seen etched into the handle layer by TMAH. The typical pyramidal pit that results from the anisotropic etching is very truncated due to the thinness of the sample (20 μm) and the size of the openings in the etch mask (60 μm x 60 μm). Figure 2.6b shows a higher magnification TEM image of the Si membrane spanning one of the openings. A highly ordered hexagonal array of nanopores can be seen in the membranes. It can be seen that some of the holes are not perfectly round with the deformations possibly resulting from deformation in the AAO etch mask. In addition contrast differences can be seen around the edge of some of the holes that may be a result of sputter redeposition around the edge of the whole or damage to the Si crystalline structure from the ion beam during the dry etching step.

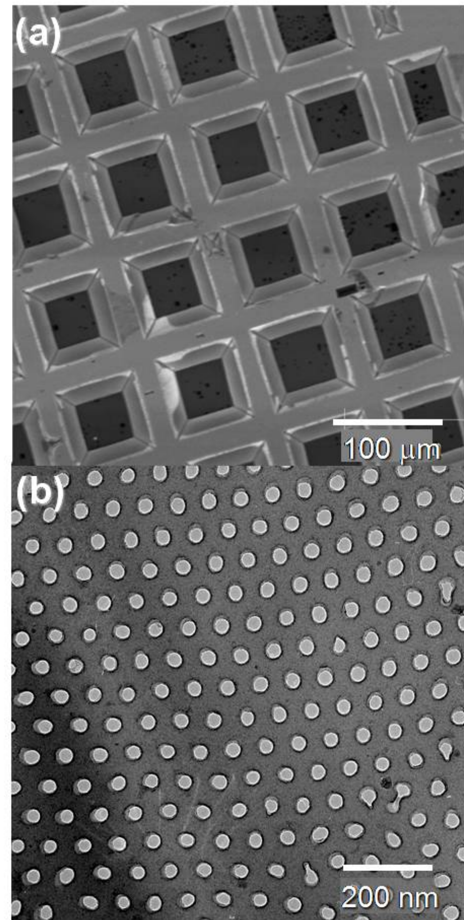


**Figure 2.6.** Electron microscope images of free-standing silicon nanomeshes. (a) SEM image of openings wet-etched into the handle layer (from back side). (b) Bright-field TEM image of unoxidized nanomesh (top side) spanning an opening in the substrate.

Figure 2.7a shows a secondary electron image (SEI), which shows information on the surface of the nanomesh, showing the nanopore array in the free-standing nanomesh. The average diameter of a nanopore is approximately 48 nm. Figure 2.7b shows a transmitted electron image (TEI) of the same area which takes into account both the top and bottom of the nanopore. The average nanopore diameter for the TEI image is approximately 60 nm. From both the SEI and TEI measurements, the taper of the nanopores is calculated to be approximately 7° and is shown schematically as an inset in figure 2.7b. 2.7c and 2.7d show SEI and TEI images, respectively of the oxidized nanomesh. The TEI image clearly shows the oxide rings that formed around the nanopores. The average radial thickness of the oxide rings is approximately 15 nm and in some areas of the mesh the oxide rings are almost touching. Using the intertwining Si nanowires model of the nanomesh, the lateral dimensions of the nanowires are from near zero to 30 nm.

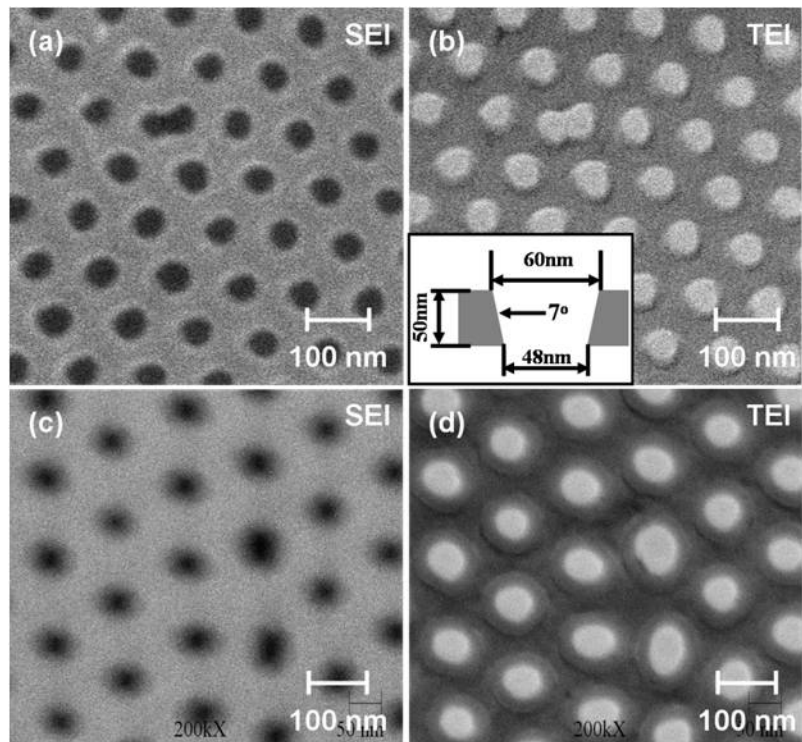


**Figure 2.7.** (a) SEI image of unoxidized Si nanomesh. (b) TEI image of unoxidized nanomesh with schematic of nanopore taper inset. (c) SEI image of oxidized nanomesh. (d) TEI image of oxidized nanomesh showing rings of oxide around the nanopores.

Figure 2.8a shows a bright-field TEM image of an oxidized nanomesh. The oxide rings can clearly be seen around the nanopores. Inset is a dark-field TEM image of the same nanomesh. In the dark-field image, one of the diffracted beams from the crystalline Si is used to form the image and all other beams, including the transmitted beam are excluded by an objective lens aperture. As a result, the areas of bright contrast represent the crystalline silicon while the oxide rings show up as areas of dark contrast with the holes showing up as completely black. This illustrates the amorphous nature of the oxide rings. Figure 2.8b shows a high-resolution TEM (HRTEM) image of an oxidized nanomesh. Two-directional lattice fringes can be seen in the silicon, indicated by the inset, confirming its crystalline nature. The oxide rings exhibit no lattice fringes, indicating that they are amorphous.

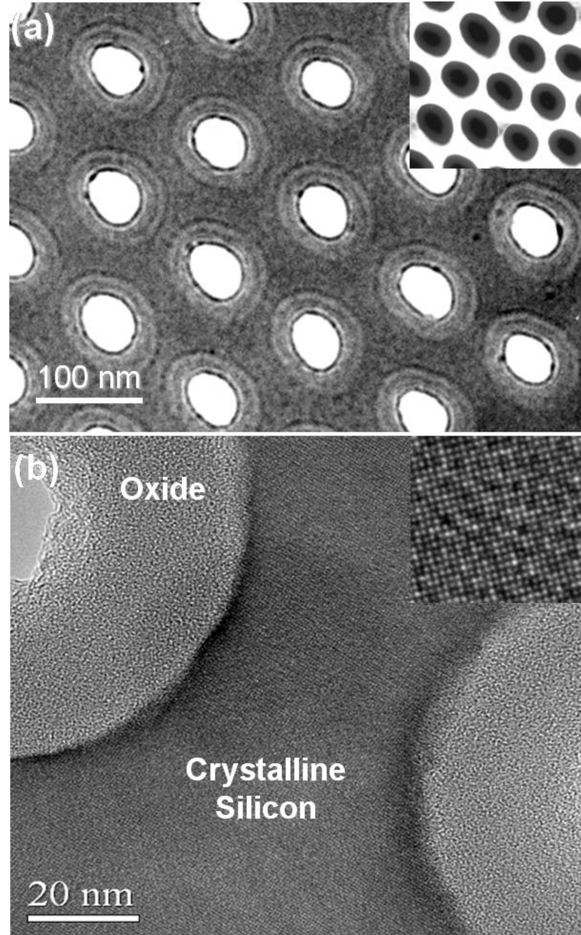


**Figure 2.8.** TEM images of free-standing silicon nanomesh. (a) Bright-field image of oxidized mesh delineating crystalline SI and silicon oxide regions. Inset is a dark-field image showing the hole (black), the amorphous nature of the oxide (gray) and the crystalline silicon (white). (b) High-resolution TEM image of an oxidized nanomesh showing crystalline Si encapsulated by high-quality oxide. Inset is a magnified view of lattice fringes in the remaining Si.

Using bright-field TEM imaging, the lateral dimensions of the Si wires we determined by measuring the distance between oxide rings. However, during the

oxidation step, the nanomesh is also oxidized in the direction normal to the plane of the nanomesh, thereby reducing the thickness of the silicon in the nanomesh. Convergent beam diffraction (CBD) was used to determine how much the silicon was oxidized in the direction normal to the plane of the nanomesh. In CBD, the TEM illumination system is set up in such a way that a small, highly convergent electron beam impinges upon the sample. In this mode, the diffraction pattern consists of broad discs instead of sharp spots. The intensities of these discs are dependent on the thickness of the diffracting material, in this case the silicon, and are measured from the recorded diffraction pattern. Using an estimated thickness of the silicon, the theoretical intensities of the discs are calculated and compared to the experimentally measured values. This is done in an iterative manner to fit the theory to the experimental results allowing the thickness of the sample to be determined. Figure 2.9a shows a TEM image of an oxidized Si nanomesh with four regions, labeled A-D, where CBD was performed. The size of the regions from which the CBD patterns were taken

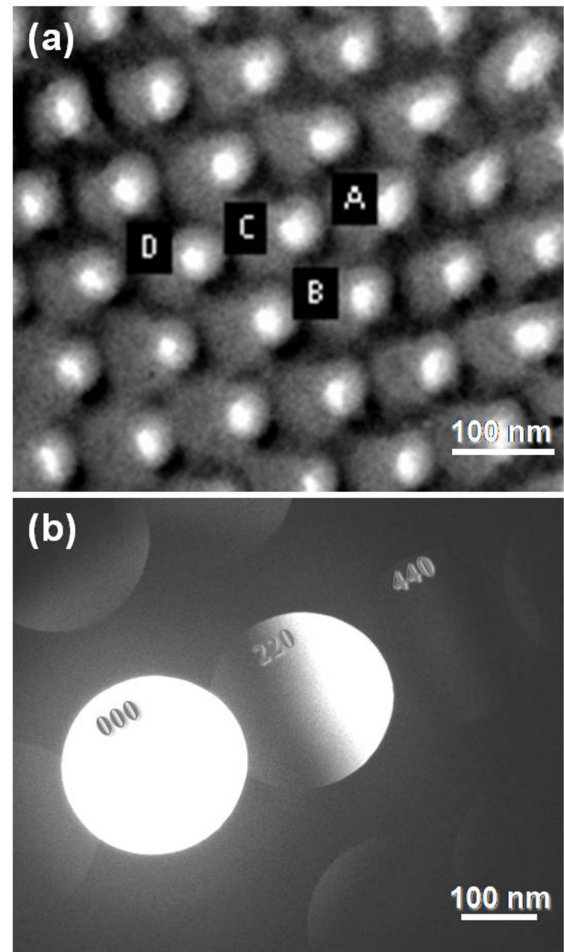


**Figure 2.9.** (a) TEM image of encapsulated Si nanomesh after oxidation. (b) Convergent beam diffraction (CBD) pattern used to determine the thickness of the Si. The Si thickness at position A, B, C, and D is 12.1, 14.0, 13.7, and 15.3 nm, respectively.

is on the order of a few nanometers. Figure 2.9b shows a representative CBD pattern taken from the nanomesh. The CBD pattern has been indexed showing which diffracting crystal planes of the silicon correspond to which disc. From the CBD measurements the thickness of the silicon at points A, B, C, and D was found to be 12.1 ± 0.4 nm, 14.0 ± 1.0 nm, 13.7 ± 1.0 nm, and 15.3 ± 1.0 nm, respectively. This yields a thickness of approximately 12-14 nm of oxide on both the top and the bottom of the nanomesh. This result is similar to the measured radial thickness of the oxide rings around the nanopores. From both the CBD and TEM measurements, it is determined that the cross-sectional dimensions of the silicon wires has been reduced from 40 nm x 50 nm (height x width) to roughly 14 nm x 20 nm. This is in good agreement with dimensions expected from the chosen self-limiting oxidation parameters.

The size of the remaining silicon in the oxidized nanomesh is anticipated to be still too large to see quantum confinement effects. Similar oxidized nanomeshes that are not free-standing have shown weak, broad photoluminescence peaks centered near 600 and 800 nm [19]. Further oxidation of free-standing nanomeshes could move the nanomeshes further into the quantum confinement size regime. This combined with the free-standing nanomeshes' ability to be characterized by TEM will be useful in the future for studying quantum confinement in silicon.

## 2.5. CONCLUSIONS

Free-standing Si nanomeshes that can be characterized by TEM have been demonstrated through a combination of photolithography, wet anisotropic etching, porous anodic aluminum oxide templates, and dry etching techniques. Electron microscopy results show ordered nanoporous silicon membranes spanning 45 μm x 45 μm openings

in the substrate. The nanopores in the membrane are arranged in a 2D hexagonal close packed array with a nanopore diameter of approximately 50 nm and a center-to-center spacing of approximately 100 nm. In addition to the porous membrane model, the nanomeshes can be thought of as intertwining Si nanowires. Subsequent self-limiting thermal oxidation has reduced the cross-sectional dimensions of these wires by approximately 60% in a controlled manner. Further self-limiting oxidation could reduce the wire dimensions even more, bringing them closer to the quantum confinement size regime for silicon.

### 2.6. ACKNOWLEDGEMENTS

The author would like to thank Dr. Preston Larson for his work on this project, especially in the AAO pattern transfer process and SEM work, Kevin Hobbs for growth of the AAO, Dr. Guoda Lian for TEM imaging, and Dr. Bin Jiang at Arizona State University for CBD. In addition, the author would like to thank SIMGUI Technology Co., Ltd., China for providing the SOI used in this research.

# CHAPTER 3:

# CHARACTERIZATION OF $Mn^{2+}$ DOPED ZnSe BRANCHED QUANTUM DOTS

## 3.1. ABSTRACT

Colloidal $Mn^{2+}$ doped ZnSe branched quantum dots, referred to as d-dots, have been characterized by a combination of TEM and energy dispersive spectroscopy (EDS). Bright-field TEM imaging of the d-dots shows a branched structure with four pod-like structures attached to a central core. High-resolution TEM (HRTEM) analysis shows that all four pods and the core possess a zinc blend crystal structure with the four pods having a crystallographic relationship to the core. Energy dispersive spectroscopy (EDS) of the d-dots reveals that the pods are composed solely of Zn and Se while the Mn is confined to the core of the d-dot which also contains Zn and Se.

## 3.2. INTRODUCTION

Colloidal quantum dots are semiconductor crystals on the scale of a few nanometers that are suspended in a liquid medium. Because of their small size, quantum dots display quantum confinement effects. This results in quantum dots having a band gap that is tunable depending upon the size of the quantum dots [20]. Such quantum dots

therefore have some very appealing optical properties. Quantum dots have applications in light emitting devices (LEDs) [21], solar cells [22], and biological markers [23]. Because of their simplicity of fabrication, quantum dots are of commercial interest. One of the problems that will have to be overcome for biological applications of quantum dots is that many quantum dots contain cadmium, which is particularly toxic to life.

Two areas of recent interest in quantum dots are branched quantum dot structures [24, 25] and doped quantum dots [26-29]. $Mn^{2+}$ doped ZnSe quantum dots, referred to as d-dots, are of particular interest because (1) they lack cadmium making them better suited for biological applications, (2) they posses a more complex shape than a typical quantum dot, and (3) the $Mn^{2+}$ doping produces high luminescent efficiencies.

In this chapter, the first crystallographic and compositional characterization using a TEM of novel $Mn^{2+}$ doped ZnSe colloidal quantum dots (d-dots) is discussed. These d-dots are novel in that not only are they doped but also they posses a complex shape. HRTEM imaging of the d-dots shows a branched, crystalline structure with four pod-like structures attached to a central core. All four pods and the core possess a zinc blend crystal structure with the four pods having a crystallographic relationship to the core. Energy dispersive spectroscopy of the d-dots reveals that the pods are composed solely of Zn and Se, while the core contains both Zn and Se along with Mn.

### 3.3. TEM ANALYSIS

A schematic of a $Mn^{2+}$ branched quantum dot is shown in figure 3.1. These d-dots consist of an approximately 2 nm diameter inner core of $Mn^{2+}$ doped ZnSe surrounded by a shell of undoped ZnSe. All together the d-dot core structure is

approximately 5 nm in diameter. As can be seen on the schematic, four pod-like structures branch off from the core and are composed of ZnSe.

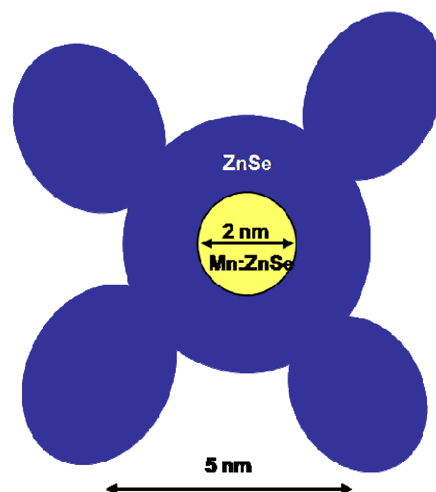

**Figure 3.1.** A schematic of the branched d-dot structure showing four pods attached to a central core.

Aliquots of the branched d-dots suspended in chloroform were provided for characterization by TEM. Details of the d-dot synthesis procedure are described in Viswanatha, *et al.* [30]. Drops of the colloid from the aliquots were transferred via pipette onto an ultra-thin carbon over holey-carbon TEM grid purchased from Ted Pella, Inc. The grid was then allowed to dry for several minutes. Before introducing the grid into the TEM column, the grids were dipped into a vial of pure chloroform for 5 seconds to wash off any remnant materials from synthesis. This helped to reduce contamination in the TEM and improved imaging.

TEM characterization was carried out using a 200 kV JEOL 2010F field emission TEM. Figure 3.2 shows a low magnification bright-field TEM image of the d-dots. The image shows that the branched d-dots are tetrapod-like structures (a central core with four pods attached) and around 10–20 nm in width. Some d-dots are

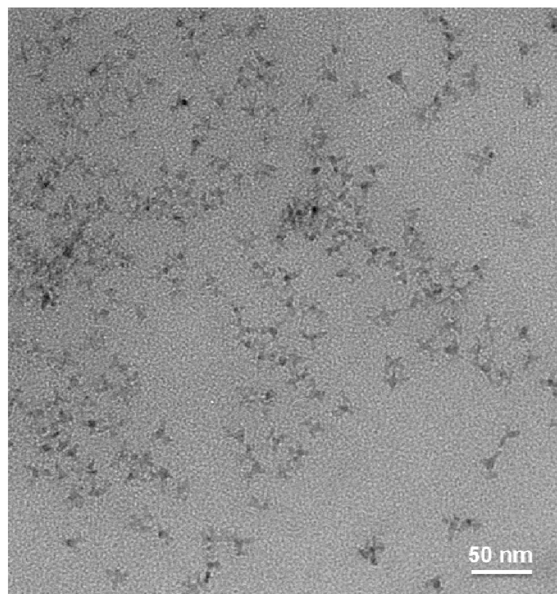

**Figure 3.2.** Bright-field TEM image of $Mn^{2+}$ doped ZnSe branched d-dots. Some of the d-dots are missing pods.

lacking all four branches. These branches have either broken off or were never formed. These results show that the structure of the d-dots deviates from previously reported, regularly branched CdSe and CdTe semiconductor tetrapod nanocrystals [24].

HRTEM and Fast Fourier transform (FFT) analysis were performed on the d-dots to study their crystallographic structure. Individual sections of the d-dot on the HRTEM image were cropped out using Adobe Photoshop CS2. These cropped images were circular and a Gaussian blur was done on the cropped images to prevent any streaks forming in the FFTs from the sharp edges of the

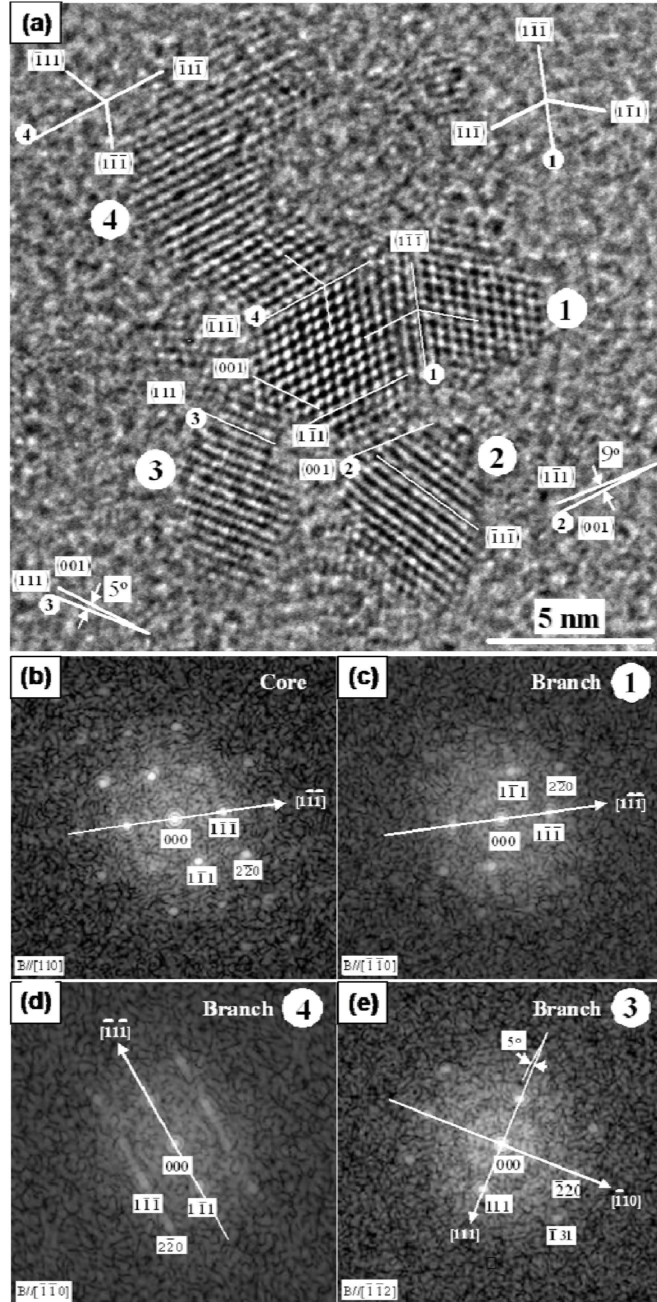


**Figure 3.3.** (a) High-resolution TEM image of a representative branched d-dot with four branches in crystallographic registry with the core. The branches are labeled 1 through 4. The crystal planes at the connections between the core and branches are superimposed on the image and thicker lined versions of these planes are labeled and positioned on adjacent areas off the quantum dot. (b) , (c), (d), and (e) Indexed FFTs of the core, branch 1, 4 and 3, respectively

cropped images. FFTs were then performed on the cropped images using Image J software. These FFTs were then indexed.

Figure 3.3 a shows an HRTEM image of a typical branched d-dot with a central core and four branches labeled 1 through 4. The core and branches are each a single crystal possessing a zinc blend structure, which was determined by looking at the symmetry and distance between reflections in the FFTs. The core, along with branches 1 and 4, show good 2-directional lattice while branches 2 and 3 show good 1-directional lattice. The crystal planes at the connections between the core and branches are superimposed on the core image and thicker lined versions of these planes are labeled and positioned on adjacent areas off the core. Figures 3.3b, c, d, and e show the FFTs of the core and branches 1, 4, and 3 respectively. The core is oriented [110] along the viewing direction. Branches 1 and 4 have a twinned relationship with respect to the core and are oriented [-1-10] along the viewing direction. Branches 1 and 4 share a {111} plane with the core. For branch 3, the [-1-12] direction of the branch is aligned with the [110] direction of the core. The (111) plane of the branch is inclined to the (001) plane of the core by 5°. For branch 2, the [110] direction of the branch is aligned with the [110] direction of the core. The (001) plane of branch 2 is inclined to the (1-11) plane of the core by 9°. While the crystallographic registry between branches 2 and 3 with the core is unusual, there is a definite crystallographic relationship.

## 3.4. ENERGY DISPERSIVE SPECTROSCOPY ANALYSIS

Energy dispersive (x-ray) spectroscopy (EDS) was carried out on the branched d-dots with a 300 kV FEI Titan S/TEM at Texas Instruments, Inc. Figure 3.4a shows a high angle annular dark field (HAADF) scanning transmission electron microscopy (STEM) image of a typical $Mn^{2+}$ doped ZnSe branched quantum dot. Areas 1 and 2 indicate where the electron beam was rastered while collecting the respective x-ray spectrum for each. Because of the small size of the d-dots, the electron beam was

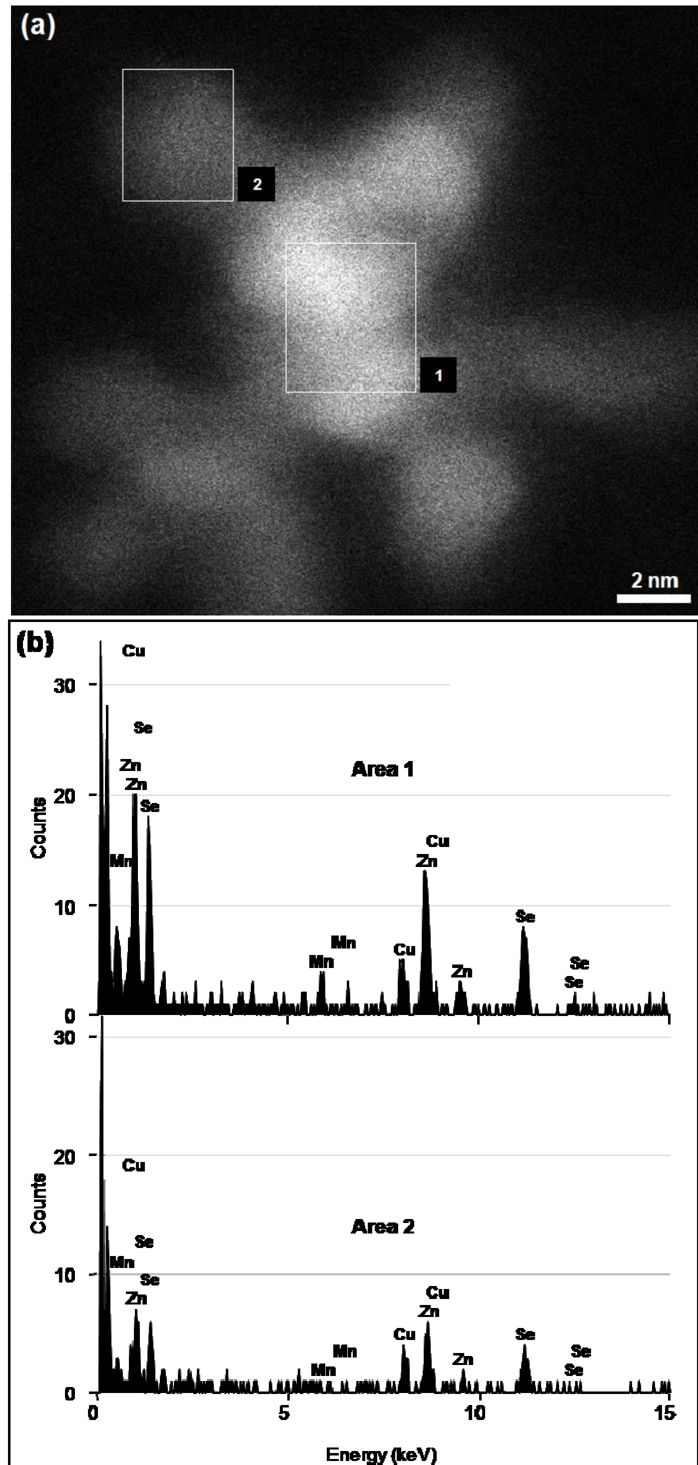


**Figure 3.4.** (a) High angle annular dark field (HAADF) scanning TEM (STEM) image of a branched d-dot. The two boxes represent the areas from which the beam was rastered to acquire x-ray spectra. (b) X-ray spectra from area 1 (core) and area 2 (branch).

rastered over each area for 2 minutes to collect as many x-rays as possible given the amount of drift that was occurring with the sample. Area 1 clearly includes the core of the d-dot while area 2 only includes a branch. Figure 3.4 b shows the EDS (x-ray) spectra obtained from each area. The peaks are labeled based on the energies of characteristic x-rays of the relevant elements. Area 1 shows the presence of Zn, Se, and Mn while area 2 shows the presence of Zn and Se but no Mn. EDS spectra were taken from cores and branches of three different d-dots. The results consistently showed Mn in the core but not the branches.

| | $K_\alpha$ Background Corrected Counts | | | $K_\alpha$ Bkg. Corr. Counts Normalized to Se | | |
|---|---|---|---|---|---|---|
| | Mn | Zn | Se | Mn | Zn | Se |
| | (25) | (30) | (34) | (25) | (30) | (34) |
| Core | 3 | 12 | 7 | 0.4 | 1.7 | 1 |
| Branch | 0 | 5 | 3 | 0 | 1.6 | 1 |

**Table 3.1.** Summary of the background corrected $K_\alpha$ x-ray counts from the x-ray spectra shown in figure 3.4b.

Table 3.1 summarizes the EDS data of the $K_\alpha$ x-ray lines for Mn, Zn, and Se. The left-hand side of the table shows the x-ray counts for each element that have been background corrected. The right-hand side of the table shows the same background corrected counts, but the counts have been normalized to Se. It should be noted that quantifying elemental percentages is difficult with such small structures that produce very few x-rays. Because of the small number of x-ray counts, little can be said about elemental percentages here. To quantify percentages would require many more x-ray

counts with a much longer acquisition time. The acquisition time, however, is limited by the amount of drift in the sample.

## 3.5. CONCLUSIONS

Novel $Mn^{2+}$ doped ZnSe branched d-dots have been characterized using TEM and EDS for the first time. HRTEM shows the d-dots are comprised of four, crystalline pod-like structures attached to a central crystalline core. HRTEM analysis reveals that all four branches and the core possess a zinc blend crystal structure with the branches in crystallographic registry to the core. EDS results show that the branches are composed only of Zn and Se, while the Mn is confined to the core which also contains Zn and Se. Such branched d-dots will be valuable in implementing and extending applications of quantum dots.

## 3.6. ACKNOWLEDGEMENTS

The author would like to thank Dr. Ranjani Viswanatha for synthesis of the d-dots, Dr. Guoda Lian at Texas Instruments, Inc. for performing the EDS, and Tetsuya Mishima for assistance with the HRTEM analysis.

# CHAPTER 4:

# CHARACTERIZATION OF CUBOID-SHAPED MICROCRYSTALS IN PbSe EPITAXIAL FILMS

## 4.1. ABSTRACT

Cuboid-shaped PbSe microcrystals (cuboids) in PbSe (111) epilayers grown on silicon substrates have been characterized using a combination of electron microscopy and electron diffraction. Plan-view scanning electron microscopy (SEM) of the cuboids show they posses flat cubic faces while cross-sectional SEM shows the cuboids extend a few microns into the epilayer. Electron backscatter diffraction (EBSD) and selected area diffraction (SAD) have determined that the exposed square face of the cuboids at the surface of the sample is a {100} plane. Cross-sectional bright-field transmission electron microscopy (TEM) of a cuboid shows the cuboid extending approximately 4.5 μm into the epilayer and tapering towards its root, dark-field TEM suggests the cuboid is not a perfect crystal along its length and might be strained.

## 4.2. INTRODUCTION

PbSe is a narrow band gap semiconducting material that is a key material used in infrared optoelectronic devices such as lasers and detectors [31-35]. Some studies have

been made on defects in MBE-grown PbSe layers [36, 37], but a thorough study of growth defects has not yet been conducted [38]. Recently, cuboid-shaped microcrystals have been observed in MBE-grown PbSe (111) films which have been previously associated with growth pits in the epilayer [38].

In this chapter, the characterization of PbSe cuboids in a MBE-grown PbSe (111) epilayer is discussed. SEM characterization shows cubic-faced structures, occurring both individually and in clusters, protruding from the surface of the epilayer. Cross-sectional SEM and TEM images show that the cuboids typically extend several microns below the surface of the epilayer and tend to taper towards the bottom of the structure. Electron backscatter diffraction shows that the exposed face of the cuboid is a {100} plane whereas the epilayer is a {111} plane. These results are confirmed by selected area diffraction. Dark-field TEM reveals the cuboid is not a perfect crystal along its entire length and may be strained in some areas. This is the first comprehensive study of the crystal orientation of PbSe cuboids.

## 4.3. GROWTH DETAILS

Growth of the PbSe epilayer is similar to that as described in Zhao, *et al.* [39]. The 6.5 µm layer of PbSe was grown by molecular beam epitaxy (MBE) on a Si (111) substrate with a 2 nm $CaF_2$ (111) buffer layer. The temperature of the Si substrate during growth was 400 °C and the growth rate was 2.6 µm/hr.

## 4.4. OPTICAL AND SCANNING ELECTRON MICROSCOPY RESULTS

Figure 4.1 shows optical microscopy images of the PbSe (111) epilayer surface. Defects in the epitaxial layer can be seen as bright spots in the dark background. These defects range in size from a few microns to around 15 microns with most of the large

ones possessing an irregular shape. The density of these defects was measured to be around 5 x $10^4$ $cm^{-2}$.

SEM imaging of the sample was performed at the University of Oklahoma using a JEOL JSM-6060, Zeiss 960A, and JEOL JSM-880 SEM. SEM revealed that the defects possess a cubic face that protrudes from the epilayer, hence the term cuboid. These cuboids can occur individually or in clusters. Figure 4.2a shows an individual cuboid in a PbSe epilayer. The cuboid's edges are approximately 1.5 μm in length. A small gap can be seen between the epilayer and the sides of the cuboid showing that the cuboid and the epilayer are not in epitaxial registry with each other. In addition, the corner of another cuboid can be seen protruding from the surface indicating that not all of the cuboids occur with a face parallel to the epilayer surface. While the cuboids displayed a varying degree of tilt relative to the epilayer surface, most of the individual cuboids were found to have a rectangular face that is fairly parallel to the epilayer surface. Figure 4.2b shows a large cluster of cuboids protruding from the sample surface. The gap around the cluster gives the appearance of a pit in which the cuboids grow. Experiments in blowing the epilayer surface with dry $N_2$ and

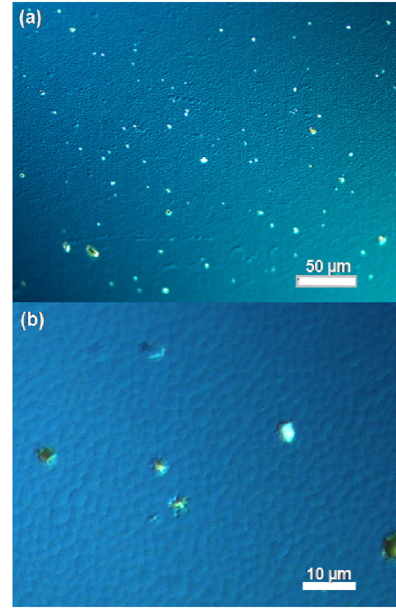


**Figure 4.1.** (a) Optical microscope image of cuboids in a PbSe (111) epilayer. (b) A higher magnification image of a group of cuboids

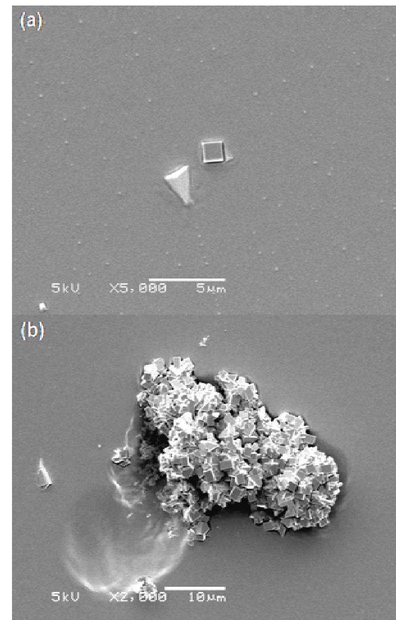


**Figure 4.2.** Plan-view SEM images of (a) an individual cuboid and (b) a cluster of cuboids

ultrasonication have shown that some of the cuboids can be easily removed from the epilayer [38]. These experiments have shown that the larger the cuboid, the deeper the pit left behind after the cuboid's removal. This suggests that the formation of the cuboids can occur at various points during growth.

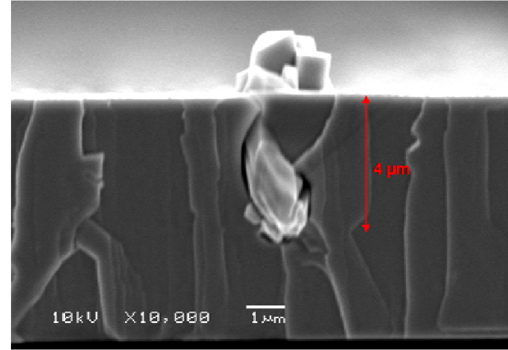


**Figure 4.3.** A cross-sectional SEM image of a cluster of PbSe cuboids showing the root structure of a cluster in the PbSe (111) epilayer.

Figure 4.3 shows a cross-sectional SEM image of the sub-surface structure of small cluster of cuboids that was exposed when the sample was cleaved. The epilayer is approximately 6.5 μm thick and the cuboids extend approximately 4 μm below the epilayer surface. The cuboids appear to taper towards the bottom of cluster's structure.

In addition to imaging with the SEM, EDS, which is sensitive to elemental composition, was performed on the cuboids and the epilayer. The results indicate that the composition of the cuboids is the same as the surrounding PbSe epilayer.

## 4.5. ELECTRON BACKSCATTER DIFFRACTION RESULTS

In order to determine the orientation of the exposed cuboid faces, electron backscatter diffraction (EBSD), which is an SEM technique, was employed. While there are other techniques that can be used to determine the crystalline orientation of materials, namely x-ray diffraction (XRD) and TEM techniques such as selected area diffraction (SAD), nanobeam diffraction (NBD), and convergent beam diffraction (CBD), EBSD offers some huge advantages. First, EBSD uses the electron beam of an SEM to probe the material in question, thus the orientation of small, individual crystallites down to 20

nm in size can be determined. This is an advantage over XRD which can only probe areas down to around 50 μm in diameter [40] and thus only gives orientation information about large populations of crystallites. In addition, EBSD can be performed on bulk samples and therefore does not require that the sample be thinned to electron transparency like those prepared for TEM diffraction techniques.

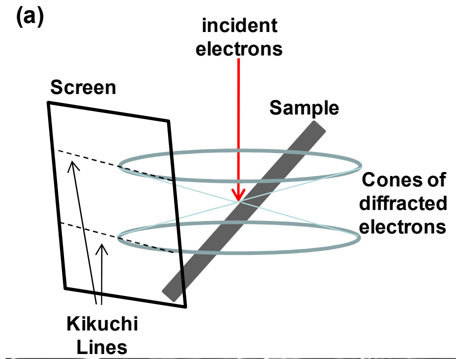


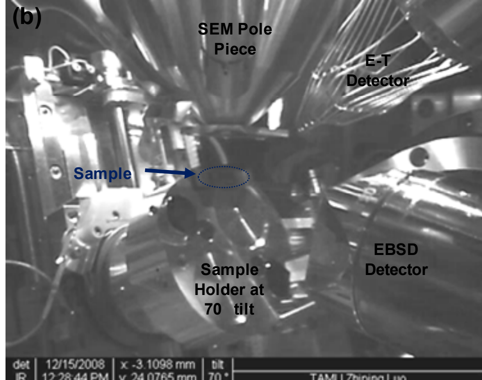


**Figure 4.4.** (a) Schematic of the concept of EBSD. (b) Optical mage of the inside of an SEM chamber equipped for EBSD.

Figure 4.4a illustrates the principle behind EBSD. The sample is first tilted at an angle of 70° to the electron beam. The electron beam impinges upon the sample and the electrons are inelastically scattered in all directions. Since the electrons are now travelling in all directions, some electrons will satisfy the Bragg equation for diffraction for each crystal plane in the sample. From each crystal plane the diffracted electrons form two conical surfaces. This occurs because the electrons are striking each crystal plane from every direction and are therefore also diffracted in every direction (as long as the Bragg equation is satisfied). There are two cones per plane since the scattered electrons from the primary electron beam strike each plane from every possible direction and thus electrons can be diffracted either from the top or bottom side of the plane. To detect these diffracted electrons, a phosphor screen is placed near the sample. Where the cones from the different planes intersect the phosphor screen, lines are formed on the screen

giving rise to the EBSD pattern. A CCD behind the phosphor screen records the pattern on the screen. In the EBSD pattern, the lines appear in pairs with each pair representing a crystal plane. These pairs of lines are called Kikuchi bands and are a result of the two cones produced from each crystal plane due to diffraction from both the top and bottom of the plane. The width of each Kikuchi band is inversely proportional to the d-spacing of the diffracting plane. In addition, the intersection of the Kikuchi bands correspond to zone axes of the crystal and the position of the Kikuchi bands and their intersection shift as the crystal orientation changes. This allows the EBSD pattern to be indexed and the orientation of the crystal to be determined.

Figure 4.4b shows an EBSD arrangement on an FEI Quanta 600 FESEM. The large tilt of the sample with respect to the SEM pole piece can be seen. The EBSD detector can be seen in the lower right of the image. The detector is brought within a few millimeters of the sample during acquisition of EBSD patterns but is retracted in the image for illustration purposes.

EBSD was performed on the cuboids at Texas Instruments, Inc. using a TSL (EDAX) orientational imaging microscopy (OIM) EBSD system on a Hitachi 4800S field emission SEM (FE-SEM). For the SEM an accelerating voltage of 20 kV was used along with a beam current of 20 μA and a working distance of 15 mm. Before acquisition of EBSD patterns from the sample, a background EBSD pattern of an amorphous material was taken. This background was subsequently subtracted from EBSD patterns acquired from the sample. Figure 4.5a shows a rectangular shaped cuboid protruding from the epilayer surface that was used for EBSD. Additional material can be seen around the cuboid that appears to be connected to the cuboid and not part of the epilayer. Figure

4.5b shows the same cuboid at a 70° tilt to the electron beam so that EBSD can be performed. Figure 4.5c shows a raw EBSD pattern taken from a single point on the cuboid. Although faint, the Kikuchi bands resulting from electrons diffracting from crystal planes in the cuboid can be seen. These bands were indexed by the TSL OIM Analysis version 4.6 software and the intersections of the bands labeled with the crystal zone axes of the cuboid as shown in figure 4.5d. The software used the pattern along with the sample tilt, tilt of the detector, etc. to determine the orientation of the cuboid. Three cuboids were examined and in all three the protruding flat face was shown to be a {100} plane. In addition, EBSD on the substrate confirmed the <111> orientation of the substrate.

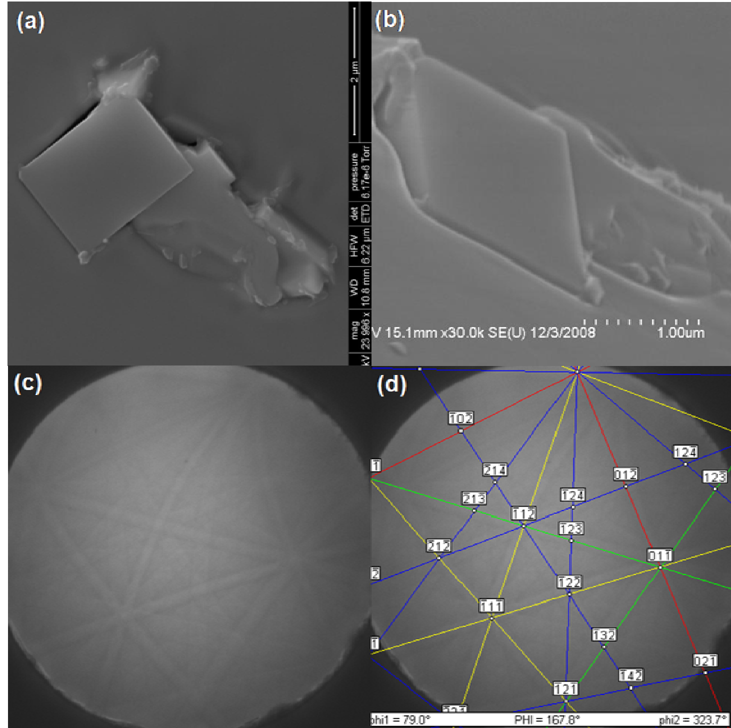


**Figure 4.5.** (a) Top down SEM image of PbSe cuboid. (b) SEM image of same cuboid at 70° tilt to the electron beam for EBSD. (c) Raw EBSD pattern from the cuboid shows a raw EBSD pattern taken from the cuboid. (d) Same EBSD pattern indexed by the OIM software.

To get a better idea of the crystallographic relationship between the cuboid and the epilayer, EBSD mapping was performed on the cuboid as shown in figure 4.6. The mapping was done by acquiring and indexing EBSD patterns from different points in a triangular array with a resolution of around 300 nm. The large size of the data points was chosen to deal with the effects of sample drift which can make higher resolution mapping

difficult. Figure 4.6a shows an SEM of the cuboid that was mapped at a 70° tilt with respect to the electron beam. Figure 4.6b shows an EBSD orientational map of the cuboid shown in 4.6a. The map has been compressed by 65 % to account for the tilt in the sample. Inset is an inverse pole figure which color codes the different possible orientations for the map. It can be seen that the substrate is blue, which according to the inverse pole figure means it is <111> oriented. The cuboid is colored red, indicating that it is of a <100> orientation. Since the cuboid face is not perfectly parallel to the substrate face, the cuboid deviates slightly from perfect <100> orientation, with respect to the epilayer surface, indicated by the pinkish hue of the cuboid. This is because the sample was aligned in the SEM using the surface of the epilayer. Figure 4.6c shows a map of the deviation of the cuboid orientation from perfect <100> orientation. Inset is an inverse pole figure with color banding showing progressive deviation from perfect <100> orientation (green) to 15° deviation (red). The deviation was found to be

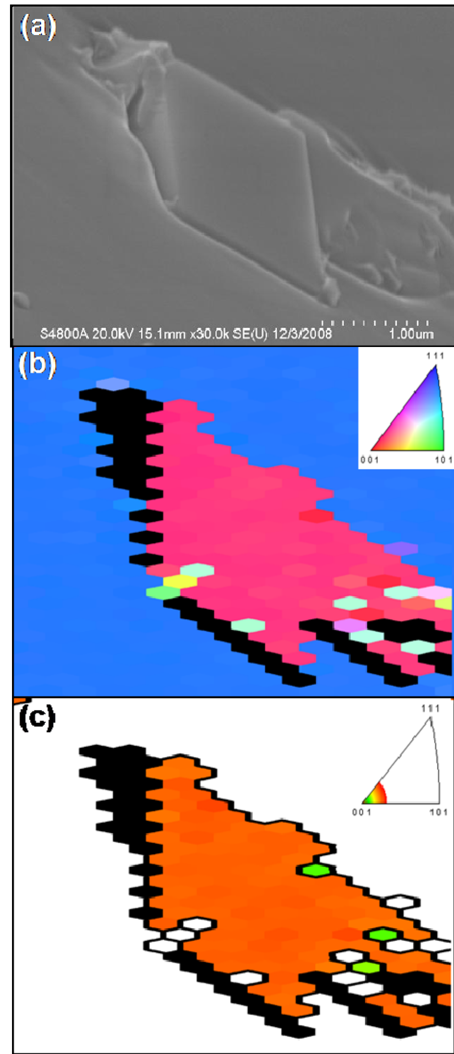


**Figure 4.6.** (a) SEM image of PbSe cuboid at with the sample surface tilted 70° to the electron beam. (b) EBSD orientation map of the image in (a) with an inverse pole figure inset used to determine orientation on the map. The EBSD map has been compressed vertically to match the SEM image of the cuboid due to the 70° tilt of the sample. (c) EBSD map of cuboid showing deviation of cuboid from perfect <100> orientation as a result of the cuboid face not being perfectly parallel to epilayer surface.

around 10-12° which is in agreement with the observed tilt of the cuboid face with respect to the epilayer surface.

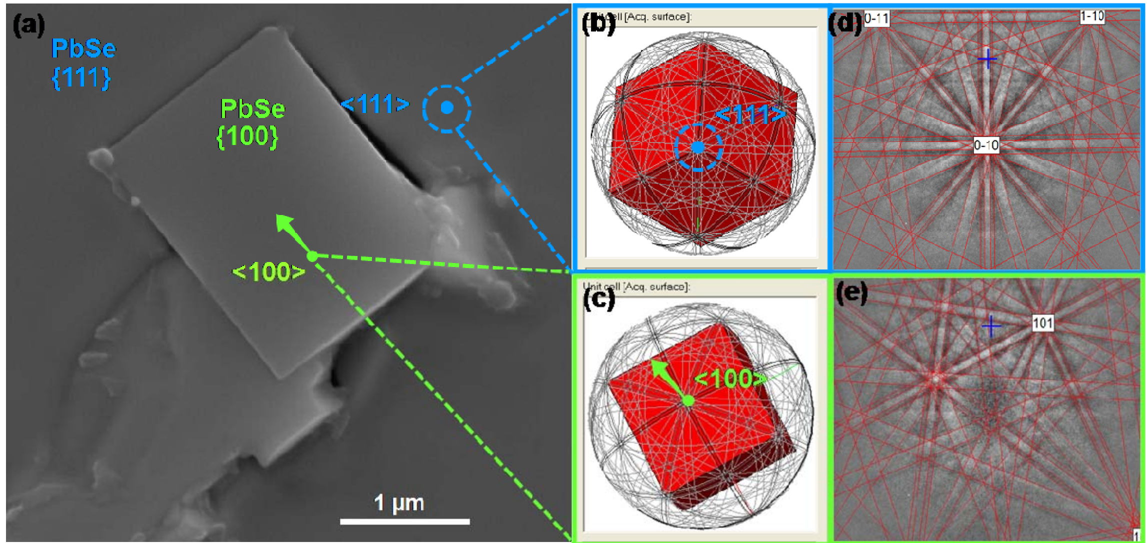


**Figure 4.7.** (a) Top down SEM image of a PbSe cuboid with the orientation of both the cuboid and epilayer labeled. (b) and (c) Software rendering s of orientation of unit cell f or epilayer and cuboid, respectively. (d) and (e) Indexed EBSD pattern s to determine unit cell in (b) and (c) , respectively.

In addition to the EBSD performed at Texas Instruments, Inc., EBSD was also performed at Texas A&M University using an HKL (Oxford) EBSD system with HKL Flamenco software on a FEI Quanta 600 FESEM. The results of the EBSD are shown in figure 4.7. Figure 4.7a shows the same cuboid analyzed in figures 4.5 and 4.6. The orientations of the cuboid and epilayer have been determined using the HKL EBSD system and are indicated on the image. Figures 4.7b and 4.7c show the calculated unit cell orientations for the epilayer and cuboid respectively. Figures d and e show the indexed EBSD patterns taken from the epilayer and cuboid respectively to determine the unit cell orientation shown in b and c. The results show that the exposed face of the cuboid is a {100} plane and the epilayer is a {111} plane. The results are in agreement with those from the EDAX system at Texas Instruments, Inc.

## 4.6. TRANSMISSION ELECTRON MICROSCOPY RESULTS

To investigate the structure of the cuboids below the epilayer surface, a cross-sectional TEM sample was prepared by using a focused ion beam (FIB) to cut out a thin section of the sample. This thin cross section was then mounted to a TEM grid using a lift-out process. FIB preparation of TEM samples is discussed in more detail in chapter 5. TEM was performed at the University of Oklahoma using a JEOL 2000FX TEM and a JEOL 2010F FE-TEM.

Figure 4.8a shows a bright-field TEM image of a cuboid. The cuboid protrudes above the epilayer top surface by about 0.5 µm and is approximately 4.5 µm in length. An approximately 0.5 µm layer of platinum was deposited as a protective layer during FIB preparation and can be seen in the image. Below the epilayer surface, one side of the top ¼ of the cuboid expands at a 10° angle from a line normal to the top face of the cuboid while the other side is approximately parallel with the normal. In the bottom ¾ of the cuboid, significant tapering towards the can be seen.

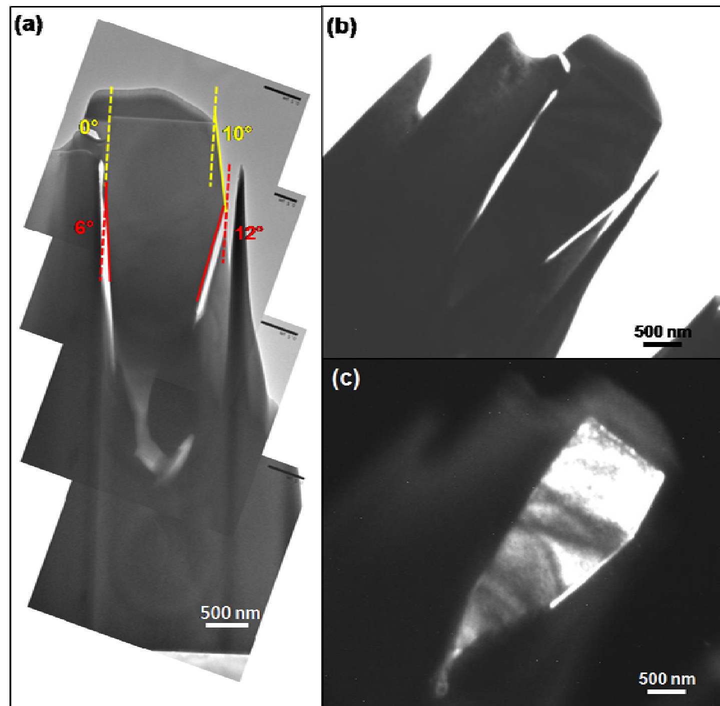


**Figure 4.8.** (a) Stitched bright-field TEM image of PbSe cuboid with the angles of the cuboid labeled. (b) Tilted bright-field TEM image of the PbSe cuboid. (b) Tilted dark-field TEM image of the PbSe cuboid.

One side of the cuboid tapers at a 12° angle from a line normal to the top face of the cuboid while the other side tapers at 6°. Figure 4.8b and 4.8c show a tilted bright-field and dark-field TEM image, respectively, of the cuboid. The cuboid was tilted as to strongly excite one of the reflections in the cuboid's selected area diffraction (SAD) pattern. An objective aperture was then centered on the optical axis to block any diffracted electron beams from contributing to the image. In the bright-field image, this gives rise to diffraction contrast. For the dark field image, the strongly excited diffracted spot was centered on the optical axis by using electrostatic tilts in the TEM. The objective aperture, which is still centered on the optical axis, now blocks all electrons except for those diffracted from the plane corresponding to the strongly excited diffraction spot. Since the cuboid and epilayer are of different crystallographic orientation, this gives a stark contrast difference between the cuboid and the surrounding epilayer as seen in figure 4.8c. Figure 4.8c also suggests that the cuboid is not a perfect crystal since the contrast varies across the cuboid. This contrast variation is likely due to strain in the cuboid. The largest contrast changes occur near the bottom of the cuboid and in areas where the sides of the cuboid change angle.

Figure 4.9a shows a bright-field TEM image of the top of the cuboid and the epilayer. Figures 4.9b and c are the SAD pattern and HRTEM image, respectively, from the epilayer. The indexed SAD pattern shows the epilayer to be <111> oriented, which is in agreement with the EBSD results. The HRTEM image shows 2-directional lattice fringes in the epilayer. Figures 4.9d and e are the SAD pattern and HRTEM image from the cuboid respectively. The indexed SAD pattern shows the cuboid to be <100> oriented, with respect to the top surface of the sample, which is also in good agreement

with EBSD results. In addition an extra spot in the lower left-hand corner of the image indicates the present of a possible defect in the cuboid. The HRTEM image shows strong 2-directional lattice fringes with some areas showing weak lattice fringes. This is most likely due to the sample becoming contaminated with crystallites (EDS indicates $CuCl_2$ as a possibility) during storage. Due to the contamination, which has been confirmed as crystalline, analysis of the HRTEM images for dislocations is not possible.

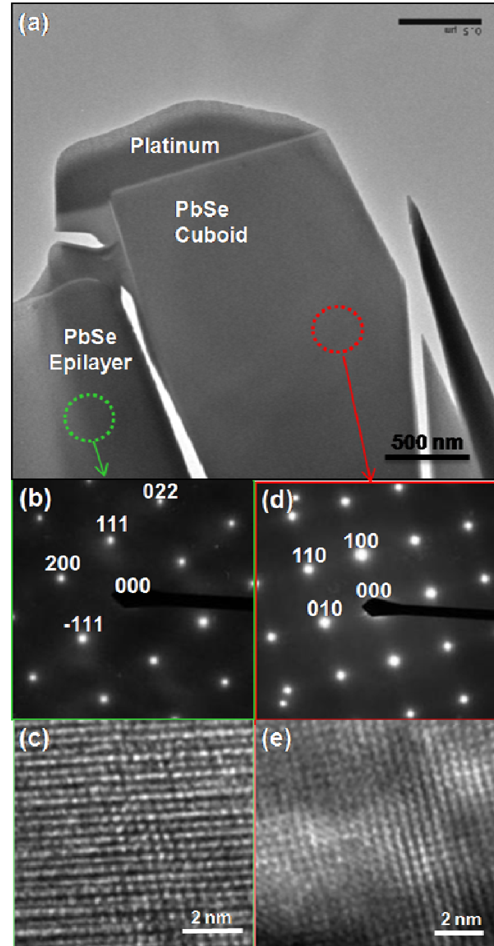


**Figure 4.9.** (a) Bright-field TEM image of the top of the PbSe cuboid. (b) and (c) PbSe epilayer SAD pattern and HRTEM image, respectively. (d) and (e) PbSe cuboid SAD pattern and HRTEM image, respectively.

It has been suggested that the origin of the cuboids is the result of growth around polycrystalline PbSe seeds occurring during growth of the epilayer with growth in the <100> direction being the fastest [38]. This would explain the prevalence of the cuboids exhibiting {100} faces at the surface of the epilayer. In order to investigate this, the root at the very bottom of the cuboid was imaged with TEM. Figure 4.10 shows a TEM image of the root. In the image a rectangular structure can be seen at the root. In addition, gaps between the cuboid and the epilayer can be seen. The root of the cuboid is not very electron transparent, which made HRTEM impossible in the root area. It should be noted that the best HRTEM imaging of the PbSe was along the edge of the TEM sample. This

is perhaps due to the sample being thinner along the edge from the FIB milling. However, the Si substrate portion of the sample was electron transparent enough to obtain HRTEM images anywhere in the Si. One issue that limits HRTEM of the PbSe cuboid and epilayer is the larger atomic number of Pb and Se compared to Si. This larger mass will decrease the electron transparency of the sample for a given thickness. In the future, uncontaminated and more electron transparent samples would permit HRTEM analysis of the root structure of cuboids. In addition nanobeam diffraction analysis of the cuboids would identify any changes in crystal orientation in different parts of the cuboids including the root area.

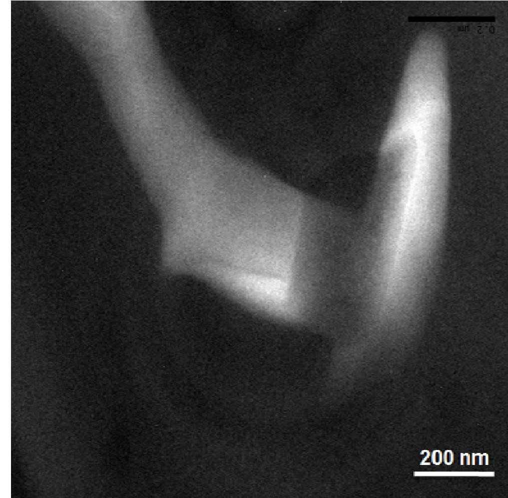


**Figure 4.10.** TEM image of the root at the bottom of the cuboid.

## 4.7. CONCLUSIONS

PbSe (100) cuboids in PbSe (111) epilayers have been oriented by EBSD and characterized cross-sectionally in a TEM. SEM characterization shows cubic faced structures occurring individually and in clusters protruding from the surface of the epilayer. Cross-sectional SEM and TEM show that the cuboids extend several microns below the surface of the epilayer and tend to taper towards the bottom. Electron backscatter diffraction and selected area diffraction show that the exposed face of the cuboid is a {100} plane compared to the {111} plane of the epilayer. Dark-field TEM shows the cuboid is not a perfect crystal along its length, possibly as a result of strain. Bright-field TEM imaging of the root structure of the cuboid shows gaps between the

cuboid and the epilayer at the root. In addition, an unidentified rectangular structure can be seen in the root area. In the future, with more electron transparent TEM samples, HRTEM analysis and nanobeam diffraction of the root structure of cuboids could yield more information on the origin of the cuboids.

### 4.8. ACKNOWLEDGEMENTS

The author would like to thank Dr. Jiangang Ma for growing the samples and performing the preliminary optical and SEM imaging, Dr. Cathy Vartuli at Texas Instruments, Inc. for performing the EDAX EBSD, Mr. Tom Stephens for assisting with the Oxford EBSD at Texas A&M University, and Dr. Mark Zurbuchen at Aerospace Corporation for FIB preparation of the cuboid TEM sample.

# CHAPTER 5:

# TEM AND NBD CHARACTERIZATION OF FERROELECTRIC RANDOM ACCESS MEMORY DEVICE CAPACITORS

## 5.1. ABSTRACT

Ferroelectric random access memory (FRAM) device capacitors have been prepared in cross section for TEM by careful focused ion beam (FIB) milling. Individual grains of the ferroelectric $Pb(Zr,Ti)O_3$ (PZT) layer from the capacitors have been characterized using TEM. The average size of individual PZT grains within the capacitors has been determined. Nanobeam diffraction (NBD) patterns have been taken from individual PZT grains and indexed, allowing the crystallographic orientation of the grains to be determined. The results indicate a preferential orientation of the PZT grains with either the a- or c-axis of the grain generally normal to the FRAM capacitor electrodes. In addition, high-resolution TEM (HRTEM) images of the PZT grains have been taken and show 2-directional lattice fringes. Fast Fourier transforms (FFTs) of these HRTEM images have been indexed as a supporting method to NBD for determining grain orientation.

## 5.2. INTRODUCTION

Ferroelectric random access memory (FRAM) is a form of non-volatile memory in which a ferroelectric layer between two capacitor plates is used to store a bit. In FRAM, the bit is stored as one of two opposing polarization states that can be switched in the presence of an external electric field. Once the external electric field is removed, the polarization remains until it is switched by an external electric field in the opposite direction [41]. One ferroelectric material that is heavily used in the fabrication of FRAM is lead zirconate titanate (PZT). Ferroelectricity in PZT arises from its crystal structure; therefore, crystallographic information about PZT in devices is important. One of the crystal structures of PZT that exhibits ferroelectricity is the tetragonal crystal structure [42]. In such a tetragonal structure the c-axis of the crystal is longer than the a-axis, and it is along the c-axis which the polarization occurs. The difference between the length of the c-axis and a-axis is small. For example, for PZT with a Zr/Ti ratio of 25/75, the c-axis is only 4% longer than the a-axis [43].

Preparation of good quality, crystalline cross-sectional TEM samples of PZT by focused ion beam (FIB) milling has previously been problematic resulting in amorphous PZT layers. While TEM can be performed on amorphized samples, information about the grain structure is difficult to obtain due to loss of crystallinity. In addition, determining the crystallographic orientation of grains that have been amorphized is impossible. Even if quality crystalline PZT samples are prepared, many techniques used to obtain the crystallographic orientation on the PZT have some important limitations. For example, X-ray diffraction (XRD), which is often employed to study crystalline samples, gives crystallographic information only on large populations of grains, and it is

inappropriate for fully fabricated FRAM devices in which the PZT may be below many other layers of material. Selected Area Diffraction (SAD), a TEM-based technique, which uses a physical aperture in the image plane of the objective lens to select an area of the sample, is limited to an area of around 400 nm in diameter [44] and thus, depending on the PZT grain sizes and other layers present in the device, cannot select an individual grain of PZT and determine its crystallographic orientation. Parallel Nanobeam diffraction (NBD) is a TEM technique that provides a straight forward means of determining the orientation of individual PZT grains. Areas as small as 10 nm in diameter can be probed and the diffraction patterns produced can be interpreted in the same manner as SAD [45].

In this chapter, a brief background on ferroelectric random access memory (FRAM) will be given followed by a detailed discussion on TEM analysis of PZT in FRAM device capacitors. Careful focused ion beam preparation has allowed TEM and high-resolution TEM (HRTEM) imaging of PZT grains within an FRAM device capacitor. From this imaging, the average size of the PZT grains within several different types of FRAM capacitors has been determined. In addition, NBD has enabled determination of the crystallographic orientation of individual PZT grains within a capacitor, showing a preferential orientation of the grains to the capacitor electrodes. HRTEM images of the grains show 2-directional lattice fringe and fast Fourier transforms (FFTs) of the HRTEM images of individual grains have been analyzed to orient the grains in support of the NBD measurements.

## 5.3. FERROELECTRIC RANDOM ACCESS MEMORY

Ferroelectrics, which are electric analogs to ferromagnetics, are materials that posses a spontaneous polarization, which can be reversed by an applied electric field. The reversal of the polarization is non-linear and hysteretic. These ferroelectric properties are destroyed above a certain temperature, dependent upon the material, called the Curie temperature. In addition, the electric dipoles in the ferroelectric material are organized into volumes of like polarization called domains. Ferroelectric materials also exhibit pyroelectricity and piezoelectricity as illustrated by the Venn diagram shown in figure 5.1 [46]. Pyroelectrics are materials that have a spontaneous polarization that increases with temperature until the Curie temperature for the material is reached. This polarization is not necessarily switchable in an external electric field because the electric field needed to switch the polarization exceeds the breakdown field of the material. If the polarization is switchable then the material is also considered a ferroelectric. Piezoelectric materials, which are materials that exhibit a change in polarization due to applied mechanical stress, encompass both pyroelectric and ferroelectric materials. Examples of some important ferroelectrics include potassium sodium tartrate (Rochelle salt), lead zirconate titanate (PZT), strontium bismuth tantalate (SBT), and barium titanate [47].

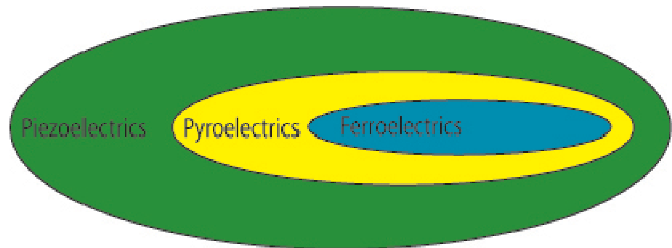


**Figure 5.1.** A Venn diagram showing the relationship between ferroelectrics, pyroelectrics, and piezoelectrics.

Out of all ferroelectric materials, PZT is of particular interest because of its use in the FRAM industry. PZT has a low deposition temperature (< 600 °C) and large polarization (> 30 μC/cm$^2$) [48]. PZT possesses a perovskite crystal structure which takes on the form $ABO_3$. A schematic of the PZT unit cell is shown in figure 5.2 a [49]. For this unit cell, the PZT has a tetragonal crystal structure with the c-axis longer than the a-axis. The central ion, either Zr or Ti, can move along the c-axis in response to an external electric field giving rise to a net dipole moment and thus a polarization along the c-axis of the crystal. Once the field is removed, the central ion stays in its shifted position (up or down) and thus there is a remnant polarization that will remain until an external electric field reverses it. This two state polarization is the basis for FRAM. It permits the storage of a bit, 1 or 0 and is illustrated in the plot of polarization vs. applied electric field shown in figure 5.2b [49]. The figure shows a hysteresis loop for a ferroelectric with $P_r$ being the remnant polarization (polarization after removal of external electric field) and $E_c$ being the coercive electric field (electric field strength required to flip the direction of polarization).

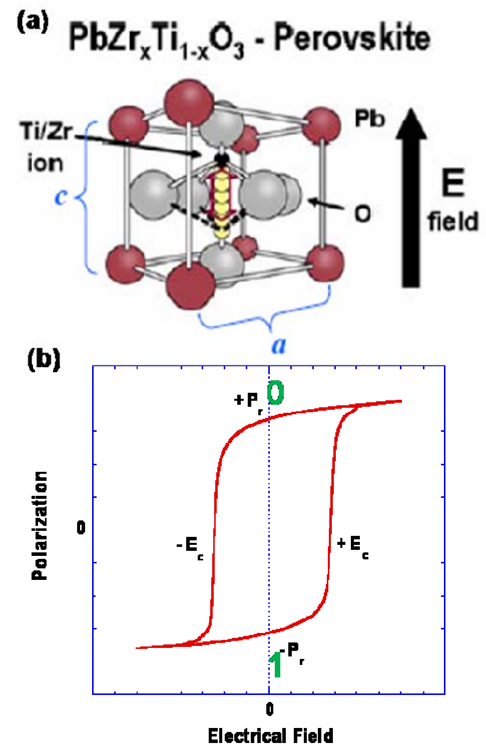


**Figure 5.2.** (a) Schematic of PZT unit cell. The central ion can move along the c-axis giving rise to a spontaneous polarization. (b) Plot of polarization vs. electric field for a ferroelectric showing hysteresis. A bit (1 or 0) is stored as the remnant polarization of the material once the electric field has been removed.

There are many types of computer memories in use today, with each having its own

advantages and disadvantages, which are summarized in table 5.1. FRAM is of particular importance because it is non-volatile (does not require constant power supply to maintain memory) and has low power consumption (~ 1.5 V). FRAM is similar in construction to the more familiar dynamic random access memory (DRAM). It consists of one transistor associated with one capacitor, but instead of a dielectric in the capacitor, a ferroelectric

| Memory Type | Advantages | Disadvantages |
|---|---|---|
| Static Random Access Memory (SRAM) | randomly access data, no refresh cycle, fast write time, low power | volatile, complicated structure, high cost |
| Dynamic Random Access Memory (DRAM) | randomly access bits, simple structure, low cost, fast read/write times | volatile, need refresh cycle, high power consumption, |
| Flash Memory | non-volatile, low cost per bit | high power consumption, slow, can not randomly erase data, low number of erase/write cycles |
| Magnetoresistive Random Access Memory (MRAM) | non-volatile, large number of erase/write cycles, low power | higher cost per bit, subject to stray magnetic fields |
| Phase Change Random Access Memory (PRAM) | non-volatile, large storage capacity, randomly erase data | long erase/write times, temperature sensitive, high cost per bit due to current density issues |
| Ferroelectric Random Access Memory (FRAM) | non-volatile, low power, fast read/write times | high cost per bit, use of “exotic” materials that can contaminate fabrication line |

**Table 5.1.** A comparison of different types of memories

material is used. Unlike volatile DRAM, which stores a bit as either a charged or uncharged capacitor, non-volatile FRAM does not require a constant refresh cycle to replenish leaked charge.

## 5.4. FABRICATION OF FRAM DEVICES

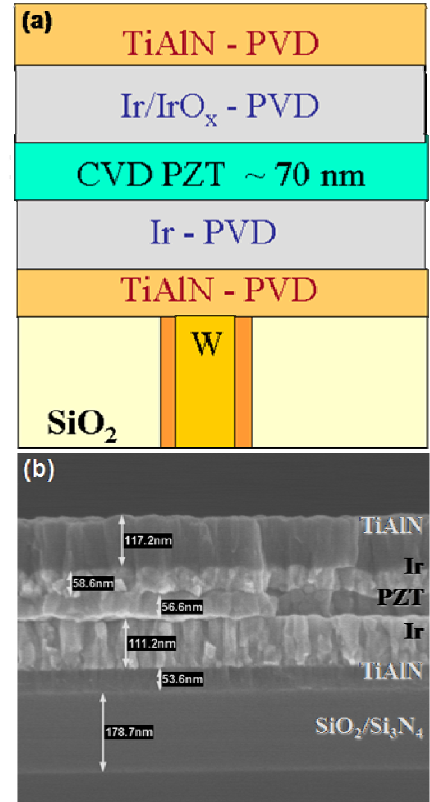


**Figure 5.3.** (a) A schematic of an FRAM capacitor. (b) SEM image of the capacitor without the W contacts.

FRAM device capacitors were fabricated by Texas Instruments, Inc. on 8" silicon wafers. The Zr/Ti ratio of the PZT film used in the FRAM was 25/75, which produces the desired tetragonal crystal structure of PZT. Growth details of the PZT are described elsewhere [50]. A schematic of the typical capacitor structure, with each layer and deposition method labeled, is shown in figure 5.3a [51]. As can be seen in the figure, the ferroelectric PZT layer, which is grown by metal-organic chemical vapor deposition (MOCVD), is located between two iridium capacitor electrodes. An SEM image of a capacitor structure is shown in figure 5.3b. The capacitor shown in figure 5.3b is what is known as a short flow capacitor in which one or more fabrication steps were left out. In this case the tungsten contacts were not fabricated. This is as opposed to full flow capacitors in which all of the fabrication steps have been performed.

## 5.5. FOCUSED ION BEAM PREPARATION OF TEM SAMPLES

TEM samples of FRAM capacitors were first cleaved from 8" wafers, shown in figure 5.4a, into approximately 2 cm by 2 cm pieces. The areas of interest were cut out of these pieces using a Disco DAD 321 automatic dicing saw such that a two-tiered cross-sectional piece of the sample resulted as shown in figure 5.4b. The top tier, which

is ~ 30 μm thick in cross section, is much narrower than the bottom tier and served as the starting point for FIB milling of an electron transparent cross-section using the H-bar method [52]. In the H-bar method, a small (~ 20 μm wide) area of sample is milled until a thin, electron transparent window of material remains. This window is supported on both ends by the bulk of the sample material. This is in contrast to the lift-out method, which involves milling the window free of the supporting bulk material.

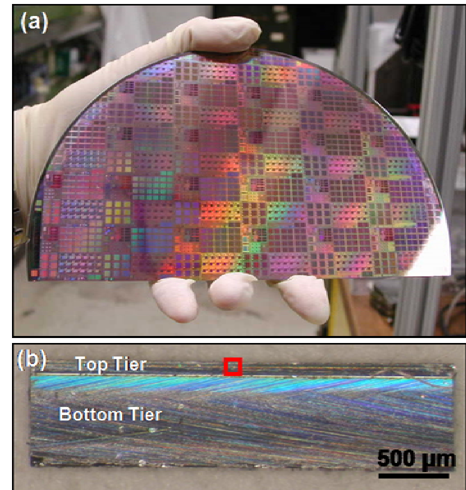


**Figure 5.4.** (a) Part of an 8" wafer onto which the FRAM modules have been fabricated. (b) A cross-sectional, two-tiered chip that has been cut from the wafer using a dicing saw. The red square indicates the area that will be further thinned by FIB.

After dicing, the samples were then coated with approximately 30 nm of gold in an Emitech table-top sputtering system to protect the sample surface from the ion beam before a much thicker and site specific platinum protective layer can be deposited in the FIB system. The samples were then loaded into an FEI 835 FIB dual-beam system. The term "dual-beam" is used because the instrument houses both an FIB and an SEM with the FIB at a 52° angle to the SEM as shown in figure 5.5 [53]. An FIB operates similarly to an SEM but uses gallium ions instead of electrons. These gallium ions are accelerated at a high voltage (~ 3-30 kV) and are focused with electromagnetic lenses.

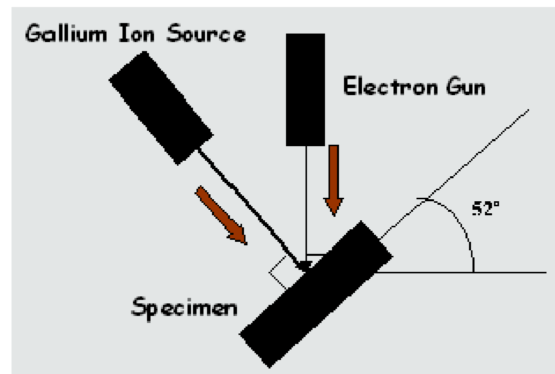


**Figure 5.5.** A schematic of a dual-beam FIB/SEM system.

The ion beam can then be directed across the sample surface using scan coils. The $Ga^{+}$ ions sputter material from the sample by momentum transfer and can also be used to image the surface of the sample due to ejection of secondary electrons, which can be collected by an Everhart-Thornley detector.

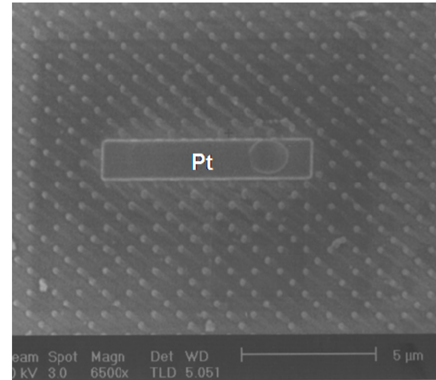


**Figure 5.6.** SEM image of a protective platinum strap deposited over the top to the FRAM capacitors. The dot structures on the surface are the top tungsten contacts of the buried capacitors.

Before FIB milling, a strip of platinum 20 µm long by 2 µm wide by 1 µm high, referred to as a Pt strap, was deposited in the dual-beam system by ion-assisted chemical vapor deposition on top of the area of interest. An example of a Pt strap is shown in figure 5.6. The purpose of the Pt strap is to protect the area of interest from ion damage during milling or imaging with the ion beam. Material was removed symmetrically in steps on either side of the Pt strap, starting at the edge of the top tier (see figure 5.4b), with each successive milling step performed at a lower beam current.

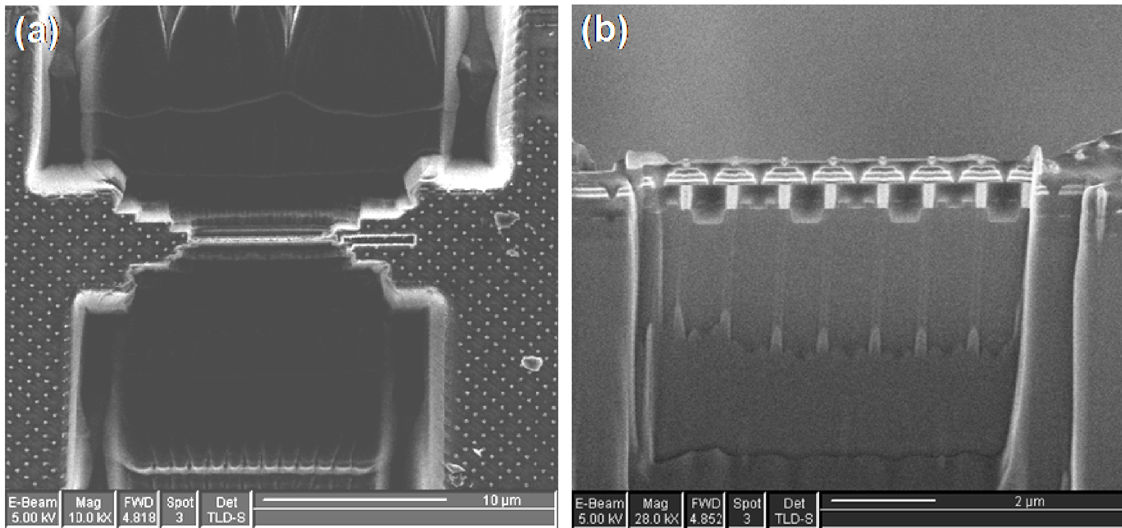


**Figure 5.7**. (a) Top-down SEM image of the FIB milled window. The step pattern leading to the window in the center can be seen. (b) A cross-sectional SEM image of the final electron transparent window showing a row of FRAM capacitors.

This is illustrated in the top down SEM image of one of the samples shown in figure 5.7a. In the image a series of successively smaller notches, where material was milled away, can be seen approaching the electron transparent window in the center. A 30 kV accelerating voltage was used for each of the milling steps and each successively smaller step in the milling process used an ion beam current at 7000, 1000, 300, 50, and 30 pA respectively. The final result was an electron transparent window that was ~ 80 nm thick. A cross-sectional view of the window is shown in figure 5.7b. At the top of the window a row of FRAM capacitors can be seen. At this point it should be noted that extreme care was taken not to approach the area of interest with too high of an ion beam current. Rather a more conservative approach was taken such that the highest current beam, the 7000 pA beam, was terminated before reaching the platinum strap. In addition, the final 30 pA milling step was terminated before most of the Pt and TiAlN, which lie above the PZT layer, was removed. This was done to minimize damage to the PZT layer. Figure

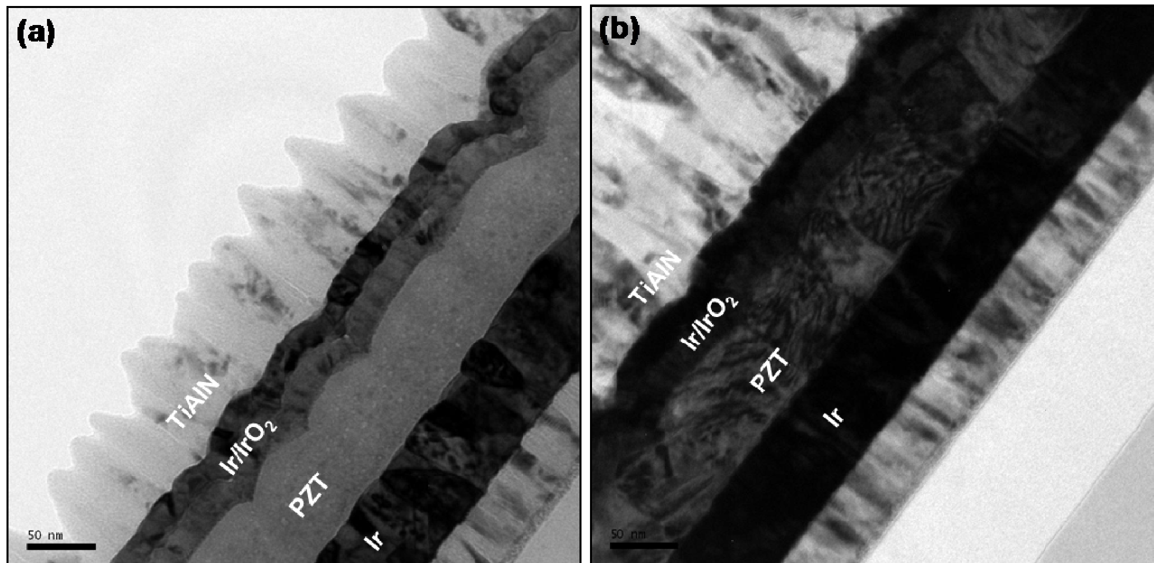


**Figure 5.8.** (a) An FRAM capacitor with an amorphous PZT layer due to FIB damage. (b) An FRAM capacitor from the same sample with crystalline PZT after careful FIB milling.

5.8 illustrates the difference in sample quality when using a more conservative approach. Both windows shown in figures 5.8a and 5.8b are from the same FRAM sample. The window in figure 5.8a was not prepared as carefully with the FIB as the window in figure 5.8b. The final 30 pA beam was allowed to mill the window in figure 5.8a more than in figure 5.8b. This can be seen by the fact that there is less TiAlN on top of the capacitor in figure 5.8a. As a result, the PZT in figure 5.8a is amorphous which can be seen by the lack of diffraction contrast as compared to figure 5.8b where the PZT is crystalline.

After the final and carefully performed 30 kV / 30 pA milling step, the surface of the window was tilted 60° degrees to the ion beam and was cleaned using a 3 kV / 30 pA beam for 20 sec. on each side of the window. This low voltage clean was to remove any ion damage layer from the surface of the sample which can be 15-25 nm thick. After the samples were removed from the FIB, each was mounted with G1 epoxy onto a copper TEM annulus that was 3 mm in diameter and with a 1.5 mm diameter opening.

## 5.6. TEM / STEM RESULTS

TEM/STEM was performed at Texas Instruments, Inc. using an FEI Titan S/TEM

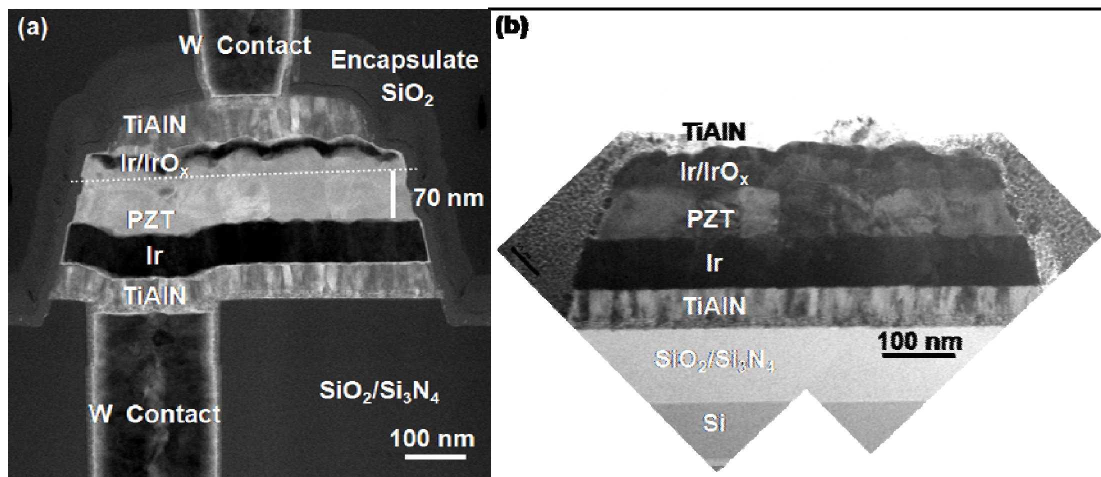


**Figure 5.9.** (a) High-angle annular dark-field (HAADF) scanning transmission electron microscopy (STEM) image of a complete FRAM capacitor. (b) Stitched bright-field TEM image of an FRAM capacitor. Individual grains of PZT can be seen in both images.

and at the University of Oklahoma using a JEOL 2000FX TEM and a JEOL 2010F FE-TEM. Figure 5.9a is a cross-sectional high-angle annular dark field (HAADF) STEM image that shows a fully fabricated (full flow) FRAM capacitor. Each layer within the capacitor stack is labeled. The PZT occupies the center of the capacitor stack. Individual grains of PZT can be seen in the capacitor. The PZT layer is approximately 70 nm thickness. This image marks the first time individual crystalline grains of PZT have been seen in an FRAM device capacitor prepared for TEM at Texas Instruments. Figure 5.9b shows a labeled cross-sectional bright-field (BF) TEM image of a partially fabricated (short flow) FRAM capacitor from a different wafer without tungsten contacts. Individual PZT grains can be seen in the image from diffraction contrast. This indicates

| Sample | Grain Height | Grain Width |
|---|---|---|
| Small Short Flow Capacitors | 65 ± 6 nm | 80 ± 30 nm |
| Small Full Flow Capacitors | 65 ± 6 nm | 80 ± 30 nm |
| Large Short Flow Capacitors | 70 ± 3 nm | 80 ± 30 nm |

**Table 5.2.** Comparison of grain sizes from different FRAM capacitors

that the PZT grains are crystalline and not amorphous. Several capacitors from the same sample as 5.9b were imaged in order to obtain a statistical picture of the size of PZT grains. From these images it was determined that the average height of a PZT grain is 65 ± 6 nm and the average width of a grain as seen in the cross-sectional slice was found to be 80 ± 30 nm. Several other FRAM samples were imaged and compared to see if there was any grain size difference among them. These samples included full and short flow

small capacitors (capacitor width ~ 500 nm) and short flow large capacitors (capacitor width ~ 20 μm). A comparison of grain sizes for these samples is shown in table 5.2. As can be seen from the table, no appreciable difference in grain size was found among the different FRAM samples.

## 5.7. NANOBEAM DIFFRACTION RESULTS

As was previously mention, NBD allows for diffraction patterns to be taken from small areas of the sample and these patterns can be interpreted the same as SAD patterns. The advantage of NBD over SAD is shown in figure 5.10. Figure 5.10a shows an image of an FRAM capacitor with the smallest selected area aperture available on the JEOL 2000FX inserted. As can be seen, several grains of PZT are within the area selected by the aperture as well as several other layers of material from the capacitor structure. Figure 5.10b shows the diffraction pattern taken from this area. As expected, there are many diffraction spots from all the crystallites within the area selected by the aperture. Figure 5.10c shows the NBD pattern taken from a single grain from the same capacitor. The diameter of the beam used to make the NBD pattern is indicated on figure 5.10a by the dashed red circle. The NBD pattern shows the presence

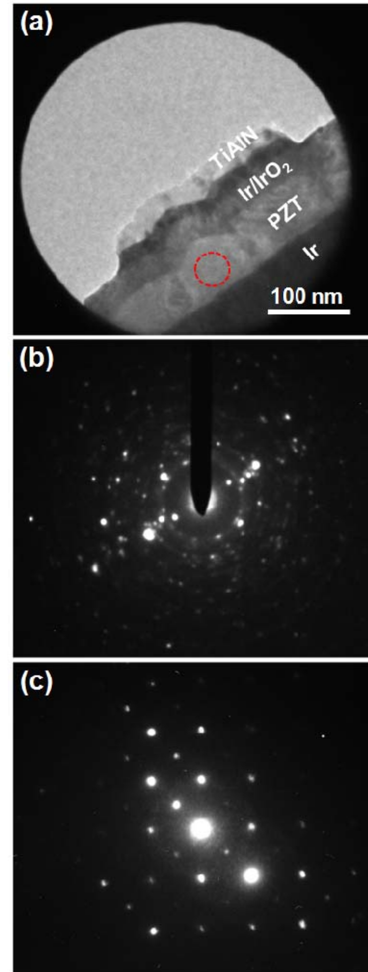


**Figure 5.10.** (a) TEM image of part of an FRAM capacitor with the smallest SAD aperture on the TEM inserted. (b) The SAD pattern taken from that area showing multiple crystallites. (c) NBD pattern taken from an individual grain in the capacitor showing a single crystal diffraction pattern. The diameter of the NBD beam used is indicated by the dashed red circle in (a).

of a single crystallite, thus making indexing and interpretation of the pattern much simpler than the SAD pattern.

NBD was performed using the same short flow sample as shown in figure 5.9b but on a different capacitor by using the TEM illumination system to create a small, parallel beam with a diameter of approximately 50 nm. This diameter beam is small enough to probe a single grain of PZT and obtain its diffraction pattern.

Figure 5.11 shows a bright-field TEM image of an FRAM capacitor. The upper right inset shows a PZT grain within that capacitor with its c-axis determined by NBD. The circle on the PZT grain shows the approximate size of the electron beam used to create the NBD pattern relative to the size of the grain itself. The lower left inset shows the NBD

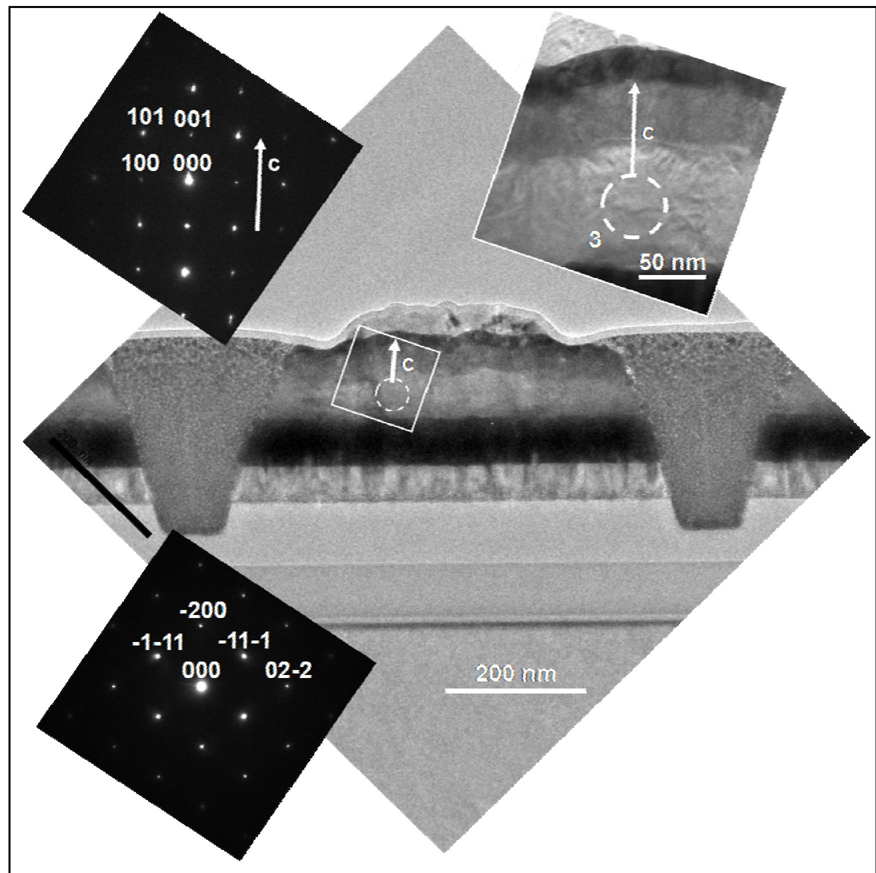


**Figure 5.11.** Bright-field TEM image of an FRAM capacitor. Inset (lower left) shows a NBD pattern from the Si substrate below the capacitor, used as an *in situ* calibration. Inset (upper left) shows the NBD pattern for the PZT grain indicated by the outlined box. Inset (upper right) is a higher mag. image of the outlined PZT grain (labeled grain 3), including an arrow indicating the c-axis. The dashed circle indicates the approx. diameter of the beam for the NBD pattern.

pattern taken from the silicon substrate far underneath the capacitor. This Si pattern provided an *in situ* method to account for any distortion in the PZT NBD patterns introduced by the TEM lenses which could affect the relative distance measurements of the diffraction spots on the NBD patterns. The silicon NBD pattern was indexed and the distances between opposing reflections were measured. The ratios of the measured distances between diffraction spots on the Si NBD pattern correspond to the inverse of the ratios between known d-spacings of Si. Comparing these measured and known ratios provides a way to quantify any distortion in the diffraction pattern. From these comparisons, it was determined that the distortion was around 1%. The upper left inset of figure 5.11 shows the NBD pattern taken from the PZT grain shown in the upper right inset. Since PZT possesses a tetragonal crystal structure, the c and a crystallographic axes can be determined by measuring the relative distance between diffraction spots and indexing the pattern. To measure the NBD patterns, Image J software was used to make 25 pixel wide line scans through pairs of opposing diffractions spots on each recorded NBD pattern to calculate average pixel intensity versus pixel position along the line scans. Using Origin 6.1 software, the data for each line scan was plotted and Cauchy-Lorentz curves were then fitted to the data. The center positions of the diffractions spots from each line scan were then extracted with sub-pixel resolution. The distance between opposing diffraction spots was calculated from these positions allowing the NBD pattern to be indexed and the a- and c-axes of the grain to be determined. The difference in length between the c-axis and the a-axis from the PZT NBD patterns was found to be around 2-4%. It should be noted that in some of the patterns, individual diffraction spots are elongated. The axis of the elongation was the same for all the spots in a given NBD

pattern. This type of elongation in the NBD patterns is thought to be associated with strain in the crystals [54].

NBD pattern analysis was carried out for several neighboring grains within a single capacitor. Figure 5.12 shows the same capacitor as shown in 5.11 with four neighboring PZT grains aligned within the capacitor. The associated NBD patterns used to determine the crystallographic orientation of each PZT grain are shown above the corresponding grain along with the TEM holder tilts used to obtain the pattern and the measured c/a ratio. The NBD patterns are rotated with respect to the TEM images to account for rotational differences between TEM and diffraction mode on the microscope. In addition, NBD patterns are slightly rotated with respect to each other due to slight sample misalignment between two different TEM sessions. The c and a-axes for grains 2

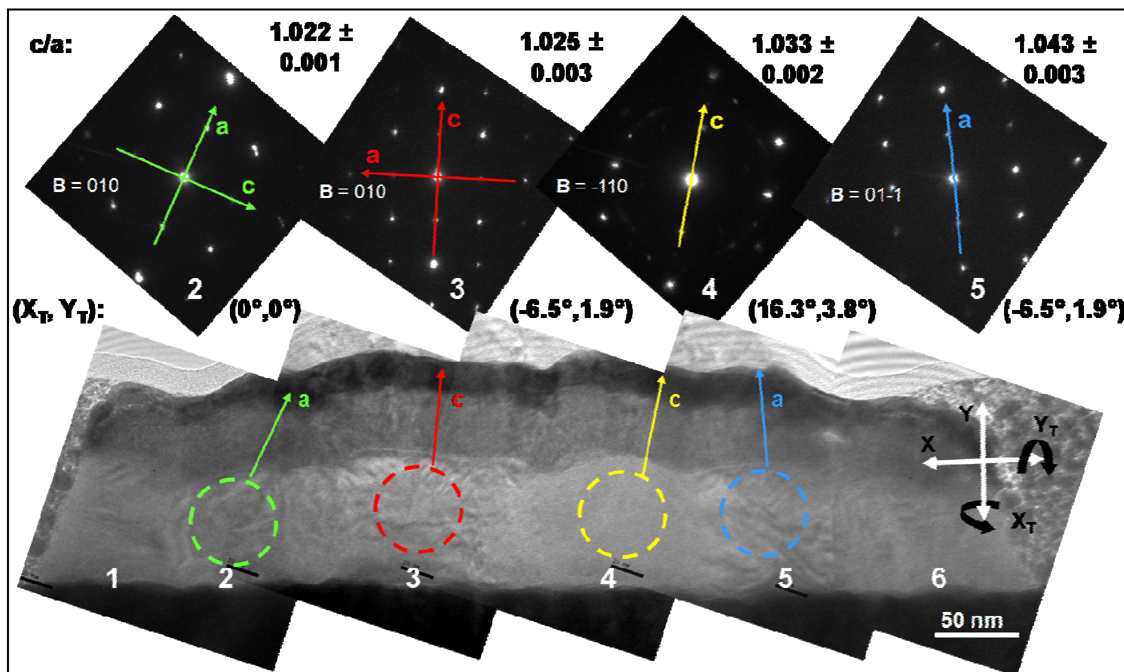


**Figure 5.12.** Four indexed NBD patterns taken from PZT grains in the FRAM capacitor, shown directly below. The capacitor is the same as the one shown in figure 5.11. The orientation for each grain was determined by indexing the NBD patterns. The sample tilts used to obtain the patterns and the measured c/a ratios are also shown.

and 3 could be directly measured from the diffraction pattern. For grains 3 and 4, only one of these axes was present in the pattern due to the orientation of the grain. A value for the axis not present in the pattern was calculated by simple geometry. It should be noted that this was done with the assumption that the a- and b-axes for the grain are equal in length since it is a tetragonal system. This, however, does not take into account any strain that could cause a difference in the a- and b-axes. In addition, the NBD pattern for the grain labeled with a 4 showed additional diffraction spots that are suggestive of diffraction from other grains. Given that the thickness of the cross-sectional TEM window and the average width of a grain are comparable in size, it is possible to have parts of additional grains, in the direction normal to the plane of the cross-sectional TEM window, contributing to the NBD pattern. However, the pattern used to determine the orientation of grain 4 is by far the dominant pattern seen for that particular grain. The NBD results suggest that the orientation of each PZT grain is not random but has a preferred orientation with either the a- or c-axis generally normal to the capacitor electrodes. This preferred orientation is in agreement with previously published x-ray data [55].

## 5.8. HRTEM RESULTS

High resolution TEM (HRTEM) images were obtained from the four PZT grains, shown in figure 5.12, whose crystallographic orientation was determined by NBD. Figure 5.13a shows an HRTEM image of the PZT grain labeled 3 in which 2-directional lattice fringes can be seen. A fast Fourier transform (FFT) was performed on each of the HRTEM images from each of the four grains using Image J. The spatial frequencies were measured in the same manner as described for the NBD patterns. Figure 5.13b,

inset, is the FFT of the HRTEM image in 5.13a. Measurements of the relative distance between spots on the FFT allow for the a- and c-axes to be determined in the same way they were using NBD patterns. Figure 5.13c shows the PZT grain from which the HRTEM image has been taken. The c-axis, which was determined by measuring the FFT, has been drawn on the grain. Comparing the measured c-axis to a line normal to the capacitor electrodes, it can be seen that the c-axis is not perfectly normal to the electrodes but deviates by 3°.

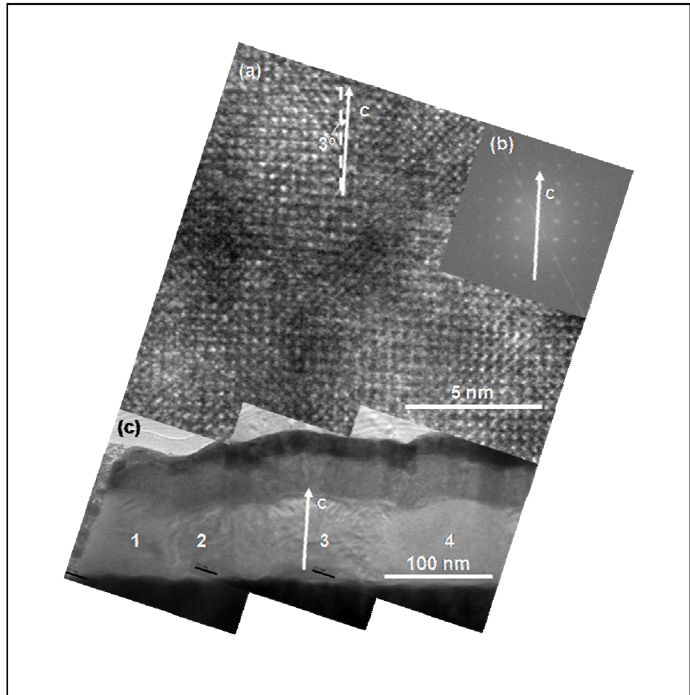


**Figure 5.13.** (a) High-resolution TEM image of PZT grain 3 from the same capacitor exhibiting 2-directional lattice. The c-axis is 3° off of a line normal to the capacitor electrodes. (b) A fast Fourier transform (FFT) of the HRTEM image, showing the c-axis. (c) A lower mag. TEM image showing the location of PZT grain 3 in (a).

Figure 5.14 shows the same capacitor that was characterized by NBD shown in figure 5.12. The same four grains oriented by NBD were oriented using the FFT method. An HRTEM image of each grain was taken and an FFT performed on that image. The FFTs associated with each grain are shown above. The arrows show the a- or c-axis alignment of the grains. The FFT results are in agreement with the NBD results with the exception of grain 5. One possible explanation of this is objective lens astigmatism during the recording of the HRTEM image from which the FFT was taken. This would

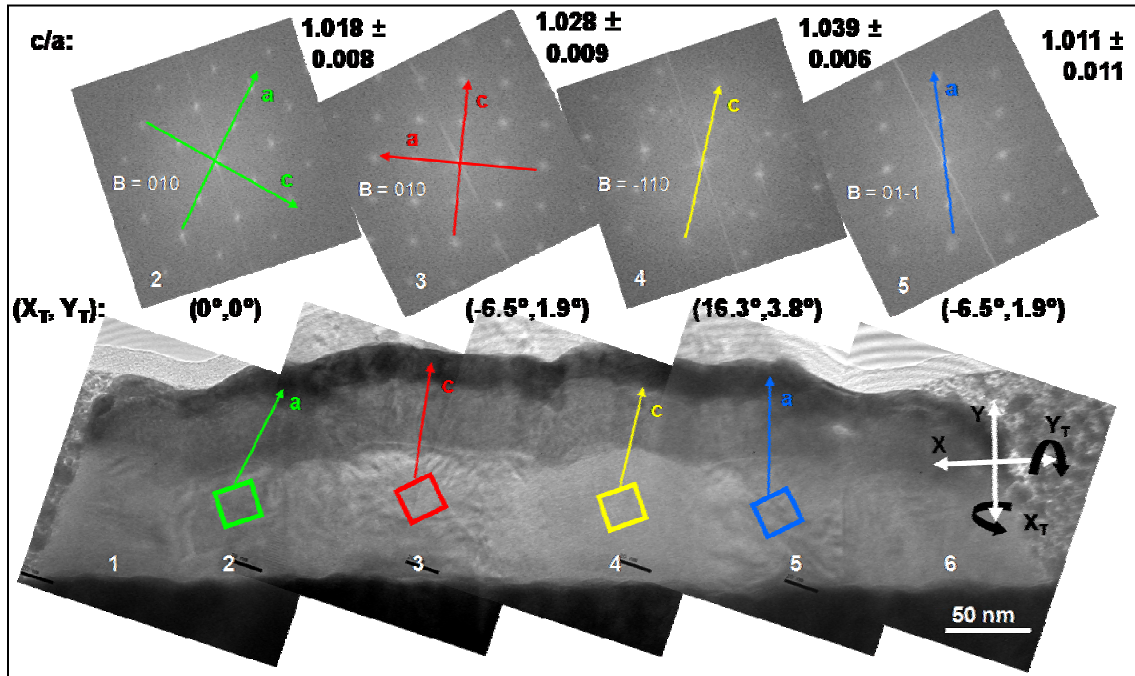


**Figure 5.14.** Four indexed fast Fourier transforms (FFTs) taken from PZT grains in the same FRAM capacitor as before, shown directly below. The orientation of each grain was determined by indexing the FFT. The sample tilts used to obtain the HRTEM images for the FFTs and the measured c/a ratios are also shown.

produce a stretch in the FFT that would cause a disagreement between the FFT and NBD methods.

## 5.9. CONCLUSIONS

FRAM device capacitors from Texas Instruments, Inc. were prepared in cross-section for TEM using the H-bar FIB method. Individual crystalline PZT grains within FRAM device capacitors were successfully characterized using TEM. The average size of individual PZT grains within the capacitors has been determined. The crystallographic orientation of neighboring PZT grains within the same capacitor was determined by measuring relative distances of diffraction spots on NBD patterns taken from each individual grain. The results suggest a preferential orientation of the PZT grains with either the a- or c-axis of the grains generally normal to the FRAM capacitor electrodes.

HRTEM images of the PZT grains show 2-direction lattice fringes and FFT analysis of these images supports the NBD results.

## 5.10. ACKNOWLEDGMENTS

The author would like to thank Dr. K. R. Udayakumar at Texas Instruments, Inc. for supplying the samples and for the many helpful conversations concerning PZT and FRAM, and Dr. Guoda Lian, and Dr. Jayhoon Chung at Texas Instruments, Inc. for all of their assistance with FIB preparation and TEM on the FRAM capacitors.

# CHAPTER 6:

# DUAL-BIPRISM ELECTRON HOLOGRAPHY OF FERROELECTRIC RANDOM ACCESS MEMORY DEVICE CAPACITORS

## 6.1. ABSTRACT

Dual-biprism electron holography has been performed on PZT layers within FRAM device capacitors that have been prepared in cross-section with FIB. Optimization of voltages on the electron biprisms produced a dramatic reduction in Fresnel fringes in the holographs. Independent control of interference fringe spacing with a fixed interference region width was obtained through free lens control of the TEM using Au nanoparticles embedded in $Fe_2O_3$ as a test sample. For the FRAM samples, the best of the PZT holographs display visible interference fringes with a fringe contrast of around 13%. The experiments performed show that the application of dual-biprism electron holography to FRAM capacitors is possible but have raised some practical concerns.

## 6.2. INTRODUCTION

The previous chapter showed that TEM can be successfully used to characterize the grain structure of layers of polycrystalline PZT inside of FRAM device capacitors. In addition, NBD, a TEM-based technique, can be used to obtain the crystallographic orientation of the PZT grains. These techniques however are not capable of exploring the ferroelectric domain structure of the PZT. In PZT, as in all ferroelectrics, domains are formed where volumes of spontaneous dipole moments align themselves in the same direction. Electron holography, which is also TEM-based, is one technique that is capable of exploring the domain structure of PZT. Electron holography is extremely sensitive to electric fields in and around TEM samples and thus sensitive to the electric polarization of PZT domains. Electron holography using a single biprism has been used before to investigate PZT [56] including PZT inside of an FRAM device capacitor [57]. Information about the size, number, and location of domains within the PZT layer of an FRAM capacitor is very useful in understanding FRAM device performance. In addition, using electron holography to obtain PZT domain structure information in FRAM device capacitors and combining it with grain structure and crystallographic orientation information obtained by TEM and NBD from the same capacitors would provide a good overall picture of the PZT layer in the FRAM capacitor. Such information could be beneficial in improving future FRAM devices. To the author's knowledge no such combined study has been done.

In this chapter, a brief background on single-biprism electron holography will be given followed by a discussion of dual-biprism electron holography. Initial work on optimization of the dual-biprism electron holography parameters will be presented. In

addition, practical considerations of dual-biprism electron holography of PZT in FRAM device capacitors will be discussed. The results of electron holography of PZT in FRAM device capacitors will be given. The holographs show visible electron interference fringes with the best holographs showing a fringe contrast of only around 13 %.

### 6.3. SINGLE-BIPRISM ELECTRON HOLOGRAPHY

The concept of electron holography predates optical holography [58]. However, the invention of a coherent optical source, *i.e.* the laser, allowed the realization of optical holography before electron holography. A coherent source of electrons finally became available with the advent of the field-emission electron gun which made electron holography possible. A schematic of the typical microscope arrangement for off-axis electron holography is shown in figure 6.1 [59]. For off-axis electron holography, part of the incident electron wave passes through the specimen (object wave) and the other part passes unimpeded through the vacuum next to the specimen (reference wave). These two waves are then brought together to interfere with one another by an electron biprism which consists of a conductive Au-coated quartz fiber to which a voltage is applied. In the resulting interference pattern, shifts in interference fringes indicate phase changes in the object wave caused by electric and magnetic fields within the specimen. This sensitivity to

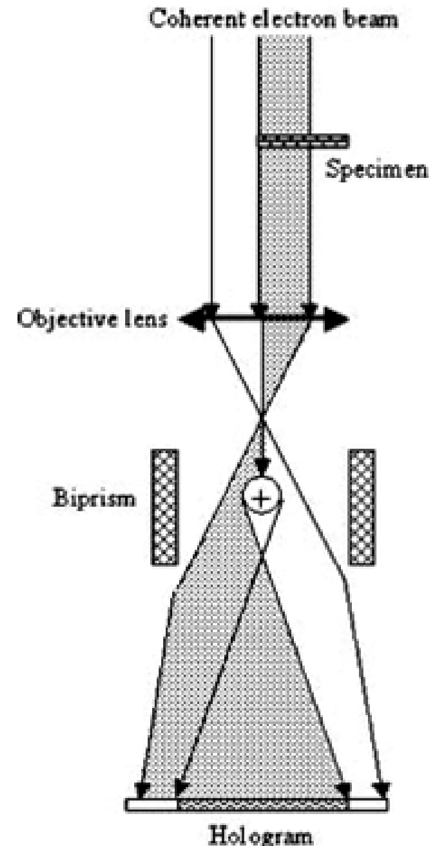


**Figure 6.1.** Microscope arrangement for single biprism electron holography.

electric and magnetic fields within the specimen is what makes electron holography a uniquely beneficial TEM technique.

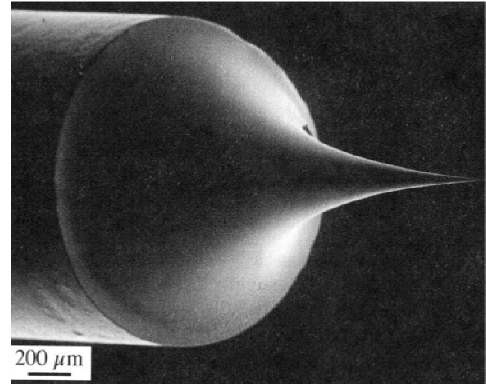


**Figure 6.2.** <310> oriented etched tungsten tip used for a field-emission TEM which is key to electron holography.

As has been mentioned, a source of coherent electrons is crucial to electron holography. This criterion was finally met with the invention of the field-emission gun (FEG). An example of the tip of an FEG is shown in figure 6.2 [60]. In an FEG, a <310> oriented tungsten tip with a tip radius of curvature less than 100 nm is subjected to a high applied voltage. This high voltage results in a high electric field at the tip such that electrons are able to tunnel out of the tip due to the lowered work function barrier caused by the electric field [60]. The FEG produces electrons that are temporally coherent (longitudinal coherence in the direction of propagation) and spatially coherent (transverse coherence of the wave front perpendicular to propagation direction). The former depends on the energy spread of the electrons and the latter depends on the source size [61]. These coherent electrons are then accelerated down the TEM column by the accelerating voltage. The electrons then encounter the first set of TEM lenses, the condenser lenses, which control the illumination of the specimen with electrons.

The specimen to be studied by electron holography is placed such that only half of the specimen occupies the viewing area. The other half of the viewing area is a vacuum. The electron wave that passes through the specimen is referred to as the object (perturbed) wave and can be represented as a plane wave of the form:

$$\psi_o = a(x,y)e^{i\phi(x,y)} \tag{6.1}$$

It is important to note that both the phase and the amplitude are dependent on the coordinates x and y, which are in the plane of the specimen. The part of the electron wave that passes through the vacuum is called the reference (unperturbed) wave and can be considered as a plane wave with an amplitude of unity and a phase of 0 given by:

$$\psi_r = 1 \tag{6.2}$$

Interactions of the coherent electrons with electric and magnetic fields in the specimen result in a phase shift of the object wave whereas the reference wave experiences no phase shift as it passes through the vacuum. The phase shift caused by these fields is given by:

$$\Delta\phi(x,y) = \frac{\pi}{\lambda E}\int V(x,y,z)dz - \frac{e}{\hbar}\iint \vec{B}\cdot d\vec{S} \tag{6.3}$$

where $E$ is the electron energy, $\lambda$ is the electron wavelength, $V$ is the electric scalar potential, and $\vec{B}$ is the magnetic field [62]. The integral on the left is the electric contribution to the phase shift and is integrated in the direction of the incident electron beam. The second integral is the magnetic contribution and is to be integrated over a surface enclosed by both the object and reference beams.

After passing through the objective lens below the sample, which may be lightly excited or even turned off, the reference and object waves encounter the electron biprism. The electron biprism consist of a very thin, typically $< 1$ μm in diameter, quartz fiber that has been coated with gold [61, 63] and sits between two grounded electrodes. A positive bias is applied to the biprism which results in the object and reference waves being made to interfere with one another, forming an interference pattern. This interference pattern is

magnified and projected onto a recording device, typically a CCD, by the intermediate and projector lens systems.

The intensity of the recorded holograph is given by:

$$I = |\psi_r + \psi_o|^2 = |\psi_r|^2 + |\psi_o|^2 + \psi_r^* \psi_o + \psi_o^* \psi_r \qquad (6.4)$$

$$I = \left|1 + a(x,y)e^{i\phi(x,y)}\right|^2 = 1 + a(x,y)^2 + a(x,y)e^{i\phi(x,y)} + a(x,y)e^{-i\phi(x,y)} \qquad (6.5)$$

$$I = 1 + a(x,y)^2 + 2a(x,y)\cos[\phi(x,y)] \qquad (6.6)$$

The first two terms in equation 6.6 represent a superposition of the intensity due to the amplitudes of the reference and object waves respectively. The third term, which is cosinusoidal, represents the interference pattern. Shifts in the fringes of the interference

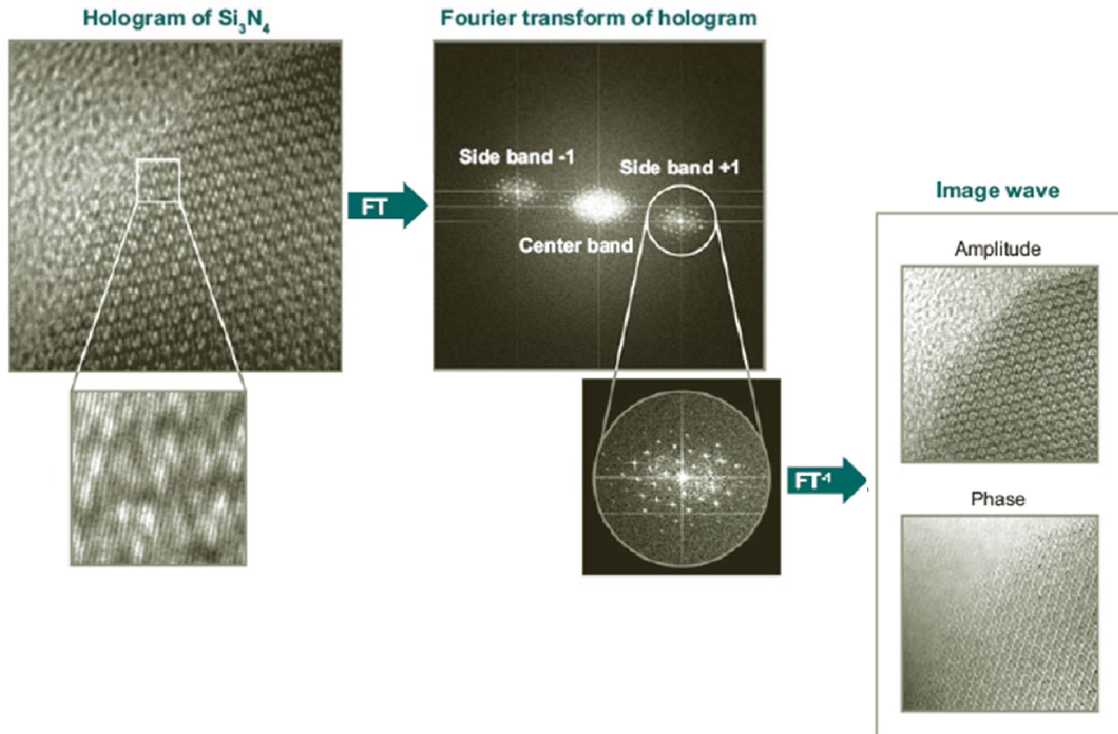


**Figure 6.3.** Reconstruction process for electron holography. The holograph is Fourier transformed producing side bands that represent the Fourier transform of the object wave and its conjugate. One of the sidebands is selected and an inverse Fourier transform is performed. The amplitude and phase can then be extracted from the reconstructed object wave.

pattern are the result of phase shifts of the object wave.

To obtain phase information, the holograph is reconstructed as shown in figure 6.3 [56]. First a Fourier transform of the holograph is performed. The resulting Fourier spectrum shows three bands, a central band and two sidebands referred, to as the +1 and -1 sidebands. The central band is a result the conventional image which corresponds to the first two terms in equation 6.5 and the +1 and -1 side bands correspond to terms 3 and 4. The +1 side band is the Fourier transform of the complete object wave while the -1 side band is its conjugate. The +1 side band is selected out, and an inverse Fourier transform is performed yielding the complete object wave. From this complete object wave, the amplitude and phase information from the object wave can be extracted.

## 6.4. DUAL-BIPRISM ELECTRON HOLOGRAPHY

One emerging technique for improved electron holography is dual-biprism electron holography [64-67]. A schematic of the typical microscope arrangement for dual-biprism electron holography is shown in figure 6.4 [65]. The principle of dual-biprism electron holography is the same except for the addition of another biprism. In dual-biprism holography, one biprism (the upper biprism or BP1) is inserted at the image plane of the objective lens between the objective lens and magnifying lens. The other biprism (the

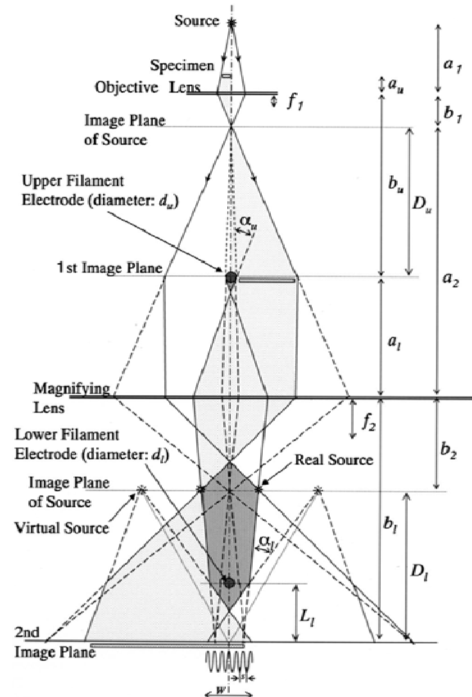


**Figure 6.4.** Detailed microscope arrangement for dual-biprism electron holography.

lower biprism or BP2) is inserted in between the cross-over point and image plane of the magnifying lens. The function of the dual-biprism arrangement, as an improvement over the single-biprism arrangement, is that it allows independent control over the interference fringe spacing (spatial resolution of the reconstructed holograph) and width of the interference region (field of view of the holograph). In addition, the use of a second biprism eliminates Fresnel fringes in the interference region that are due to Fresnel diffraction by the biprisms as observed in single biprism holography [67, 68]. The equations governing the fringe spacing $s_{obj}$ and interference region width $W_{obj}$ are given by [64]:

$$s_{obj} = \frac{1}{M_l}\frac{1}{M_u}\frac{a_2 D_l \lambda}{2\left[\alpha_l a_2 \left(D_l - L_l\right) + \alpha_u b_2 D_u\right]} \tag{6.7}$$

$$W_{obj} = \frac{1}{M_l}\frac{1}{M_u} 2\alpha_l L_l - \frac{1}{M_u} d_u \tag{6.8}$$

Where $\lambda$ is the electron wavelength, $M_u$ and $M_l$ are the magnification factors for the upper (objective) and lower (magnifying) lenses shown in figure 6.4, and $\alpha_u$ and $\alpha_l$ are the deflection angles produced by the upper and lower biprism respectively. All other terms in equations 6.7 and 6.8 are shown on figure 6.4. Here it is important to note that $s_{obj}$ and $W_{obj}$ are only truly independent if $D_l$ - $L_l$ = 0, in which case $s_{obj}$ and $W_{obj}$ are controlled by the deflection angles of the upper and lower biprisms which are controlled by the voltages applied to the upper and lower biprisms respectively. A microscope arrangement with $D_l$ - $L_l$ = 0 was constructed on a 1 MV TEM as described by K. Harada *et al.* [64]. It is noted by the authors, however, that the $D_l$ - $L_l$ = 0 condition may not be possible in a conventional TEM. For most conventional TEMs (200 kV or 300 kV), the condition $D_l > L_l = 0$ is the most practical. While this arrangement does not give

complete independent control over the fringe spacing and interference region width, it is advantageous in that once and interference width is chosen by selecting the voltage on the lower biprism, which determines $\alpha_l$, the voltage of the upper biprism can be used to adjust $\alpha_u$ which in turn controls the fringe spacing of the holograph [67].

## 6.5. RESULTS AND DISCUSSION

Dual-biprism electron holography was performed on a 300 kV Hitachi HF-3300 field emission TEM at Oak Ridge National Laboratory. This instrument possesses a cold field emitter to provide a source of coherent electrons which is crucial for electron holography. The cold field emitter is the best choice for electron holography because of its small source size and small energy spread of the emitted electrons. Both the upper and lower biprisms on the HF-3300 were first calibrated by measuring biprism voltage versus fringe spacing at 1 Mx magnification. This was done by increasing the voltage in a step-wise manner on each biprism separately and recording the interference pattern on a 2048 x 2048 pixel CCD using Gatan Digital Micrograph software. The distance between the fringes was measured by performing an FFT on the interference pattern using the software. The spatial frequency

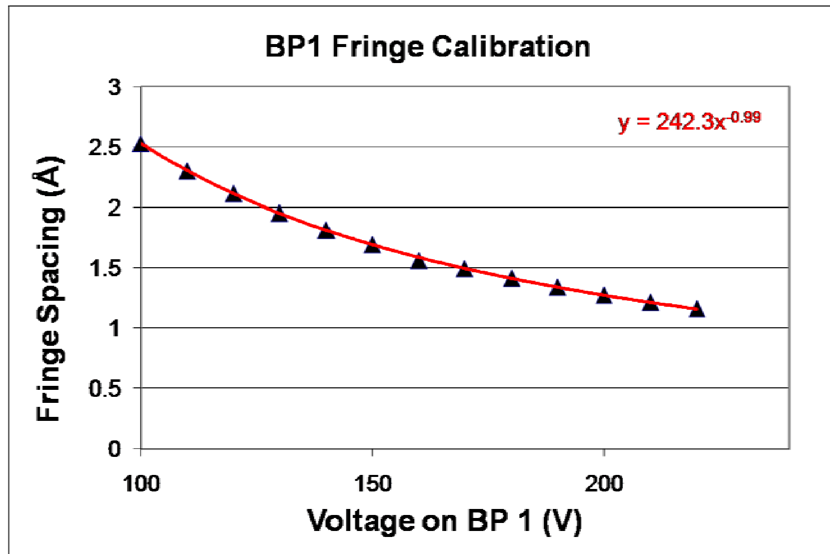


**Figure 6.5.** Plot of electron hologram fringe spacing vs. applied voltage to the upper biprism (BP1). The fringe spacing is proportional to 1/V where V is the voltage on the biprism.

of the fringes was then measured and the fringe spacing calculated. The results were plotted with the applied voltage on the biprism. The fringe spacing versus biprism voltage for the upper biprism (BP1) is shown in figure 6.5. It can be seen that the fringe spacing is inversely proportional to the biprism voltage.

In doing either single-biprism or dual-biprism electron holography, it is important to align the biprisms properly. Figure 6.6 shows a bright-field TEM image of a bank of FRAM capacitors with the shadow of one of the biprisms cutting diagonally across the image. To obtain the best electron holography results, the biprisms were aligned such that the length of the biprisms is parallel to the sample/vacuum interface. This is necessary to split the incoming electron wave into an object and reference wave to produce the interference pattern. Figure 6.7a shows both electron biprisms aligned parallel to each other with the smaller biprism being the upper biprism and the larger biprism being the lower biprism. As can be seen, both biprisms have contamination on them. Figure 6.7b shows the interference region with an appropriate applied bias to both

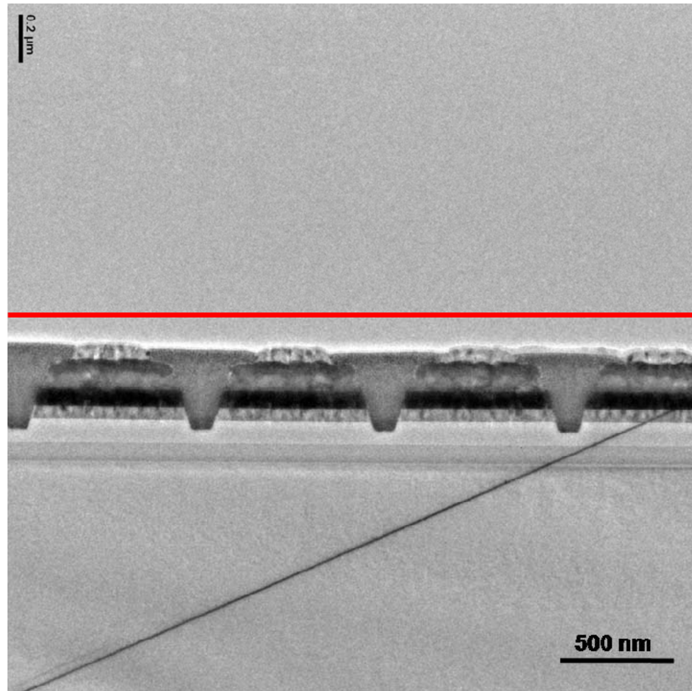


**Figure 6.6.** Bright-field TEM image of a bank of FRAM capacitors. The shadow of one of the electron biprisms can be seen going diagonally across the image during alignment of the biprisms. Ideally, the biprism needs to be in a position such that it is aligned parallel to the sample/vacuum interface as indicated by the red line.

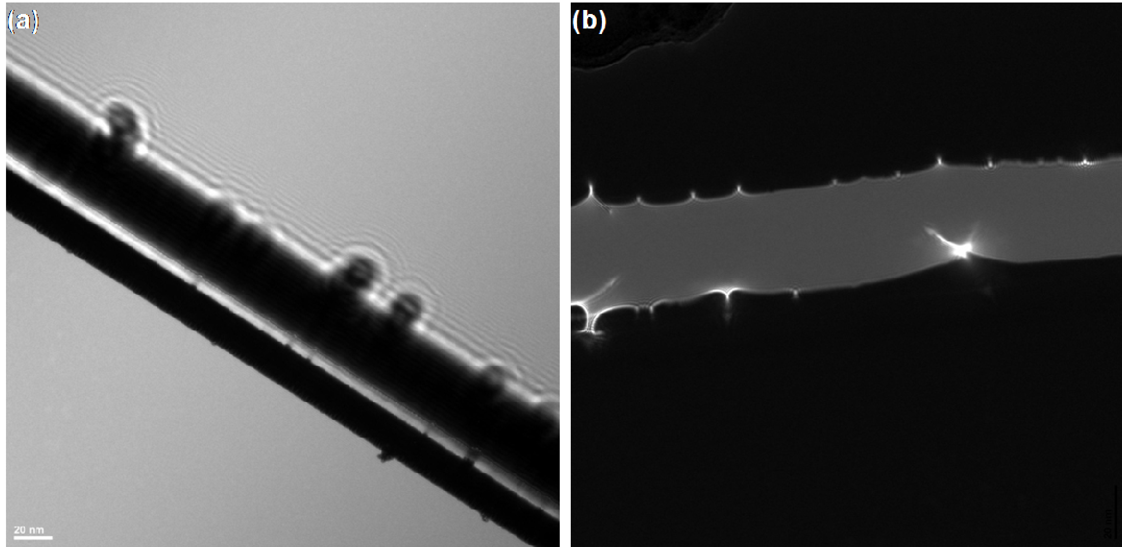


**Figure 6.7.** (a) Bright-field TEM image of both biprisms aligned for electron holography. Contamination on both biprisms can be seen. (b) Bright-field TEM image of the interference region (bright area) produced with both biprisms properly biased. Note the distortions in the interference region due to charging of the contamination particles.

biprisms. Adverse effects from charging can be seen all along the interference region. Regions that had a minimal amount of contamination were chosen to perform the electron holography to minimize the effect on the holographs.

As has been mentioned, reduction of Fresnel fringes in electron holographs is one of the advantages of using two biprisms. The presence of Fresnel fringes in the electron holograph is undesirable in that they can make observation of weak electric and magnetic fields in a small region difficult. Figure 6.8a shows the interference region produced by the lower biprism with a +70 V applied bias. The finer fringes are the interference fringes while the coarser fringes near the edge of the interference region are the Fresnel fringes, resulting from Fresnel diffraction of electrons from the biprism. Figure 6.8b shows the interference region using both biprisms with a +40 V bias on the upper biprism and a +44 V bias on the lower biprism. The Fresnel fringes are not completely absent but are dramatically reduced compared to the interference region produced by the single

biprism. The reduction in Fresnel fringes by using the dual-biprism arrangement is the result of a shadowing effect on the lower biprism due to the presence of the upper biprism [64].

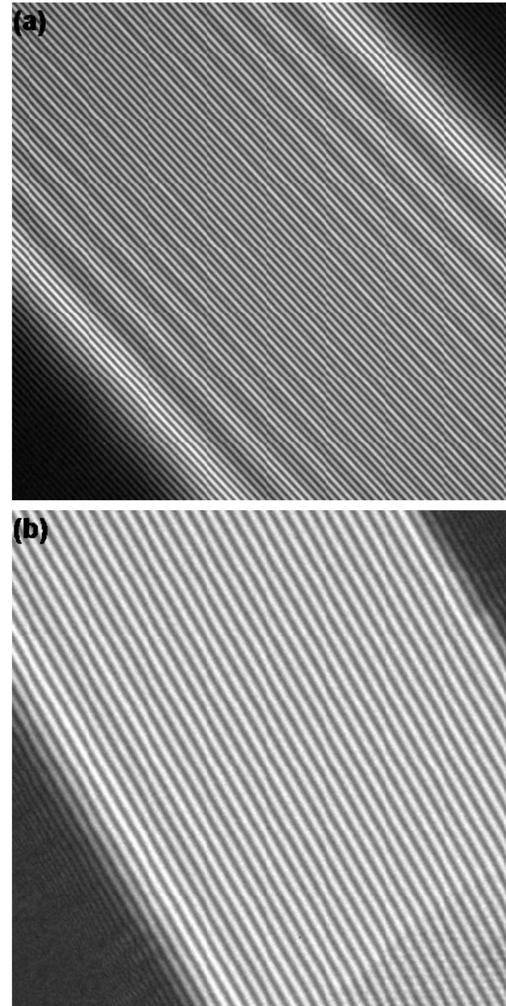


**Figure 6.8.** (a) Electron interference pattern using a single biprism. The finer fringes are the interference fringes and the coarser fringes near the edges of the interference region are Fresnel fringes. (b) Electron interference pattern using two biprisms with interference fringes. The Fresnel fringes are not completely absent but are dramatically reduced.

To explore what microscope settings were optimal for dual-biprism electron holography on the microscope, Au nanoparticles embedded in $Fe_2O_3$ were investigated. This sample was chosen as a test sample because the particles had previously been confirmed to be stable in the microscope (no drift) and it allowed the settings of the microscope to be optimized over a long period of time without having to expose the FRAM sample to long periods of irradiation from the electron beam. Figure 6.9 shows an electron holograph of a single Au particle embedded in $Fe_2O_3$. Interference fringes are very prominent within the interference region. Inset in the image is an enlarged image of the Au nanoparticle showing lattice fringes. Subtle shifts in the interference fringes can be seen as the fringes cross the particle due to the fact that

the object wave is now exiting not only the $Fe_2O_3$ matrix but also the Au nanoparticle causing a shift in phase.

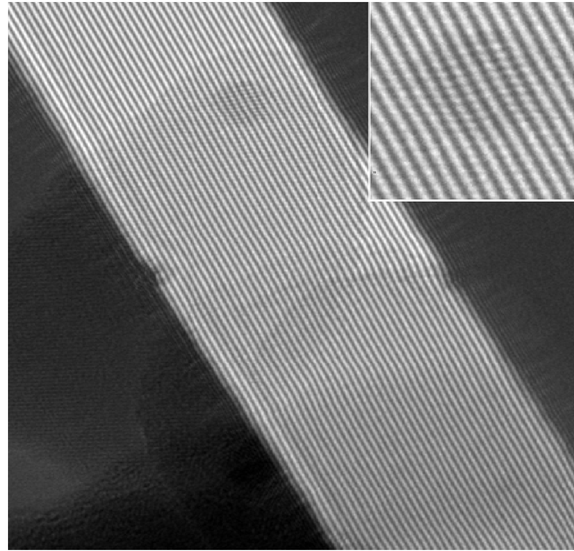

**Figure 6.9.** Dual-biprism electron holograph of an Au particle imbedded in $Fe_2O_3$. Inset is an enlarged image of the Au particle showing subtle shifts in the interference fringes as they cross the particle. The horizontal fringes seen in the particle are Au lattice fringes.

The investigation of the Au nanoparticles in $Fe_2O_3$ revealed that the best possible holography conditions could only be obtained using free lens control; where the current values of each lens are exactly specified by the operator. The optimal values are given in table 6.1. By using these values, somewhat independent control over the fringe spacing and interference region width was achieved with the upper biprism voltage controlling the fringe spacing and the lower biprism setting the interference region width. It should be noted at this point that by using free lens control the actual magnification of the image in the microscope was no longer in sync with the magnification displayed by the microscope control software or the image acquisition software. Care must therefore be taken when interpreting images where the size of features in the image is important. Reference

| Lens | Current (A) |
|---|---|
| Objective | 14.968 |
| Intermediate 1 | 3.243 |
| Intermediate 2 | 6.700 |
| Projector 1 | 5.490 |
| Projector 2 | 4.986 |

**Table 6.1.** Optimal lens current settings for dual-biprism electron holography on the Hitachi HF-3300

images should be taken of the features in the normal operating mode of the microscope such that the size of features is known.

After the optimal conditions were found for making electron holographs using the dual-biprism system, PZT within FRAM device capacitors was investigated using these holographic conditions. At this point, a problem became apparent in performing dual-biprism electron holography of FRAM capacitors using the Hitachi HF-3300. It was found that it was not possible to create an interference region wide enough to encompass both the PZT layer for the object wave and vacuum for the reference wave. This is because as prepared, the PZT in the cross-sectional FRAM samples is still underneath ~ 100 nm of top electrode material of the capacitor. The largest interference regions produced that contained visible interference fringes were on the order of ~40 nm. This result is a bit surprising given that electron holographs using a dual-biprism set-up have been produced with interference region widths on the order of 1 μm [66]. It should be noted however that those holographs were taken on a 1 MV TEM that contains more lenses than the HF-3330 and thus, this could result in larger interference region widths than can be obtained in the HF-3300. Since the interference region would not encompass both vacuum and the PZT layer, a cross-sectional FRAM sample that was inadvertently over-milled during FIB preparation was chosen for investigation. An SEM image of the sample is shown in figure 6.10a. It can be seen in the SEM image that the top structures of the capacitors enclosed by the dashed red oval have been all or partially removed by FIB milling. This allowed electron holography to be performed with areas of PZT next to vacuum. Figure 6.10b shows one of the electron holographs taken in one such area with an enlarged image of the interference fringes inset. The fringes are visible with a fringe

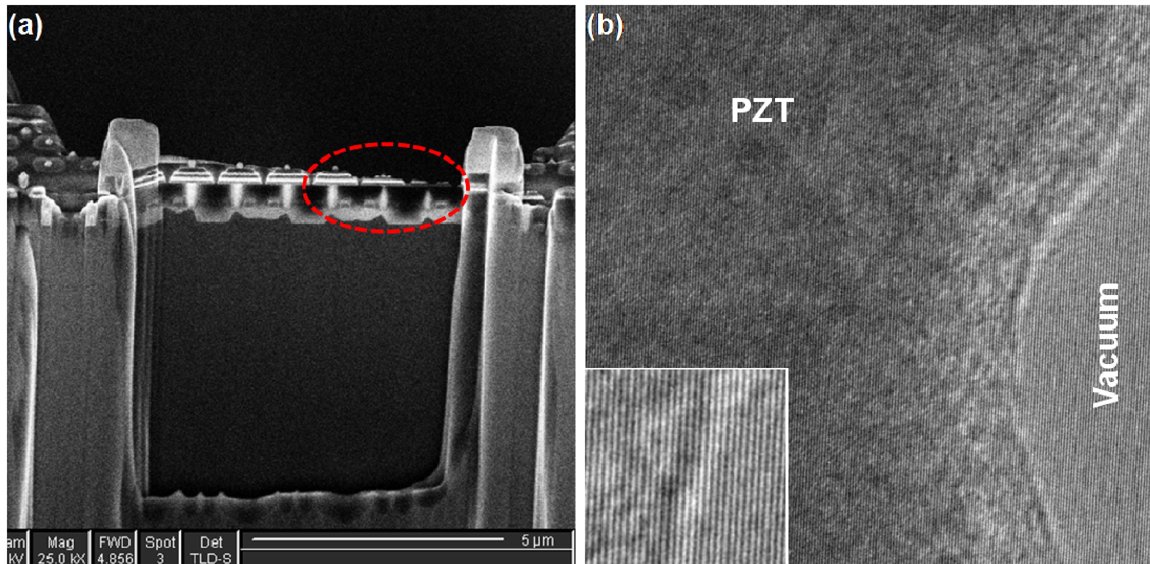


**Figure 6.10.** (a) SEM image of a row of FRAM capacitors prepared in cross section by FIB. Some of the capacitors have had their top layers removed by the FIB. (b) Dual-biprism electron holograph of PZT from one of the FRAM capacitor with higher magnification image of the interference fringes inset. Part of the capacitor was removed by the FIB producing a PZT /vacuum interface.

contrast of about 13 %. The fringe contrast value is low (25-30% is considered good) and is thought to be due to the contaminated biprisms. It should be noted that the higher the fringe contrast, the better the signal-to-noise ratio is in subsequent amplitude and phase images derived from the reconstruction of the holograph. Although electron holographs can be obtained with FRAM samples purposely prepared in a similar manner with the top part of the capacitor milled away to expose the PZT, this situation is not ideal. As was discussed in chapter 5, PZT can be easily amorphized by the focused ion beam during ion beam milling. HRTEM of the PZT from the over-milled capacitors studied here showed the PZT to be only partially crystalline (*i.e.* small areas of crystalline material mixed with amorphous areas) or completely amorphous.

## 6.6. CONCLUSIONS

Dual-biprism electron holography has been performed on PZT layers within FRAM device capacitors. Prior optimization of microscope parameters allowed for independent control of fringe spacing for a fixed interference width. A reduction in Fresnel fringes in the electron holographs was also produced. It was discovered that the interference region created by the dual-biprisms is not large enough to reach the PZT layer underneath the top electrode structure of the FRAM capacitors and to keep the vacuum region in part of the image for the reference wave. Holographs of PZT from an over-milled cross-sectional TEM sample of FRAM capacitors were obtained with visible fringes, but low fringe contrast. In the future, cross-sectional FRAM samples with the top electrode structure carefully removed will need to be prepared in order to obtain the best electron holographs for reconstruction and subsequently characterize the domain structure within the PZT layer.

## 6.6. ACKNOWLEDGMENTS

The author would like to thank Dr. Larry Allard at Oak Ridge National Laboratory for his help with the dual-biprism electron holography.

# CHAPTER 7:

# CHARACTERIZATION OF A BARE PZT LAYER ON AN FRAM CAPACITOR ELECTRODE

## 7.1. ABSTRACT

Bare layers of PZT from short flow FRAM wafers have been characterized. The bare PZT layer is a polycrystalline film deposited on the bottom electrodes of FRAM capacitors. After deposition of the PZT, the fabrication was stopped, leaving the PZT exposed. SEM and AFM results show individual PZT grains in the layer. X-ray diffraction and texture results indicate that the grains in the film are not randomly oriented but have a preference for either the a- or c-axis oriented normal to the sample surface. Preliminary piezoresponse force microscopy (PFM) results show domains in the PZT and a variation in piezoresponse across the PZT. In addition, preliminary results of band excitation piezoresponse spectroscopy (BEPS) show clear switching behavior in the PZT film.

## 7.2. INTRODUCTION

Many nanostructure and materials characterization techniques require unimpeded access to the structure or material in question. For fully fabricated FRAM device

capacitors, as with other devices, some characterization methods are difficult to perform in that the PZT layer is buried under additional layers and structures. In addition, the fabrication of these additional layers and structures may alter the PZT film itself. Therefore it is advantageous to study PZT layers as deposited, without the additional processing associated with fabricating FRAM. For PZT layers in FRAM, it would be of great benefit to characterize both the grain and domain structure of the PZT in plan view, using techniques such as AFM, XRD, and PFM. In addition, data from such techniques could be compared to data from FRAM devices that have been processed beyond the PZT deposition and studied in cross-section using techniques discussed in chapters 5 and 6.

In this chapter, characterization results from a bare PZT film, referred to as a blanket PZT layer, from an FRAM device wafer without the top capacitor electrode material are presented. SEM and AFM results show individual grains of PZT with lateral grain sizes similar to those seen in cross-sectional FRAM device capacitors. In addition, the results show a depression in the PZT layer that is thought to be associated with the tungsten contact underneath the bottom electrode. XRD and texture results show that grains in the film are not randomly oriented but have a preference for either the a- or c-axis oriented normal to the sample surface. Initial PFM results show ferroelectric domains in the PZT film and a variation of piezoresponse across the PZT. Initial band excitation piezoresponse spectroscopy shows clear switching behavior in the PZT.

### 7.3. SEM AND AFM

SEM was performed on the blanket PZT layer sample using a JEOL JSM-880 SEM at the University of Oklahoma. Figure 7.1a shows a plan view SEM image of the blanket PZT layer in which individual grains of PZT can be seen. Lateral dimensions of the

grains range from as small as 40 nm to as large as 140 nm. It can be seen from the image that many of the grains posses fairly straight edges at the grain boundaries. In the center of the image a small depression can be seen. This depression is thought to be associated with the underlying electrode structure as seen in the cross-sectional SEM image.

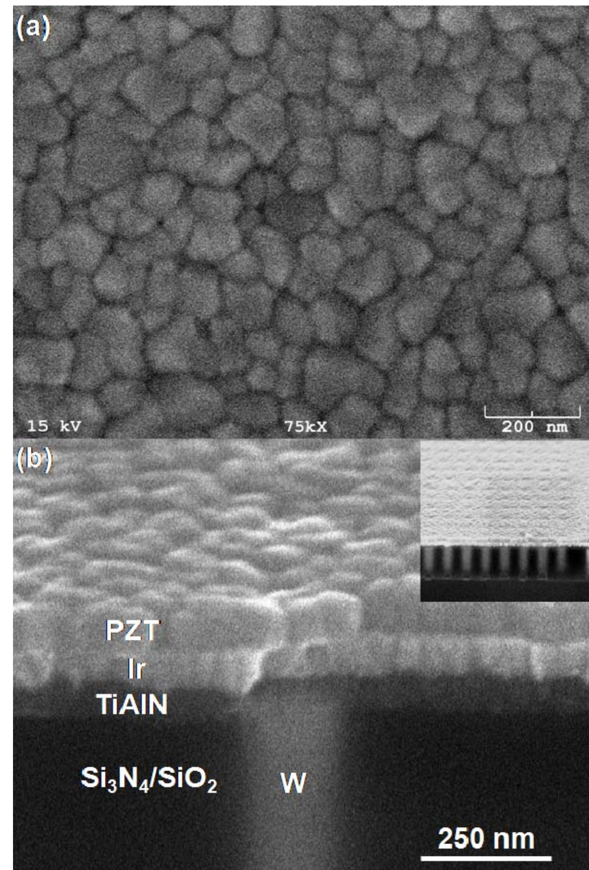


**Figure 7.1.** (a) Plan view SEM image of the blanket PZT layer. (b) Cross-sectional SEM image of the blanket PZT layer with layers labeled. The sample is at a 70° tilt to the electron beam. Inset is a lower magnification x-sectional image showing depressions in the PZT due to the W contacts.

Figure 7.1b shows a cross-sectional image of the blanket PZT layer sample. The polycrystalline PZT layer can be seen on top with the rest of the bottom capacitor electrode structure below. Also in the image, one of the tungsten contacts can be seen attached to the bottom electrode. Although it is difficult to see, there is a small depression in the PZT layer, similar in size as the one seen in figure 7.1a, occurring above the tungsten contact. This is better illustrated in the lower magnification cross-sectional image inset. The depressions occur at regular intervals in-line with the tungsten contacts seen in cross-section, suggesting the depressions are a result of the presence of the tungsten contacts. Measurements on the cross-section SEM image show that the thickness of the PZT layer

is approximately 90 nm. This is thicker than the films in the FRAM capacitors discussed in chapter 5.

In addition to SEM imaging, AFM was performed on the blanket PZT layer using a Topometrix AFM in non-contact mode. The tip used was a MikroMasch NSC35 ultrasharp tip with a radius of curvature less than 10 nm. Figure 7.2 shows a 2 μm by 2 μm scan with a 5 μm by 5 μm scan inset. As seen from the image, the lateral grain sizes are similar to those seen in the SEM. The depressions associated with the tungsten contacts are very prominent in the AFM image. From the AFM image, it was determined that the depth of the depressions were in the 20-30 nm range.

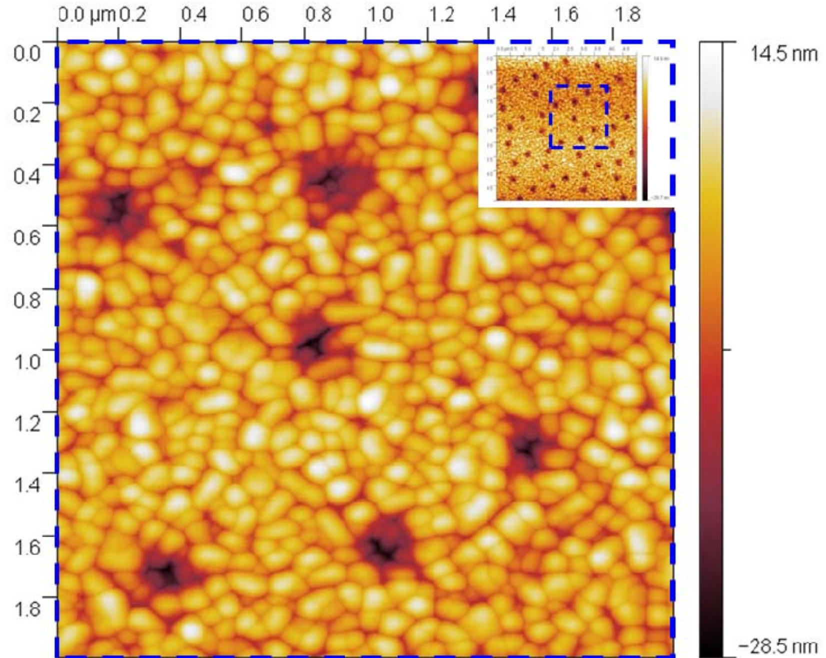


**Figure 7.2.** 2 μm x 2 μm AFM image of the blanket PZT layer with 5 μm x 5 μm scan inset.

## 7.4. XRD

In order to explore the crystallinity of the blanket PZT layer, x-ray diffraction (XRD) was performed on the sample. XRD works on the principle of Bragg diffraction of x-rays from crystal planes within the sample. Initial XRD was performed at the University of Oklahoma using a powder x-ray diffractometer. The diffractometer used the Bragg-Brentano geometry, illustrated in figure 7.3. In such an arrangement, the

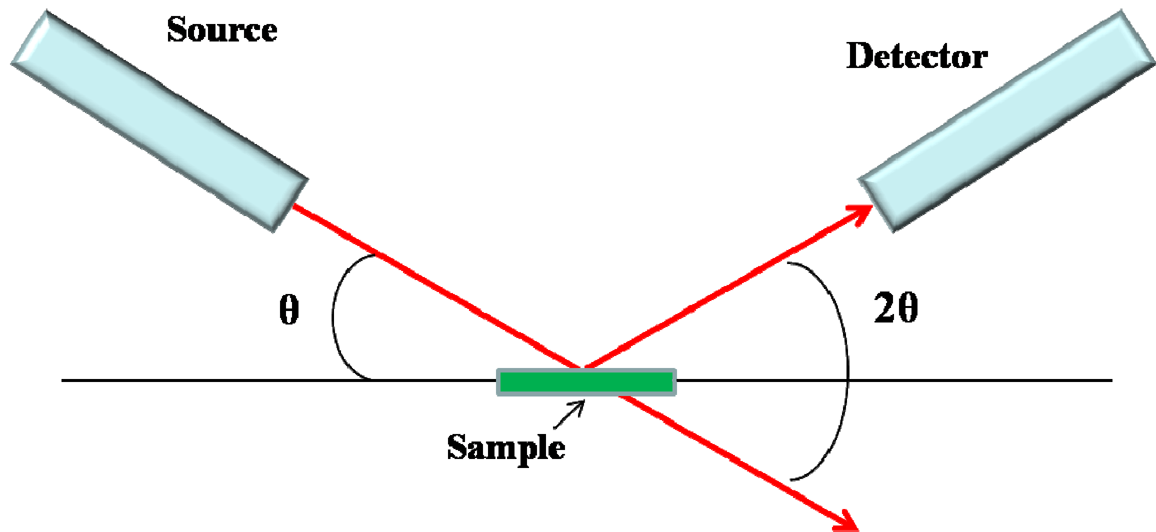


**Figure 7.3**. Bragg-Brentano XRD powder arrangement.

sample remains stationary and the x-ray source rotates in the positive +θ direction; while the detector simultaneously rotates in the -θ direction.

Figure 7.4 shows the XRD results from the blanket PZT layer in x-ray counts per second vs. 2θ. The sample was tilted at ~1° towards the detector to eliminate the Si (200) peak from the substrate that was observed. The blue line represents the XRD data from the blanket PZT sample. The red squares represent the positions and relative intensities for a PZT (25/75) powder sample. These values had to be estimated since the International Centre for Diffraction Data (ICDD) database did not contain the values for PZT (25/75). To estimate these points, the lattice parameters for PZT (25/75) were used to calculate the d-spacing for several of the crystal planes of PZT (25/75). The 2θ positions for the peaks were the calculated using the Bragg equation with $\lambda = 1.540562$ Å, which is the $K_{\alpha 1}$ x-ray line for copper. The calculated 2θ values for each plane were then paired with relative intensity values for the same planes in PZT (44/56) which was in the ICDD database. These values were then plotted in the figure and offset from the x-axis by 200 CPS.

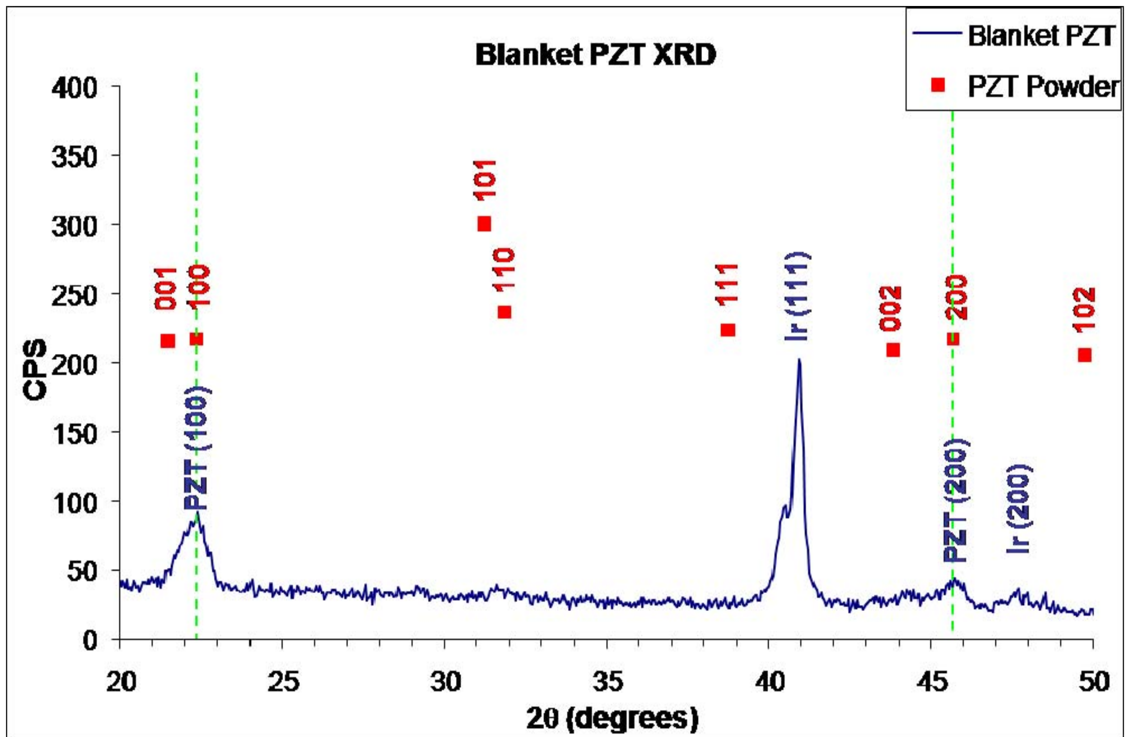


**Figure 7.4.** XRD plot of blanket PZT pattern with offset calculated powder XRD positions and intensities.

At this point it should be made clear as to what is meant by powder sample. A powder sample is considered one where the orientations of the crystallites are completely random. The values plotted as the red squares represent the peaks and relative intensities that should be seen in the orientations of the grains in the blanket PZT layer were completely random. From the XRD data, only the (100) and (200) peaks for blanket PZT sample can be readily seen, with a very small (110) peak present. It should be noted that the separation of the (100) and (001) peaks is not seen here nor has it been seen in other previously reported x-ray data on similar PZT layers [55]. It can be seen that the (100) peak is quite broad. This broadening is possibly due to a combination of small grain size and non-uniform strain of the grains [69]. The fact that only a few peaks are present in the sample suggests that the grains in the blanket PZT film are not randomly oriented but

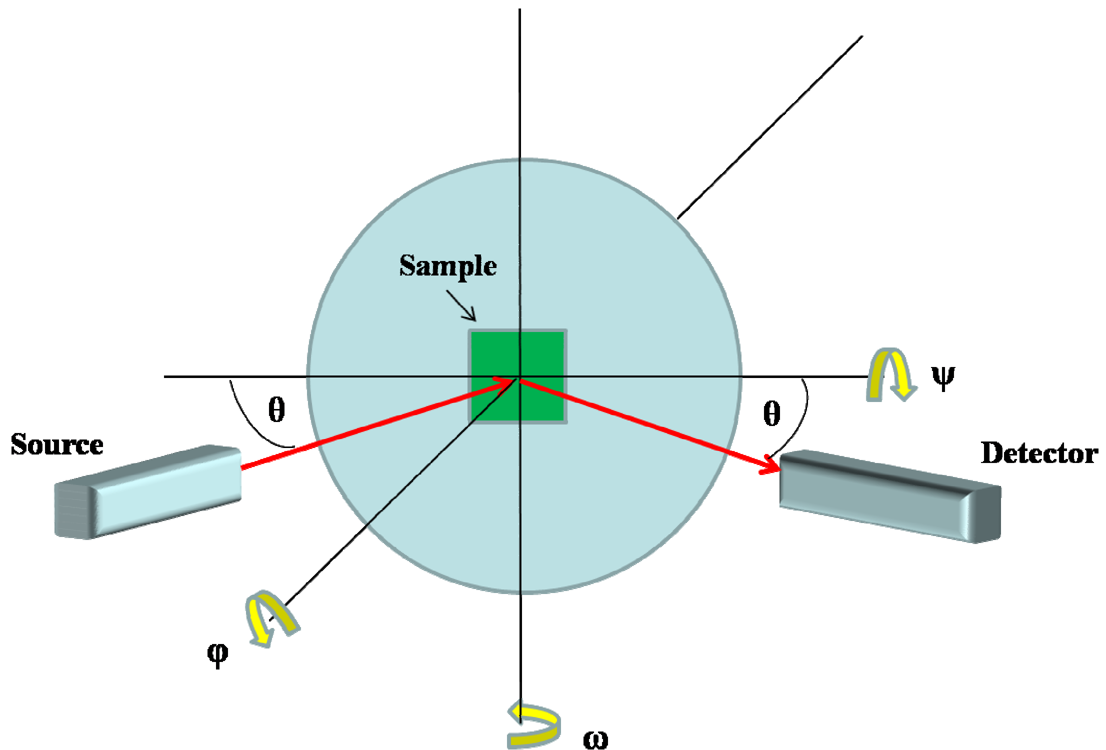


**Figure 7.5.** Four-circle diffractometer arrangement.

have a texture. This conclusion is supported by the NBD results from PZT grains in the short flow FRAM capacitors presented in chapter 5.

To further explore the texture orientation of the blanket PZT sample, XRD texture scans were performed at Oak Ridge National Laboratory using a four-circle diffractometer, as depicted schematically in figure 7.5. For texture scans, a specific crystal plane is chosen and the x-ray source and the detector are set up such that the 2θ value for Bragg diffraction from the plane is selected. The sample is then rotated azimuthally in φ and tilted in ψ. Data is then collected at a series of (ψ, φ) points. The data for the selected plane can be plotted as a pole figure with φ as the azimuthal angle and ψ as the radius. Pole figures for three planes, (100), (110), and (210) are shown in figures 7.6a, b, and c, respectively. The 100 pole figure shows the greatest intensity in the center of the pole figure, indicating that a large number of the grains are [100]

oriented. There are, however, some areas of intensity at different ψ values, indicating that some of the grains have their [100] axis tilted relative to the sample normal. It is surprising also, that these additional areas of intensity appear as 6 lobes. It is not known at this time as to why such lobes should appear. The (110) and (210) pole figures for the blanket PZT sample show little intensity at the center, indicating that few grains have those orientations parallel to the normal of the sample.

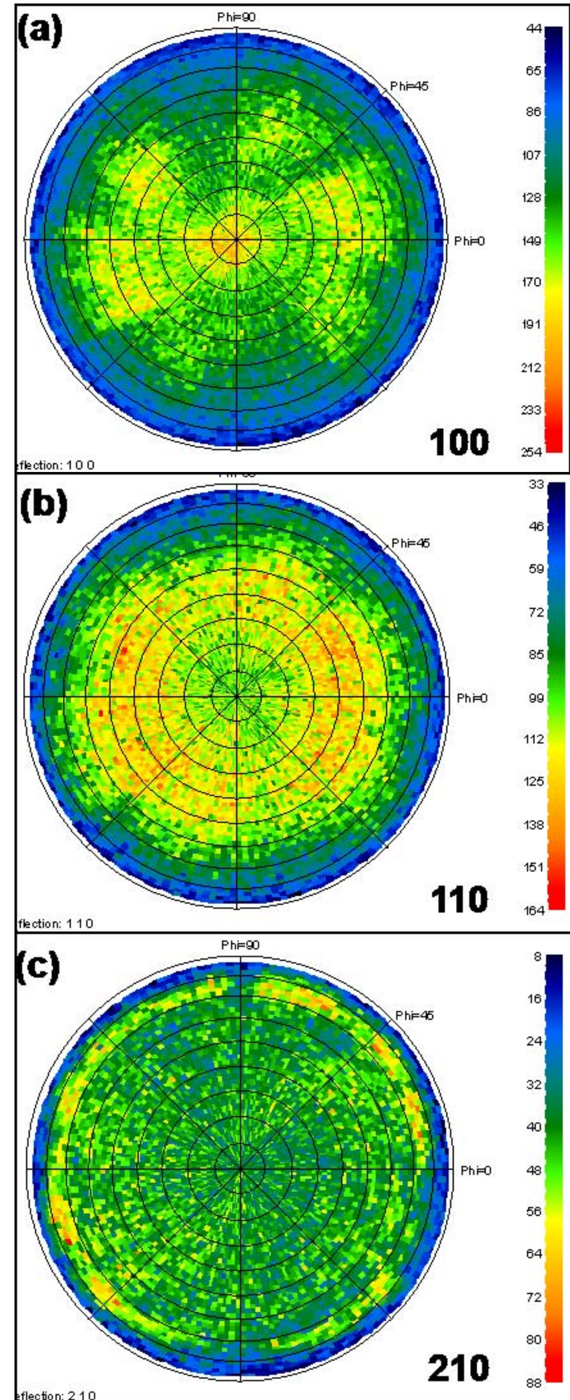


**Figure 7.6.** XRD texture pole figures for (a) 001, (b) 110, (c) 210 planes of the blanket PZT layer.

## 7.5. PFM AND BEPS RESULTS

To explore the domain structure and piezoresponse of the blanket PZT layer sample, vertical piezoresponse force microscopy (PFM) was performed. Figure 7.7 shows the principle behind vertical PFM [70]. The set up of PFM is similar to that of a contact mode AFM. A conductive tip on a cantilever is brought into contact with the sample surface. An AC voltage is applied to the tip, and the tip is

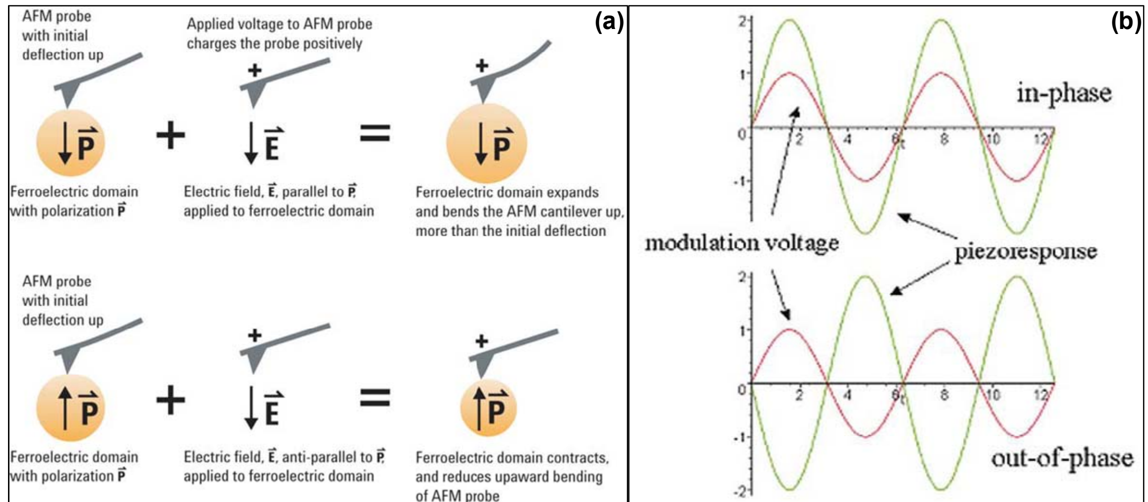


**Figure 7.7.** (a) Schematic of the principle of PFM. (b) Relationship between the applied AC voltage signal to the tip and the deflection of the tip (piezoresponse).

scanned over the surface of the sample. It is important to take into account the coercive bias for the material (see figure 5.2) when probing the piezoresponse of the material since applying a bias to the tip equal to or greater than the coercive bias will cause domains in the sample with polarizations antiparallel to the electric field produced by the tip to switch. When the tip has a positive bias in vertical PFM mode, and is in contact with a domain whose polarization is pointing downwards into the sample and thus is parallel to the electric field produced by the tip, then due to the inverse piezoelectric effect, the domain physically expands deflecting the cantilever upwards. When the bias of the tip moves to a negative voltage, the electric field from the tip and the polarization of the domain are antiparallel and the tip and cantilever are deflected downwards as the domain contracts. Thus, the deflection of the tip and cantilever are in phase with the AC voltage applied to the tip. If the domain has a polarization that is pointing downwards into the sample, then the AC voltage and the cantilever motion are out of phase by 180°. As with AFM, a laser beam is reflected off the back of the cantilever onto a detector that records the displacement of the cantilever. Vertical PFM works for domains that have a

polarization component in the direction normal to the sample surface (out of plane). For domains that have polarizations in plane with the sample surface, lateral PFM is used to determine their orientation. In lateral PFM, torsional motion of the cantilever, which is caused by piezoelectric shear deformation of the surface, is measured instead of vertical displacement [71].

Vertical PFM was performed at Oak Ridge National Laboratory using an Asylum PFM with an ElectriLevers tip. An AC voltage was applied to the tip with an amplitude of 2 V and a frequency of 289 kHz. Figure 7.8a shows a 1 μm by 1 μm AFM image of the blanket PZT surface. In the image, individual PZT grains can be seen similar to the grains seen with AFM at the University of Oklahoma.

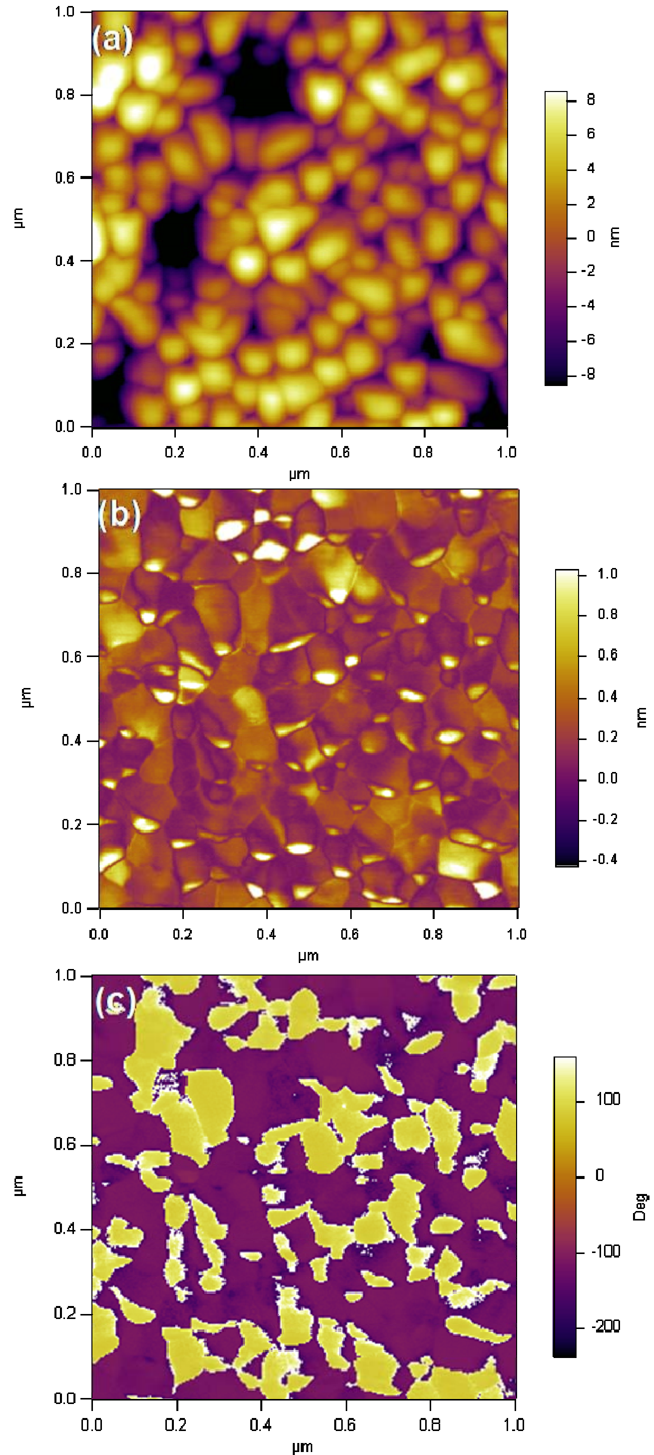


**Figure 7.8.** (a) AFM image of an area of the blanket PZT. (b) PFM amplitude image showing piezoresponse. (c) PFM phase image showing domains.

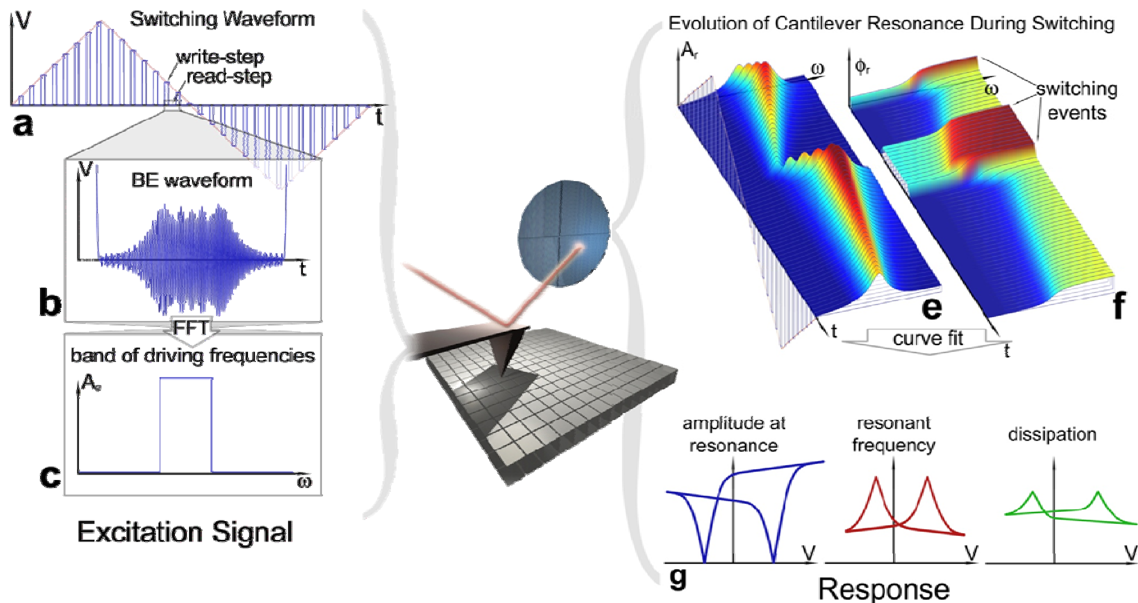


**Figure 7.9.** Schematic of the principle behind BEPS.

Figure 7.8b shows an amplitude PFM image of the same area. In this image, the amplitude of the deflection of the cantilever, due to the polarization of the PZT domains, is displayed. The image shows changes in piezoresponse across the scan area. Figure 7.8c shows the phase difference between the AC voltage applied to the tip and the oscillation of cantilever deflection due to the piezoresponse. Parallel and antiparallel out-of-plane domains can be seen as stark changes in the coloration on the image.

In addition to measuring the piezoresponse of the PZT, preliminary band excitation piezoresponse spectroscopy (BEPS) measurements were made to investigate the local switching behavior of the PZT. The schematic of the principle of BEPS is shown in figure 7.9 [72]. In BEPS, a series of pulses of steadily changing DC bias is applied to the PFM tip, as shown in figure 7.9a to induce polarization switching. In between these pulses, when the DC bias is off, the PFM tip and cantilever is excited by a voltage pulse of a band of frequencies centered around the resonance frequency of the cantilever indicated by figures 7.9b and 7.9c. By doing this, the piezoresponse of the PZT can be

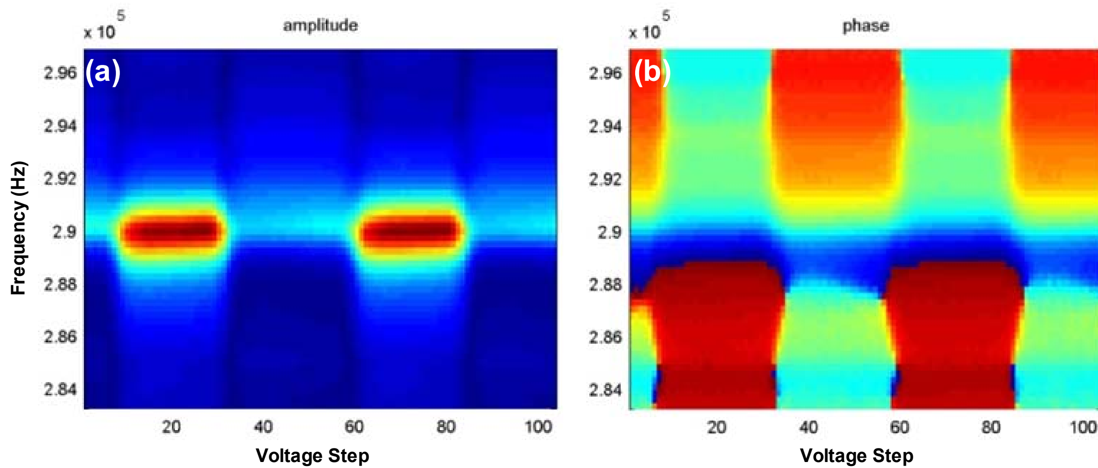


**Figure 7.10.** BEPS Spectrograms (frequency vs. voltage step) during polarization switching for (a) amplitude and (b) phase of the piezoresponse.

probed directly after a polarization pattern has been created by the DC bias pulse. The preliminary results of BEPS on the blanket PZT layer are shown in figure 7.10. Figure 7.10a shows a spectrogram of the amplitude of the piezoresponse and 7.10b shows a spectrogram of the phase. Polarization switching has occurred when the phase changes by 180° as shown. This project is on-going and will hopefully yield detailed information on the piezoresponse and switching behavior of the blanket PZT film in the future.

### 7.6. CONCLUSIONS

A blanket layer of PZT on a bottom FRAM capacitor electrode has been characterized. SEM and AFM results show individual PZT grains with dimensions similar to those found in fully fabricated FRAM device capacitors. In addition, depressions in the PZT film were noted and are thought to be associated with the tungsten contacts underneath the bottom electrode structure. XRD and texture results show that grains in the film are not randomly oriented, but have a preference for either the a- or c-axis oriented normal to the sample surface. Preliminary piezoresponse force microscopy results show ferroelectric domains in the PZT and a variation in piezoresponse from the

PZT. In addition, preliminary results of band excitation piezoresponse spectroscopy (BEPS) show clear, measureable switching behavior in the PZT film. Future work including TEM, NBD, EBSD, and electron holography characterization of the blanket PZT film in conjunction with on-going PFM and BEPS will provide a better picture of FRAM PZT films for improving FRAM device performance.

### 7.7. ACKNOWLEDGEMENTS

The author would like to thank Dr. Stephen Jesse and Dr. Arthur Baddorf at Oak Ridge National Laboratory for performing PFM and BEPS, Dr. Andrew Payzant at Oak Ridge National Laboratory for performing the texture measurements, Dr. Joel Keay discussions on XRD, Dr. Preston Larson for discussions on SEM, and Mr. Ernie Sanchez for performing AFM.

# BIBLIOGRAPHY


[1] http://www.er.doe.gov/bes/BES.html.

[2] http://www.nanoscience.gatech.edu/zlwang/research/tem.html.

[3] K. Urban, B. Kabius, M. Haider, H. Rose, *J. Elec. Microsc.* **48**, 821 (1999).

[4] C. Kisielowski, *et al.*, *Microsc. and Microanal.* **14**, 469 (2008).

[5] P. Bettotti, M. Cazzanelli, L. D. Negro, B. Danese, Z. Gaburro, C. J. Oton, G. V. Prakash, and L. Pavesi, *J. Phys.: Condens. Matter* **14**, 8253 (2002).

[6] Y. Kanemitsu, in *Towards the First Silicon Laser*, Ed. L. Pavesi, S. Gaponenko, and L. D. Negro (Kluwer Academic Publishers, Dordrecht, The Netherlands, 2003), Vol. 93, p. 115.

[7] L. T. Canham, *Appl. Phys. Lett.* **57**, 1046 (1990).

[8] S. Schuppler, S. L. Friedman, M. A. Marcus, D. L. Adler, Y. H. Xie, F. M. Ross, T. D. Harris, W. L. Brown, Y. J. Chabal, L. E. Brus, and P. H. Citrin, *Phys. Rev. Lett.* **72**, 2648 (1994).

[9] A. Wellner, R. E. Palmer, J. G. Zheng, C. J. Kiely, and K. W. Kolasinski, *J. Appl. Phys.* **91**, 3294 (2002).

[10] S. G. Cloutier, P. A. Kossyrev, and J. Xu, *Nat. Mater.* **4**, 887 (2005).

[11] T. A. Schmedake, F. Cunin, J. R. Link, and M. J. Sailor, *Adv. Mater.* **14**, 1270 (2002).

[12] J. Li, M. Greshow, D. Stein, E. Brandin, and J. A. Golovchenko, *Nat. Mater.* **2**, 611 (2003).

[13] H. Masuda, and M. Satoh, *Jpn. J. Appl. Phys.* **35**, L126 (1996).

[14] H. I. Liu, N. I. Maluf, R. F. W. Pease, D. K. Biegelsen, N. M. Johnson, and F. A. Ponce, *J. Vac. Sci. Technol. B* **10**, 2846 (1992).

[15] H. I. Liu, D. K. Biegelsen, N. M. Johnson, F. A. Ponce, R. F. W. Pease, *J. Vac. Sci. Technol. B* **11**, 2532 (1993).

[16] H. I. Liu, D. K. Biegelsen, F. A. Ponce, N. M. Johnson, and R. F. W. Pease, *Appl. Phys. Lett.* **64**, 1383 (1994).

[17] C. Single, F. Zhou, H. Heidemeyer, F. E. Prins, D. P. Kern, and E. Plies, *J. Vac. Sci. Technol. B* **16**, 3938 (1998).

[18] H Heidemeyer, C. Single, F. Zhou, F. E. Prins, D. P. Kern, and E. Plies, *J. Appl. Phys.* **87**, 4580 (2000).

[19] P. R. Larson, *Doctor of Philosophy Thesis*, Dept. of Physics and Astronomy, University of Oklahoma (2005).

[20] A. P. Alivisatos, *J. Phys. Chem.* **100**, 13226 (1996).

[21] L. E. Shea Rohwer, B. L. Abrams, J. P. Wilcoxon, and S. G. Thoma, Proc. of SPIE 5366, 66 (2004).

[22] W. U. Huynh, J. J. Dittmer, and A. P. Alivisatos, *Science* **295**, 2425 (2002).

[23] M. Bruchez, M. Moronne, P. Gin, S. Weiss, and A. P. Alivisatos, *Science* **281**, 2013 (1998).

[24] L. Manna, D. J. Milliron, A. Meisel, E. C. Scher, A. P. Alivisatos, *Nature Materials* **2**, 382 (2003).

[25] D. J. Milliron, S. M. Hughes, Y. Cui, L. Manna, J. Li, L. M. Wang, and A. P. Alivisatos, *Nature* **430**, 190 (2004).

[26] R. N. Bhargava, D. Gallagher, X. Hong, and A. Nurmikko, *Phys. Rev. Lett.* **72**, 416 (1994).

[27] N. Pradhan, D. Goorskey, J. Thessing, and X. Peng, *J. Am. Chem. Soc.* **127**, 17586 (2005).

[28] N. Pradhan, D. M. Battaglia, Y. Liu, and X. Peng, Nano. Lett. 7, 312 (2007).

[29] N. Pradhan, D. Goorskey, J. Thessing, and X. Peng, *J. Am. Chem. Soc*. **129**, *129*, 3339 (2007).

[30] R. Viswanatha, D. M. Battaglia, M. E. Curtis, T. D. Mishima, M. B. Johnson, and X. Peng, *Nano. Res.* **1**, 138 (2008).

[31] *Lead Chalcogenides: Physics and Applications*, edited by D. Khokhlov (Taylor and Francis, New York, 2003).

[32] Z. Shi, G. Xu, P. J. McCann, X. M. Fang, N. Dai, C. L. Felix, W. W. Bewley, I. Vurgaftman, and J. R. Meyer, *Appl. Phys. Lett.* **76**, 3688 (2000).

[33] E. Max, S. T. Eng, *Optical and Quantum Electronics* **9**, 411 (1977).

[34] F. K. Tittel, D. Richter, A. Fried in *Solid-State Mid-Infrared Laser Sources*, edited by I. T. Sorokina and K. L. Vodopyanov, (Springer-Verlag, New York, 2003).

[35] A. Rogalski*, Opto-electronics Review* **12**, 221 (2004).

[36] V. Mathet, P. Galtier, F. Nguyen-Van-Dau, G. Padeletti, J. Olivier, *J. Crystal Growth* **132**, 241 (1993).

[37] P. Mueller, H. Zogg, A. Fach, J. Johsn, C. Paglino, A. N. Tiwari, and M. Krejci, *Phys. Rev. Lett.* **78**, 3007 (1997).

[38] J. Ma, D. Li, G. Bi, F. Zhao, S. Elizondo, S. Mukherjee, and Z. Shi, *J. Electron. Mater.* **38**, 325 (2009).

[39] F. Zhao, S. Mukherjee, J. Ma, D. Li, S. L. Elizondo, and Z. Shi, Appl. Phys. Lett. 92, 211110 (2008).

[40] R. Flemming, *Canadian Journal of Earth Sciences* **44**, 1333 (2007).

[41] Scott, James F., *et al*, *Science* **246**, 1400 (1989).

[42] K.M. Rabe, *Nat. Mater.* **1**, 147 (2002).

[43] G. Shirane and K. Suzuki, *J. Phys. Soc. Jpn.* **7**, 333 (1952).

[44] D.B. William and C.B. Carter, in *Transmission Electron Microscopy*, (Plenum Press, New York, 1996), Chap. 9, p. 141.

[45] M. Malac, F. Wang, R. Egerton, Y. Taniguchi, Microsc Microanal 13(Suppl 2), 558CD (2007).

[46] http://www.doitpoms.ac.uk/tlplib/piezoelectrics/spontaneous_polar.php.

[47] N. Izyumskaya, *et al.*, *Critical Reviews in Solid State and Materials Sciences* **32**, 111 (2007).

[48] S. R. Summerfelt, *et al.*, *Appl. Phys. Lett.* **79**, 4004 (2001).

[49] R. Bailey, *et al.*, *Proc. ICCD*, 485 (2005).

[50] K.R. Udayakumar, et al, *JJAP* **45**, 3202 (2006).

[51] T.S. Moise, *et al*., *IEDM Tech. Dig*., 940 (1999).

[52] R. Anderson and S. J. Klepeis, in Introduction to Focused Ion Beams: Introduction, Theory, Techniques and Practice, edited by L.A. Giannuzzi and F.A. Stevie (Springer, New York, 2005), Chap. 9, p. 180.

[53] http://www.asu.edu/clas/csss/NUE/FIBLift-Out.html.

[54] A. Armigliato, S. Frabboni, and G.C. Gazzadi, *Appl. Phys. Lett.* **93**, 161906 (2008).

[55] S. Aggarwal, K. R. Udayakumar, and J. A. Rodriguez, *J. Appl. Phys.* **100**, 064103 (2006).

[56] H. Lichte, *et al.*, *Annu. Rev. Mater. Res.* **37**, (539) 2007.

[57] K. Honda, *FUJITSU Sci. Tech. J.* **38**, 64 (2002).

[58] D. Gabor, *Nature* **161**, 777 (1948).

[59] Z. L. Wang*, Adv. Mater.* **15**, 1497 (2003).

[60] D. B. William and C.B. Carter, in *Transmission Electron Microscopy*, (Plenum Press, New York, 1996), Chap. 5, p. 76.

[61] Tonomura, A., in *Electron Holography*, (Springer, Berlin, 1999).

[62] J. E. Bonevich, *et al.*, in Introduction to Electron Holography, edited by E. Völkl, L. F. Allard, D. C. Joy, (Kluwer Academic / Plenum Publishers, New York, 1999).

[63] M. R. McCartney and D. J. Smith, *Annu. Rev. Mater. Res.* **37**, 729 (2007).

[64] K. Harada and A. Tonomura, *Appl. Phys. Lett.* **84**, 3229 (2004).

[65] K. Harada, Y. Togawa, T. Akashi, T. Matsuda, A. Tonomura, *Microsc. Microanal.* **10**, 986 (2004).

[66] K. Harada, A. Tonomura, T. Matsuda, T. Akashi, Y. Togawa, *J. Appl. Phys.* **96**, 6097 (2004).

[67] K. Harada, T. Akashi, Y. Togawa, T. Matsuda, A. Tonomura, *J. Elec. Microsc.* **54**, 19 (2005).

[68] J. Endo, J. Chen, D. Kobayashi, Y. Wada, H. Fujita, *Appl. Opt.* **41**, 1308 (2002).

[69] B. D. Cullity and S.R. Stock, in Elements of X-Ray Diffraction, $3^{rd}$ edition, (Prentice Hall, New Jersey, 2001) p. 167-177.

[70] S. Wu, Piezoresponse Force Microscopy Application Note, Agilent Technologies.

[71] A. Gruverman and S. V. Kalinin, *J. Mat. Sci.* **41**, 107 (2006).

[72] S. Jesse, P. Maksymovych, and S. V. Kalinin, *Appl. Phys. Lett.* **93**, 112903 (2008).